UNIVERSITY OF OKLAHOMA

GRADUATE COLLEGE

CHARACTERIZATION OF ARBUCKLE-BASEMENT SYSTEM WITH A FOCUS ON SEISMIC ATTRIBUTES IMAGE OF IGNEOUS INTRUSIONS AND SEISMIC RESOLUTION, PAYNE COUNTY, NORTHERN OKLAHOMA

A DISSERTATION

SUBMITTED TO THE GRADUATE FACULTY

in partial fulfilment of the requirements for the

Degree of

DOCTOR OF PHILOSOPHY

By

GABRIEL MACHADO
Norman, Oklahoma
2019

CHARACTERIZATION OF ARBUCKLE-BASEMENT SYSTEM WITH A FOCUS ON SEISMIC ATTRIBUTES IMAGE OF IGNEOUS INTRUSIONS AND SEISMIC RESOLUTION, PAYNE COUNTY, NORTHERN OKLAHOMA

A DISSERTATION APPROVED FOR THE
SCHOOL OF GEOSCIENCES

BY THE COMMITTEE CONSISTING OF

Dr. Kurt J. Marfurt, Chair

Dr. Matthew Pranter

Dr. Brett Carpenter

Dr. Bradley Wallet

Dr. Zulfiquar Reza

© Copyright by GABRIEL MACHADO 2019
All Rights Reserved.

To my God, my Most Holy Mother Mary and Divine Mercy.

Acknowledgements

First, to my advisor, Dr. Kurt Marfurt, for 5 years of teaching. Not just a great professional, but, most importantly, a good person, in all it entails.

To my committee members, for constant support and advice throughout this long and arduous process.

To all my co-authors: Garret Hickman, Maulin Gogri, Dr. Matthew Pranter, Dr. Zulfiquar Reza, Folarin Kolawole, Rachel Neher, Thang Ha and Bin Lyu. These papers would not have been half as good if not for your input and help.

To the unsung heroes of the department, our beloved staff: Rebecca Fay, Leah Moser, Ginger Leivas Ginny Guedez and Ashley Tullius. Thank you for your continuous support throughout the years.

To my friends, constantly pushing me to try harder and to not give up.

Lastly, to my parents, my brother and my sister, I owe my life and who I am and where how far I have made it, to you.

Table of Contents

Acknowledgements v

Table of Contents vi

List of Figures xi

Abstract xxvii

Chapter 1: Introduction 1

References 5

Figures 9

Chapter 2: Characterization of Arbuckle-Basement waste-water disposal system, Payne county, northern Oklahoma 10

Abstract 10

Introduction 11

Geologic setting 14

Methods 15

3D Seismic Processing, Interpretation, and Attribute Analysis 15

Well-Log Cross-Sections and Formation Correlation 17

Structure-Contour and Isopach Mapping 18

Construction of a 3D Reservoir Model 18

Porosity Modeling 19

Permeability Modeling 20

Analysis of the Injection Data 21

History-Matching Methodology 22

Results. 24

Core and Log Properties of the Arbuckle Group 24

Top Basement Structure-Contour Map including Key Faults based on Seismic Data 24

Arbuckle Group Structure-Contour and Isopach Trends based on Seismic and Well Data 25

3D Reservoir Model Grid (3D Stratigraphic and Structural Framework).........25

Porosity Distribution of the Arbuckle Group and Basement 25

Permeability Distribution of Arbuckle Group and Basement............................26

Quality Control and Preconditioning of the Injection Data 26

History-Matching Results 28

Limitations...30

Conclusions..31

Acknowledgments...32

References..32

Figures 38

Tables...65

Chapter 3: Mafic sill complexes and interactions in the Precambrian basement of north-central Oklahoma: insights from depth-migrated seismic imaging 66

Abstract...66

Introduction..67

Geologic setting and data available...68

Methodology 71

Prestack time vs prestack depth migration...71

Processing Workflow 72
How thin is thin in the basement? 73
Outcrop-based models 74
Seismic attributes 76
Results. 77
Time versus depth migration 77
Outcrop-based models seismic attribute response 78
Comparison with real depth-migrated seismic data 81
Limitations 82
Discussion and conclusions 84
Acknowledgments 85
References 85
Figures 91
Chapter 4: Limitations to thin bed resolution 106
Abstract 106
Introduction 106
Defining resolution 106
Improving resolution 109
Methodology 111
Wedge models 111
Spectral balancing 112
Continuous Wavelet Transform (CWT) Bandwidth Extension 114
Hölder exponent 115

Results and discussions 116
  Continuous Wavelet Transform (CWT) bandwidth extension 117
  Spectral balancing 120
  Hölder exponent 121
  Seismic well-ties 123
Discussion 124
Conclusions 125
Acknowledgments 126
Appendix A 126
  Reflectivity decomposition 126
Appendix B 127
  The Continuous Wavelet Transform (CWT) 127
Appendix C 131
  Maximum Moduli Lines (MML) 131
Appendix D 132
  Hölder exponent 132
References 134
Figures 137
Chapter 5: Conclusions 158

List of Tables

Table 1. Minimum, maximum and average porosity values for Arbuckle and Simpson formations based on history-match. 65

Table 2. Minimum, maximum and average permeability values for Arbuckle and Simpson formations based on history match. 65

List of Figures

Figure 1. Map view of seismic survey for current study in Payne County, Oklahoma, with hypocenter of earthquakes from 2010 through 2106 color coded by year. Some clusters of events can be observed in the southern portion of survey and outside of it...9

Figure 2. Cumulative number of magnitude 2.5+ earthquakes in Oklahoma (After Walsh and Zoback 2015)...38

Figure 3. (a) Map showing the location of Payne County, Oklahoma., (b) Boundaries (in crimson) of the 3D seismic survey and (in blue) of the 3D cellular model. Black dots indicate the wells that penetrated the Arbuckle in the study area. (c) A chair display through the seismic amplitude volume. The top of the survey has been cropped 20 ms above the top Arbuckle Formation. The time slice is approximately 800 ms below the top of basement. 39

Figure 4. Core from the Catoosa, OK, Amoco Shads #4 Well, with its formations and their respective depths, located in Rogers County (Gogri, 2018)...40

Figure 5. Vertical slice through the 3D seismic amplitude volume (a) before and (b) after structural-oriented-filtering and spectral balancing with a -114° phase shift as guided by the data owner. Red sub vertical lines are example faults interpreted in the basement. 41

Figure 6. Horizon slice of the Arbuckle Group top through (a) seismic amplitude, (b) coherence, (c) negative curvature and (d) positive curvature. 42

Figure 7. Time slice at the approximate location of the Arbuckle Group top through total aberrancy co-rendered with the azimuth of the aberrancy. An opacity curve is applied such that high aberrancy features appear transparent. Events are colored according to the azimuth in which they are flexing downwards...43

Figure 8. Type log of a gamma ray (to the left) and resistivity and porosity (to the right) showing the major formation tops picked from the Ordovician Arbuckle Group up through the Pennsylvanian Oolagah Limestone showing their ages, as seen on well E. I can see significant contrasts of resistivity and porosity values below the Simpson and Arbuckle Group tops. 44

Figure 9. Arbuckle Group structure contour map. The depths increase about 1,000 ft (~300 m) from northeast to southwest...45

Figure 10. Simulation model schematic showing the four major formations. The 3D grid consists of cells with aerial dimensions of 500 ft by 500 ft (152 m by 152 m) and an average layer thickness of 3 ft (0.9 m) resulting in a total of approximately 6.5 million cells..........................46

Figure 11. Type log of the Arbuckle group with the following tracks: a) gamma ray curve, b) resistivity, c) porosity, and d) bulk density. This well was located outside of the seismic survey, but within the limits of the reservoir model, as can be seen in **Figure 15**. 47

Figure 12. Horizon slice along the top Arbuckle Group through the negative curvature volume showing lineaments corresponding to faults seen on vertical slices through the seismic amplitude volume. Blue arrows indicate three of the larger faults that continue up through the Red Fork formation (personal communication from the data owner). 48

Figure 13. Structure map of basement top. White lines represent location of faults interpreted from curvature attributes. 49

Figure 14. Structure map of Arbuckle Group top. White lines represent location of faults interpreted from curvature attributes...50

Figure 15. Arbuckle Group Isopach map. The average thickness is approximately 1200 ft. (~380 m) for most of the survey with the unit thickening to the southwest and northwest. White circle represents location of type log shown in **Figure 11**. 51

Figure 16. Stratigraphic framework (3D grid). A proportional layering scheme was used, and the resulting grid contains approximately 6.5 million cells. The 3D grid consists of cells with aerial dimensions of 500 ft. by 500 ft. (152 m by 152 m) and an average layer thickness of 3 ft. (0.9 m). 52

Figure 17. Porosity model of the basement through Viola intervals. Vertical exaggeration 10x. 53

Figure 18. Permeability model of the basement through Viola intervals. Permeability values range from 0.1 – 100 mD, with the highest permeability values being associated with faults interpreted from the seismic survey. Vertical exaggeration 10x. 54

Figure 19. Pressure and injection-rate data for a well highlighting various forms of data quality issues. WHP stands for Well Head Pressure. 55

Figure 20. Conversion of wellhead pressure to bottomhole pressure for a well. BHP stands for Bottom Hole pressure.. 56

Figure 21. Material-balance-time diagnostics plot of a random well for flow regime identification.. 57

Figure 22. Silin-slope plot. 58

Figure 23. Modified Hall plot analysis of a well. 59

Figure 24. Bottom hole pressure history-match quality. Color coded based on mismatch: Grey – Inconsistent or no data, Green – less than 10%, Yellow – within 10 and 50% and Red – greater than 50%. In the background, I display the elevation of the Arbuckle Group top: blue represents deeper regions while red the shallower regions.. 60

Figure 25. Bottom hole pressure and injection rate match for two wells. (a) Bottom hole pressure for Well 1; (b) Water injection rate for Well 1; (c) Bottom hole pressure for Well 2; and (b) Water injection rate for Well 2. 61

Figure 26. Distribution of pressure in the basement formation at a) the beginning of 2005 and b) the beginning of 2016...62

Figure 27. Distribution of pressure buildup due to wastewater injection in the basement formation at the beginning of 2016...63

Figure 28. Significance of the interpreted faults based on pressure buildup around the disposal wells. Wells are color coded according to the quality of pressure match as used in **Figure 24**. In the background, I display the elevation of the Arbuckle Group formation top: blue represents deeper regions while red the shallower regions...64

Figure 29. (a) Map of geologic provinces of Oklahoma, with red star indicating location of seismic survey in Payne county (modified from Johnson, 2008) and blue star indicating location of outcrops in (c) and (d). The green star indicates the outcrop of the Spavinaw Granite host rock. (b) Map of geologic interpretation of basement rocks based on geophysical and drill hole data (modified after Shah and Keller, 2017). (c) and (d) are photographs of characteristic geometries observed in diabase sills in granite host rock, south Oklahoma. (c) shows intrusion interaction with pre-existent fracture in place, while (d) represent the interaction of mafic sill in the absence of a pre-existing fracture..91

Figure 30. Chair display of time-migrated, depth-converted seismic amplitude volume used in this study showing the Top Arbuckle Group and Top Basement surfaces, along with four interpreted basement faults as colored polygons. Red arrows indicate mapped amplitude anomalies interpreted in the basement as mafic intrusions (after Kolawole et al., 2019).............92

Figure 31. Workflow for depth migrating the seismic volume. Three iterations of velocity spectral semblance analysis and residual statics were computed before improving the velocity further using a tomographic solution. Two iterations of PSDM were computed before converging to a depth migration volume. 93

Figure 32. Wedge model generated to test the limits of seismic resolution of diabase intrusions on granite host rock. (a) Conceptual model geometry of mafic diabase intrusion in felsic granite basement rock. The model contains a wedge with a 0-1200 ft varying thickness thinning towards the left. Reflectivity coefficients calculated from (a) are convolved with a 20 Hz and 50 Hz Ricker wavelet to generate synthetic seismograms in (b) and (c). Amplitude vs thickness plots are constructed for (b) and (c) in (d) and (e). Blue arrows indicate the onset of tuning for both cases. Peak in amplitude occurs at 160 ft for (d) and 400 ft for (e). Thickness less than these cannot be estimated through conventional two-way traveltime analysis (Widess, 1973). Note that beds of different thicknesses may exhibit the same amplitude response, hence amplitude is not a reliable indicator of thickness for this model below a specific threshold. 94

Figure 33. Conceptual and geometric models of diabase sills hosted in granite host rock in the presence or absence of pre-existing faults (modified from Stephens et al., 2017). (a) and (b) Conceptual models of mafic emplacement in an early stage of shallow intrusion with magma segments adjacent to a steep discontinuity. (c) my corresponding synthetic model. (d) and (e) Conceptual model of mafic emplacement in later stages of shallow intrusion with magma segments inflation of the initial sill segments leading to linkage through stepping or breached relay structures. (f) my corresponding synthetic model. (g) and (h) Conceptual models of mafic emplacement in the absence of pre-existing discontinuities that lead to the development of sub-parallel sill segments. (i) my corresponding synthetic model. 95

Figure 34. (a) Representative vertical cross section of time-migrated, depth-converted seismic amplitude volume. The blank area in the middle of the line is due to lack of a seismic acquisition permit. (b) highlights my fault interpretation. Red rectangles are zoomed-in mafic intrusions in (c) and (d). Depth conversion was performed with the same velocity model as in depth conversion in **Figure 35**. The intrusion from (d) was mapped in (e) Red ellipses highlights interpreted fault defining geometry of reflector after time migration.......................................96

Figure 35. (a) Representative vertical cross section of depth-migrated seismic amplitude volume. The blank area in the middle of the line is due to lack of a seismic acquisition permit. (b) highlights my fault interpretation. Red rectangles are zoomed-in mafic intrusions in (c) and (d). Depth migration was performed with the same velocity model as in depth conversion. Depth migration and depth conversion were performed with the same velocity model. Notice that after depth migration, the overall appearance of such intrusion is flatter. The intrusion from (d) was mapped in (e) Red ellipses highlights interpreted fault defining geometry of reflector not seen in time-migrated, depth converted data..97

Figure 36. Synthetic models of diabase intrusions in granite host rock based on outcrop observation through seismic amplitude. The modeled intrusion thickness is approximately 150 ft. First column represents synthetic seismograms for “faulted” model, second column for “inflated” model and third column for “overlap” model. The reflectivity series generated from each geometric model was convolved with a 20 Hz Ricker wavelet (a), (b), (c), (g) and (h) or a 50 Hz Ricker wavelet (d), €, (f), (i), and (j). (a), (b), (d) and (e) are modeled with a fault throw of half he intrusion thickness, or approximately 75 ft; (g), (h), (i) and (j) are modeled with a fault throw of twice the intrusion thickness, or approximately 300 ft. The horizontal displacement for the column corresponding to “inflated” model is half the thickness of the layer, or approximately 75 ft. Separation between sills in “overlap” model is equal to the thickness of the intrusion, or approximately 150 ft. There is a clear contrast between the models generated with a 20 Hz

Ricker wavelet and the ones generated with a 50 Hz wavelet in how condensed and clear the reflections appear. Note the wavelet interference patter in (f) due to the closeness of the layers with regards to the size of wavelet. Such interference lowers the overall amplitude of the reflections in the overlapped region. 98

Figure 37. Synthetic models of diabase intrusions in granite host rock based on outcrop observation through coherence. The modeled intrusion thickness is approximately 150 ft. First column represents synthetic seismograms for "faulted" model, second column for "inflated" model and third column for "overlap" model. The reflectivity series generated from each geometric model was convolved with a 20 Hz Ricker wavelet (a, b, c, g and h) or a 50 Hz Ricker wavelet (d, e, f, i and j). (a), (b), (d) and (e) are modeled with a fault throw of half he intrusion thickness, or approximately 75 ft; (g), (h), (i) and (j) are modeled with a fault throw of twice the intrusion thickness, or approximately 300 ft. The horizontal displacement for the column corresponding to "inflated" model is half the thickness of the layer, or approximately 75 ft. Separation between sills in "overlap" model is equal to the thickness of the intrusion, or approximately 150 ft. Low frequency synthetics show more coherence than their high frequency counterparts. Higher fault throws show lower coherence than small fault throws. Wavelet interference patterns from "overlap" model are not detected by coherence, as seen on (c) and (f), but the edges of the overlap are clearly determined. Even though coherence anomalies from "inflated" model are generally weaker than those exhibited by" faulted" model, a large enough throw will be detected, as shown in (j). In contrast, for "faulted" model, most cases show a distinct coherence anomaly, but a large fault throw does not appear different than a relatively smaller one (compare g with i). 99

Figure 38. Synthetic models of diabase intrusions in granite host rock based on outcrop observation through curvature. The modeled intrusion thickness is approximately 150 ft. First column represents synthetic seismograms for “faulted” model, second column for “inflated” model and third column for “overlap” model. The reflectivity series generated from each geometric model was convolved with a 20 Hz Ricker wavelet (a, b, c, g and h) or a 50 Hz Ricker wavelet (d, e, f, i and j). (a), (b), (d) and (e) are modeled with a fault throw of half he intrusion thickness, or approximately 75 ft; (g), (h), (i) and (j) are modeled with a fault throw of twice the intrusion thickness, or approximately 300 ft. The horizontal displacement for the column corresponding to “inflated” model is half the thickness of the layer, or approximately 75 ft. Separation between sills in “overlap” model is equal to the thickness of the intrusion, or approximately 150 ft. Because of the configuration of the “faulted” model, no curvature anomaly is detected, as expected, as both sides of the fault are perfectly flat and thus, their curvature is zero. Similarly, for “overlap” model, curvature only partially detects the edges of the model for the low frequency case, due to interference patterns being interpreted as “signal” by the algorithm, but not for the high frequency case. For “inflated” model, the curvature anomaly is present in all cases, seeming to decrease in magnitude with higher frequencies. 101

Figure 39. Synthetic models of diabase intrusions in granite host rock based on outcrop observation through curvature. The modeled intrusion thickness is approximately 150 ft. First column represents synthetic seismograms for “faulted” model, second column for “inflated” model and third column for “overlap” model. The reflectivity series generated from each geometric model was convolved with a 20 Hz Ricker wavelet (a, b, c, g and h) or a 50 Hz Ricker wavelet (d, e, f, i and j). (a), (b), (d) and (e) are modeled with a fault throw of half he intrusion thickness, or approximately 75 ft; (g), (h), (i) and (j) are modeled with a fault throw of twice the intrusion thickness, or approximately 300 ft. The horizontal displacement for the column corresponding to “inflated” model is half the thickness of the layer, or approximately 75 ft. Separation between sills in “overlap” model is equal to the thickness of the intrusion, or approximately 150 ft. There are no distinct differences for both the “faulted” and the “inflated” models, both in terms of their response to this attribute when compared with seismic amplitude. The “overlap” model further proves that interference patterns in overlapping region decrease the amplitude of the reflectors in the area for low frequencies, but for high frequencies the amplitude is increased. 102

Figure 40. Synthetic models of diabase intrusions in granite host rock based on outcrop observation through curvature. The modeled intrusion thickness is approximately 150 ft. First column represents synthetic seismograms for “faulted” model, second column for “inflated” model and third column for “overlap” model. The reflectivity series generated from each geometric model was convolved with a 20 Hz Ricker wavelet (a, b, c, g and h) or a 50 Hz Ricker wavelet (d, e, f, i and j). (a), (b), (d) and (e) are modeled with a fault throw of half he intrusion thickness, or approximately 75 ft; (g), (h), (i) and (j) are modeled with a fault throw of twice the intrusion thickness, or approximately 300 ft. The horizontal displacement for the column corresponding to “inflated” model is half the thickness of the layer, or approximately 75 ft. Separation between sills in “overlap” model is equal to the thickness of the intrusion, or approximately 150 ft. In a similar way to **Figure 39**, there are no distinct responses of this attributes for “faulted” or “inflated” models when compared with seismic amplitude. The attribute only recognizes one event in all of these cases because the model’s thicknesses are below tuning, as shown wit **Figure 32**. In contrast with **Figure 39**, (c) shows an increase in the spectral peak magnitude from the wavelet interference within overlapping zone for the low source wavelet frequency case. In the same way as **Figure 39**f, for the high source wavelet frequency case in (f), there is a distinct increase in the peak magnitude observed in the overlapping zone. 103

Figure 41. Representative vertical cross section through (a) seismic amplitude, (b) coherence, (c) k_1 most positive curvature, (d) spectral peak magnitude, (e) spectral frequency and (f) amplitude envelope. Red square represents zoomed in area displayed in **Figure 42**. Seismic amplitude anomalies in basement (a) associated with mafic diabase intrusions into felsic granite host rock in basement. These intrusions are characterized by coherent reflectors (b), mixed curvature response (c), high spectral magnitude responses (d) mid-range frequencies (e) and relatively high envelope (f). 104

Figure 42. Representative vertical cross section of zoomed in square in **Figure 41** through (a) seismic amplitude, (b) coherence, (c) k_1 most positive curvature, (d) spectral peak magnitude, (e) spectral frequency and (f) amplitude envelope. Two seismic amplitude anomalies examined. Top intrusion exhibits a low coherence lineament cutting vertically through it, unlike low intrusion. Low intrusion displays a higher positive curvature magnitude than top one. Top intrusion displays higher spectral magnitudes than low intrusion, with an inverted trend for the amplitude envelope. Additionally, both intrusions show an interruption of spectral magnitude and amplitude envelope at the location of vertical low coherence lineament. Both intrusions show a peak frequency of approximately 30 Hz. 105

Figure 43. (a) Simple wedge models convolved with a (b) 30 Hz peak frequency Ricker wavelet and (c) its corresponding frequency spectrum. (Top of (a)) the Type III (Mix component); (middle of (a)) the Type II (even component); and (bottom of (a)) the Type I (odd component) wedges, according to Chung and Lawton (1995) and Chopra et al. (2006). (d) displays the amplitude spectrum of the wedges models averaged over the entire line. Peaks correspond to interference patterns generated from model interfaces. 137

Figure 44. (a) Wiggle display of simple wedge models convolved with a (b) 30 Hz peak frequency Ricker wavelet and (c) its corresponding frequency spectrum. 20% random noise of the RMS amplitude of the entire line was added to the model. (Top of (a)) the Type III (Mix component); (middle of (a)) the Type II (even component); and (bottom of (a)) the Type I (odd component) wedges, according to Chung and Lawton (1995) and Chopra et al. (2006). (d) displays the amplitude spectrum of the wedges models averaged over the entire line. Peaks correspond to interference patterns generated from model interfaces. 138

Figure 45. (a) Vertical cross section through seismic amplitude of the Diamond M field with (b) extracted wavelet in the 500-900 ms interval, approximately corresponding to the Clearfork and Wolfcampian formations, and (c) its corresponding frequency spectrum. (d) displays the amplitude spectrum of the entire volume for the aforementioned interval. Blue arrow indicates location of shallow acquisition footprint. Orange arrow indicates location of terminations from clinoforms of Clearfork formation. Red arrow indicates relatively flat and low amplitude reflectors from Wolfcampian formation...139

Figure 46. Spectral magnitude components A(t, f) for wedge models in **Figure 43** for (a) the 20 Hz component, (b) the 40 Hz component, and (c) the 80 Hz component. Red ellipses indicate tuning amplitudes where resolution of events becomes challenging. Note that, as predicted by Marfurt and Kirlin (2001), the tuning appears at a lower thickness for the even component than for the odd and mixed component. 140

Figure 47. Spectral ridge components for wedge models in **Figure 43** for (a) the 20 Hz component, (b) the 40 Hz component, and (c) the 80 Hz component. Red ellipses indicate tuning zones where resolution of events becomes challenging. Red arrows indicate a mislocation of events due to interference patters. Maximum constructive interference simulates the presence of only one wavelet, which is all that ridges can detect. Orange arrow indicate a location where maximum destructive interference occurs. The main lobe is destroyed but the sidelobe remains, so the algorithm detects it as main peak instead. Blue lines represent actual shape of the wedge. 141

Figure 48. Spectral voice components for wedge models in **Figure 43** for (a) the 20 Hz component, (b) the 40 Hz component, and (c) the 80 Hz component. Red ellipses indicate some of the tuning zones where resolution of events becomes challenging. The high amplitude sidelobes in the 20 Hz component give rise to the extra MML in **Figure 47**a. 142

Figure 49. Spectral phase components for wedge models in **Figure 43** for (a) the 20 Hz component, (b) the 40 Hz component, and (c) the 80 Hz component; co-rendered with spectral magnitude component in a monochrome gray color bar. An opacity curve applied for low values of spectral magnitude, rendering high values transparent. Black ellipses indicate some of the tuning zones where resolution of events becomes challenging. 143

Figure 50.(a) Simple wedge models after bandwidth extension with the (b) extracted wavelet for the entire line and its (c) corresponding magnitude spectrum. (d) shows the amplitude spectrum of all three wedge models. The frequency range selected for the bandwidth extension was 5-100 Hz. As highlighted in **Figure 47**, red arrow indicates location where ridges merged due to tuning interference to create a false event. Purple arrows indicate location of side lobes erroneously interpreted by algorithm as location of ridges. Orange arrow indicates location where algorithm was not capable of resolving bottom layer, resulting in shadow zone within reconstructed line.

For high frequency components, the algorithm depicts a sharper and clearer image of the reflectors..144

Figure 51. (a) Vertical cross section through bandwidth extended seismic amplitude of the Diamond M field with (b) extracted wavelet in the 500-900 ms interval, approximately corresponding to the Clearfork and Wolfcampian formations, and (c) its corresponding frequency spectrum. (d) displays the amplitude spectrum of the entire volume for the aforementioned interval. The frequency range selected for the bandwidth extension was 5-100 Hz. Note flatter frequency spectrum. However, in the presence of clinoforms in the Clearfork formation, the algorithm fails to highlight them...145

Figure 52. (a) Simple wedge models after spectral balancing with the (b) extracted wavelet for the entire line and its (c) corresponding magnitude spectrum. (d) shows the amplitude spectrum of all three wedge models. Higher and lower frequencies amplitude are balanced when compared with **Figure 43**. I used an epsilon value of ε = 1%...146

Figure 53. (a) Simple wedge models with added 20% random noise after spectral balancing with the (b) extracted wavelet for the entire line and its (c) corresponding magnitude spectrum. (d) shows the amplitude spectrum of all three wedge models. Higher and lower frequencies amplitude are balanced when compared with **Figure 44**. I used an epsilon value of ε = 1%....147

Figure 54. (a) Vertical cross section through spectrally balanced seismic amplitude of the Diamond M field with (b) extracted wavelet in the 500-900 ms interval, approximately corresponding to the Clearfork and Wolfcampian formations, and (c) its corresponding frequency spectrum. (d) displays the amplitude spectrum of the entire volume for the aforementioned interval. Blue arrow indicates attenuated acquisition footprint and orange arrows indicate areas with improved vertical resolution. I used equation 4 with a value of ε = 0.01.........................148

Figure 55. Hölder exponent response to a simple acoustic impedance sequence. (a) shows the modeled acoustic impedance profile generated. A change occurs every 100 ms. Two thin beds of opposite acoustic impedance contrasts are modeled at the bottom, along with a sharp acoustic impedance change in the top and a grading increase and decrease of velocity is modeled between 300 and 500 ms. We convolve this acoustic impedance model with an Ormsby wavelet (*f1=5 Hz, f2=10 Hz, f3= 60 Hz* and *f4=70 Hz*) on (b) to generate a seismic reflectivity trace. We compute the Hölder exponent on this trace and display the result in (c). As expected, the sharp response of the thin beds is matched by high, positive values of the Hölder exponent. The four inflection points in the increasing and decreasing velocity gradients are characterized by four peaks of negative values in the Hölder exponent trace. 149

Figure 56. Computed Hölder exponent on wedge models from **Figure 43**. Highest values show location of tuning thicknesses, as in **Figure 46**. Interior of wedges characterized by mid-range values. Blue arrow indicates location of low Hölder exponent anomaly associated with wavelet sidelobes interference patterns. In contrast, red arrow shows location of high Hölder exponent anomaly associated with rapid increase of magnitude of high frequencies due to tuning effects near thin bed conditions. 150

Figure 57. Extracted Hölder exponent trace at well location in Diamond M field. Yellow arrows indicate locations of "M" shaped functions that correspond to changes in the acoustic impedance. Local high values of the attribute, as indicated by orange arrow, may indicate potential zones of interest, as they reveal an increasing magnitude with frequency components that may be associated to potential targets. 151

Figure 58. Cross section of seismic volume from the Diamond M field through (a) seismic amplitude, (b) Hölder exponent attribute and (c) correndering of (a) and (b). I selected a discrete color bar better distinguish between different types of singularities that the attribute may be sensitive to. Blue arrow indicates Hölder exponent negative value for acquisition footprint. Orange arrow indicates at high Hölder exponent patch previously unnoticed from amplitude attribute. Purple arrow indicates zone of low, negative Hölder exponent values, interpreted as a result of the low energy Wolfcampian formation at this depth. 152

Figure 59. Seismic-to-well tie of Diamond M field seismic volume (a) before, (b) after spectral balancing with epsilon value ε = 1%, and (c) after CWT bandwidth extension with a 5-100 Hz frequency range. Correlation coefficient slightly improved from the subtly higher frequency magnitude balancing performed through this algorithm, but decreased after bandwidth extension. Interference patterns create false events and mislocate others, resulting in a decreased correlation coefficient. A 5-100 Hz frequency range was used to compute the spectral balancing and CWT bandwidth 153

Figure 60. Reflectivity types as defined by Chung and Lawton (1995). This concept was further developed for reflectivity decomposition in odd and even components, as defined by Tirado (2004); Portniaguine and Castagna (2004 and 2005); Chopra et al. (2006); Puryear and Castagna (2008); and Chopra et al. (2009)...155

Figure 61. Representative (a) Real and (b) imaginary component of a complex wavelet family and (c) their corresponding amplitude spectrum used in spectral decomposition of wedge models displayed on **Figure 46Figure 47**,**Figure 48** and**Figure 49**. This is also the same wavelet family used to reconstruct spectral balanced outputs in **Figure 52**, **Figure 53** and **Figure 54**. Note how the wavelets become sharper in time and broader band as the center frequency increases. A total of 95 components were computed in the actual decomposition in the range of 5-100 Hz. 156

Figure 62. Representative (a) Real and (b) imaginary component of a complex wavelet family and (c) their corresponding amplitude spectrum used in spectral reconstruction of the wedge models in **Figure 51**. The bandwidth of each spectral component is twice as long as each component from **Figure 61**. A total of 95 components were computed in the actual reconstruction in the range of 5-100 Hz. 157

Abstract

During the past eight years, north-central Oklahoma has experienced a significant increase in seismicity. Although the disposal of large volumes of wastewater into the Arbuckle Group-basement system has been statistically correlated to this increased seismicity, our understanding of the actual mechanisms involved is somewhat superficial. To address this shortcoming, I served as the geophysicist in an integrated study to characterize and model the Arbuckle-basement system to increase our understanding of the subsurface dynamics during the wastewater-disposal process. I constructed a 3D geological model that integrates 3D seismic data, well logs, core measurements and injection data. Poststack-data conditioning and seismic attributes provided images of faults and the rugose top of the basement, while a modified-Hall analysis provided insights into the injection behavior of the wells. Using a Pareto-based history-matching technique, I calibrated the 3D models using injection rate and pressure data. The history-matching process showed the dominant parameters to be formation-water properties, permeability, porosity, and horizontal anisotropy of the Arbuckle Group. Based on the pressure buildup responses from the calibrated models, I identified sealing and conductive characteristics of the key faults. My analysis shows the average porosity and permeability of Arbuckle Group to be approximately 7% and 10 mD, respectively over the study area. The simulation models also showed pockets of non-uniform and large pressure buildups in these formations indicating that faults play an important role in fluid movement within the Arbuckle Group-basement system.

To further improve our understanding of the basement in Oklahoma, its plumbing system and tectono-thermal history, I depth-migrate a 3D pre-stack seismic volume in north central Oklahoma where recent studies have highlighted the presence of basement igneous sills (BIS), expressed as intra-basement seismic reflectors (IBR), possibly associated with the Mid-Continent

Rift. The depth-migrated data allows me to better delineate the geophysical characteristics of the BIS, and I integrate it with outcrop observations and well log data to constrain our geological interpretations. Further, I create geologically-realistic 2D seismic forward models of the sills to assess if their synthetic seismic attribute response can be utilized for improving current interpretation workflows for igneous intrusions in other regions. I find that (1) depth-migration of the seismic volume provides better imaging of the geometry of the BIS, (2) 2D forward models show that distinct geometries for fault-controlled basement sill steps can be distinguished in seismic reflection data and (3) salient geometric features of the BIS observed in outcrops are consistent to those in the depth-migrated seismic data.

To better delineate such basement intrusions, I evaluate current limits and assumptions of seismic resolution. Beginning in 1973 with Widess' analysis of reflector wedge models, the conventionally understood limit of vertical seismic resolution has been $\lambda/4$ for noise contaminated data. However, this model and resolution limits do not represent the full range of models that might be present in nature. In this dissertation, I examine three algorithms designed to increase the limit or at least quantify vertical seismic resolution: spectral balancing, bandwidth extension and the Hölder exponent. I find that spectral balancing provides a useful, but limited improvement of seismic resolution. I find that although bandwidth extension attempts to resolve beds below tuning frequencies by extending the magnitude spectrum, the corresponding phase spectrum interference patterns are not properly unraveled. Events that were previously resolved appear sharper, while those that were not are now corrupted. The goal of the Hölder exponent is to use the shape of the magnitude spectrum to characterize the underlying reflectivity as being blocky, spikey, or smooth. My work shows that the resolution of thin beds below tuning remains an important problem in the geophysics community that is often poorly understood and for which permanent solutions are still to be found.

Chapter 1: Introduction

Since the 1880s, the state of Oklahoma has experienced a limited but consistent level of seismicity (earthquakes.ok.gov). However, in the last decade, north-central Oklahoma has seen a drastic increase in the number of earthquake events which cannot be solely attributed to natural causes, unlike any other state in the USA. Jacobs (2016) reported more than 2,500 seismic events with >2.5 Richter magnitude between 2010 and 2015 in Oklahoma. Such increase in seismicity has been linked with wastewater disposal from Class II wells (Zoback, 2010; Horton, 2012; Kim, 2013; McGarr et al., 2015; and Walters et al., 2015) (Figure 1).

The United States Environmental Protection Agency (EPA) defines Class II wells as those used to inject fluids associated with oil and gas into the subsurface. In general, permeable formations are the targets of such wells. In north-central Oklahoma, most of the wastewater is disposed of in the high porosity, high permeability, and often karsted Arbuckle group (Walsh and Zoback, 2015). These authors hypothesize that this formation in in hydraulic communication with the underlying crystalline basement and increases in pressure in the Arbuckle Group are transmitted to the latter, thereby modifying the ambient stress field and facilitating slippage along pre-existing zones of weakness.

Although different authors have established spatio-temporal correlations between wastewater injection and earthquakes across the USA and other countries (Evans, 1966; van der Baan and Calixto, 2017; Walsh and Zoback, 2015), there are still many exceptions found across most places, which highlights that there is still a poor understanding of the mechanisms of earthquake triggering. However, what is clear is that geological variability controls the occurrence of such events and basement rocks in Oklahoma are not homogeneous (Elebiju et al., 2011; Shah and Keller, 2017; Chopra et al., 2018; Kolawole et al., 2018).

Most of Oklahoma's basement rocks are comprised of Precambrian igneous and metamorphic rocks of about 1.4 billion years ago (Johnson, 2008). For north-central Oklahoma, understanding the tectonic history and development of its igneous and metamorphic rocks can offer clues to better study its seismicity from the last decade. In particular, sheet igneous intrusions, such as the ones found across Oklahoma's basement (Chopra et al., 2018; Kolawole et al., 2019) are of special interest for understanding the systems that are crucial for monitoring of volcanoes (Galland, 2012) and for potential hydrocarbon exploration in intruded basins (Schofield et al., 2015; Senger et al., 2017). Due to their relatively high acoustic impedance contrast, igneous intrusions are easily recognized in seismic volumes where they intrude in sedimentary rocks (Magee et al., 2013; Magee et al., 2016; Infante and Marfurt, 2017; Eide et al., 2017). However, in order to visualize such intrusions in basement rocks in Oklahoma from seismic data, important consideration need be done regarding seismic resolution.

Seismic resolution is a measure of our capacity to visualize an object in seismic and how large such object must be to be properly imaged. Therefore, seismic resolution and its limits is an important factor to consider in any exploration or development endeavor. One of the most common used limits to seismic resolution was established by Widess (1973), who defined the resolving power to be $\lambda/8$ for noise-free data, but with a more practical limit of $\lambda/4$ for noise-contaminated data. Later, with the advent of spectral decomposition, it became apparent that the assertion of $\lambda/8$ as the lower limit for seismic resolution was incomplete (Chung and Lawton, 1995; Chopra et al., 2006). Chopra et al., (2006) showed that when the top and the base reflectivity coefficients of a layer are not exactly equal and opposite, as in the Widess (1973) model, the peak frequency decreases with thickness even below $\lambda/8$. Since there are changes of seismic amplitude and frequency below the conventional limits established by Widess (1973), it follows that thicknesses below tuning limits can also be inferred. Several authors have since developed different algorithms to improve seismic resolution (Smith et al., 2008; Li and Liner, 2008; Puryear and Castagna, 2008; de Matos and Marfurt, 2011).

This dissertation seeks to address the challenges mentioned thus far, and so is structured as follows:

In Chapter 2, I apply a 3-step data-integration workflow to understand plumbing mechanisms in the Arbuckle-Basement waste-water disposal system in Payne County, Oklahoma. The first step includes establishing a structural and stratigraphic framework for the basement, Arbuckle Group and overlying strata and constructing a 3D reservoir model of the subsurface geology. The second step includes analyzing and filtering injection-well data. The third step includes history matching to evaluate whether key faults act as fluid conduits or seals and discussing the limitations to the methodology presented. This chapter represents a group effort for which the author of this manuscript served as leader, working personally on the structural and stratigraphic framework for the basement, and aiding in the development of the rest of the steps mentioned along its co-authors.

In Chapter 3, I utilize synthetic seismograms created from outcrop observations in south Oklahoma to study the behavior and interactions of mafic sills in a felsic host rock. I study the seismic attribute response of such intrusions to evaluate if they can be used for improving current interpretation workflows for a real seismic volume from north-central Oklahoma. I reprocess and depth-migrate such seismic volume through a more careful velocity model building to enhance the seismic image of basement intrusions within that data set. I find that the model’s seismic attribute response can be used to recognize real igneous intrusions in the basement in Oklahoma. Depth migration improves interpretation results, by recognizing geological structures not revealed otherwise. This chapter also represents a group effort for which the author of this manuscript served as leader, personally performing depth migration, velocity analysis, synthetic generation, and attribute modeling and interpretation.

In Chapter 4, I evaluate three methods developed for either extending or quantifying the resolving problem of recorded seismic data. I review the assumptions of each of the four methods and evaluate their effectiveness on a wedge model. After, I apply these algorithms to real seismic data from the Diamond-M field in Texas and compare the seismic-to-well ties before and after the application. This chapter represents a group effort for which I served as leader, performing the algorithm review on wedge models and applying them to the data set from Diamond-M field.

In Chapter 5, I summarize the results of the current dissertation. The modeled properties for the Arbuckle-Basement waste-water disposal system can have implications in other modeling efforts performed within the region for better understanding mechanisms involved in induced seismicity in Oklahoma. The igneous intrusions modeling and interpretation workflow presented can be implemented in other regions where such features may affect petroleum system elements in place. Depth migrating seismic volumes can also enhance the information retrieved from it, provided that an appropriate velocity model has been carefully created beforehand. Finally, it is evident than conventionally established limits for seismic resolution are inadequate to handle many cases encountered in most exploration and production campaigns. Therefore, although improving seismic resolution below tuning is still further down the road, I have evaluated different algorithms that hold potential to breaking current limits and allowing for more productive and safer E&P endeavors.

References

Chopra, S., J. P. Castagna, and O. Portniaguine, 2006, Seismic resolution and thin-bed reflectivity inversion: Canadian Society of Exploration Geophysicists Recorder, **31**, 19-25.

Chopra, S., L. Infante-Paez, and K. J. Marfurt, 2018, Intra-basement intrusions in the STACK area of Oklahoma: AAPG Explorer, May Geophysical Corner. https://explorer.aapg.org/story/articleid/46763/intra-basement-intrusions-in-the-stack-area-of-oklahoma) (Accessed January 3, 2019).

Chung, H., and D. C. Lawton, 1995, Frequency characteristics of seismic reflections from thin beds: Canadian Society of Exploration Geophysicists Recorder, **31**, 32-37.

de Matos, M. C., and K. J. Marfurt, 2011, Inverse continuous wavelet transform “deconvolution”: 81st Annual International Meeting, SEG, Expanded Abstracts, 1861–1865

Eide, C. H., N. Schofield., I. Lecomte., S. Buckley., and J. A. Howell, 2017, Seismic interpretation of sill complexes in sedimentary basins: implications for the sub-sill imaging problem: Journal of the Geological Society of London, **175**, 193-209, https://doi.org/10.1144/jgs2017-096

Elebiju, O. O., S. Matson, G. R. Keller, and K. J. Marfurt, 2011, Integrated geophysical studies of the basement structures, the Mississippi chert, and the Arbuckle Group of Osage County region, Oklahoma: AAPG Bulletin, **95**, 371–393.

Evans, D. M., 1966, The Denver area earthquakes and the Rocky Mountain Arsenal disposal well: Mtn. Geologist, v. 3. no. 1, 23-26.

Galland. O., 2012, Experimental modelling of ground deformation associated with shallow magma intrusions: Earth and Planetary Science Letters, **317**, 145-156

Horton, S., 2012, Disposal of hydrofracking waste fluid by injection into subsurface aquifers triggers earthquake swarm in central Arkansas with potential for damaging earthquake: Seismol. Res. Lett. **83**, 250–260.

Infante-Paez. L., and K. J. Marfurt, 2017, Seismic expression and geomorphology of igneous bodies: A Taranaki Basin, New Zealand case study: Interpretation, **5**, SK121-SK140, https://doi.org/10.1190/int-2016-0244.1

Jacobs, T., 2016, Seismic Shifts in Oklahoma Lead to Stricter Regulations: J Pet Technol **68** (5), 44–48, SPE-0516-0044-JPT. https://doi.org/10.2118/0516-0044-JPT.

Johnson, K. S., 2008, Geologic History of Oklahoma, Educational Publication 9

Kim, W., 2013, Induced seismicity associated with fluid injection into a deep well in Youngstown, Ohio: J. Geophys. Res. **10**.

Kolawole, F., C. Johnston, J. Chang, K. J. Marfurt, Z. Reches, and B. M. Carpenter, 2018, Characterization of pre-existing structures in the basement of Oklahoma with implications for induced seismicity: GSA Annual Meeting in Indianapolis, Indiana Paper No. 158-6.

Kolawole, F., B. M. Carpenter, and M. Simpson-Turko, 2019, The intra-basement reflectors in the STACK area of Oklahoma: What are they really?: AAPG Explorer, April Geophysical Corner.

Li, C., and C. Liner, 2008, Wavelet-based detection of singularities in acoustic impedances from surface seismic reflection data: Geophysics, 73, no. 1, V1–V9

Magee. C., C. A. L. Jackson., and N. Schofield, 2013, The influence of normal fault geometry on igneous sill emplacement and morphology: Geological Society of America, **41**, 407-410.

Magee, C., J. D. Muirhead, A. Karvelas, S. P. Holford, C. A. Jackson, I. D. Bastow, N. Schofield, C. T. Stevenson, C. McLean, W. McCarthy, and O. Shtukert, 2016, Lateral magma flow in mafic sill complexes: Geosphere, **12**, 809–841, doi: 10.1130/GES01256.1.

McGarr, A., B. Bekins, N. Burkardt, J. Dewey, P. Earle, W. Ellsworth, S. Hickman, A. Holland, E. Majer, J. Rubinstein and A. Sheehan, 2015, Coping with earthquakes induced by fluid injection: Science 347, no. 6224, 830–831, doi: https://doi.org/10.1126/science.aaa0494

Puryear, C.I. and J. P. Castagna, 2008, Layer-thickness determination and stratigraphic interpretation using spectral inversion: theory and application: Geophysics, **73**, R37-R48.

Senger. K., J. Millett., S. Planke., K. Ogata., C. H. Eide., M. Festoy., O. Galland., and D. A. Jeram., Effects of igneous intrusions on the petroleum system: a review: First Break, **35**, 47-56.

Shah. A. K., and G. R. Keller, 2017, Geologic influence on induced seismicity: Constraints from potential field data in Oklahoma: Geophysical Research Letters, **44**, 152-161.

Schofield. N., S., S. Holford. et al., 2015, regional magma plumbing and emplacement mechanisms of the Faroe-Shetland Sill Complex: implications for magma transport and petroleum systems within sedimentary basins: Basin research, **29**, 41-63.

Smith, M., G. Perry, J. Stein, A. Bertrand, and G. Yu, 2008, Extending seismic bandwidth using the continuous wavelet transform: First Break, **26**, 97-102.

van der Baan, M., and F. J. Calixto, 2017, Human-induced seismicity and large-scale hydrocarbon production in the USA and Canada: Geochem. Geophys. Geosyst., 18, 2467-2485

Walsh, F. R., and M. D. Zoback, 2015, Oklahoma's recent earthquakes and saltwater disposal: American Association for the Advancement of Science, 1, No. 5.

Walters, R., M. Zoback, J. Baker and G. Beroza, 2015, Characterizing and responding to seismic risk associated with earthquakes potentially triggered by saltwater disposal and hydraulic fracturing: Seismol. Res. Lett. **86**, no. 4, doi: https://doi.org/10.1785/0220150048.

Widess, M., 1973, How thin is a thin bed?: Geophysics, **38**, 1176-1180.

Zoback, M. D., 2010, Reservoir Geomechanics, Cambridge University Press, 505p.

Figures

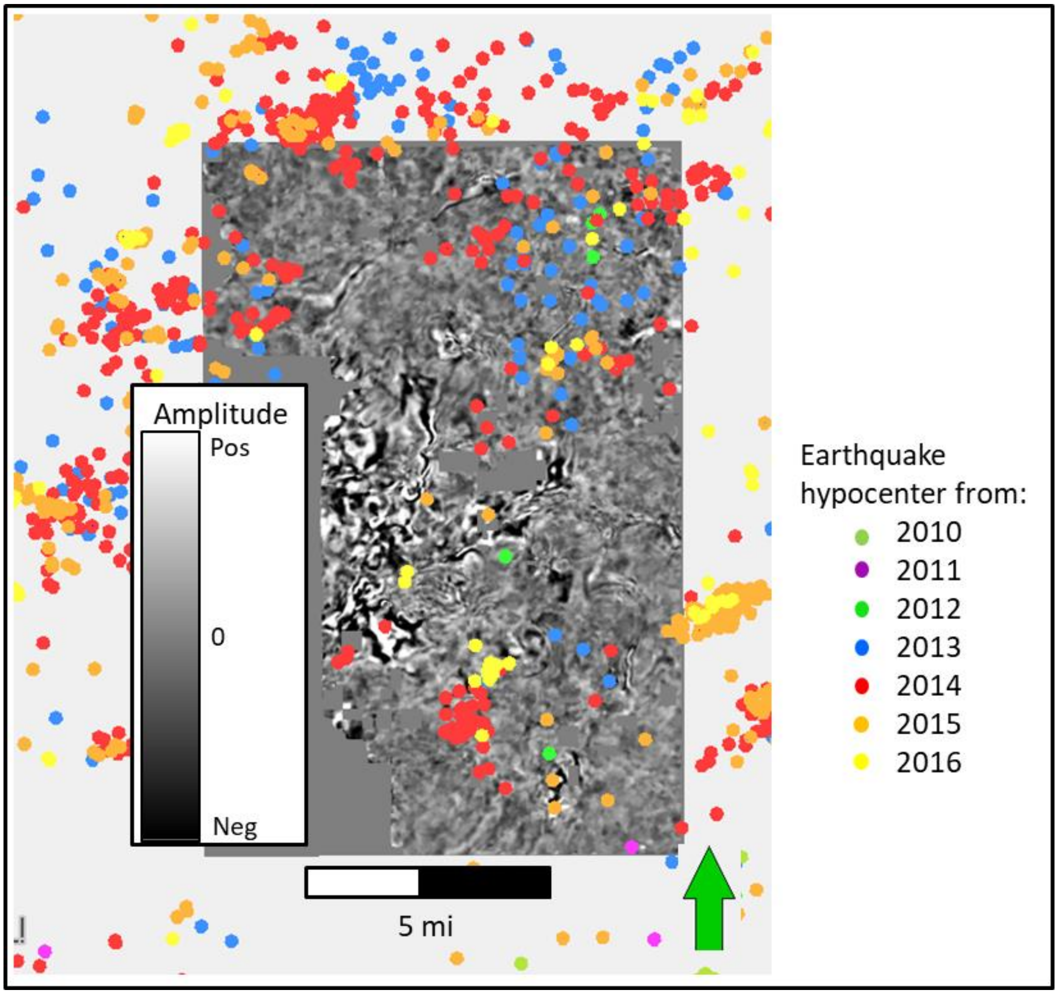
Amplitude
Pos
0
Neg
5 mi
Earthquake hypocenter from:
● 2010
● 2011
● 2012
● 2013
● 2014
● 2015
● 2016

Figure 1. Map view of seismic survey for current study in Payne County, Oklahoma, with hypocenter of earthquakes from 2010 through 2106 color coded by year. Some clusters of events can be observed in the southern portion of survey and outside of it.

Chapter 2: Characterization of Arbuckle-Basement waste-water disposal system, Payne county, northern Oklahoma

Abstract

During the past eight years, north-central Oklahoma has experienced a significant increase in seismicity. Although the disposal of large volumes of wastewater into the Arbuckle Group-basement system has been statistically correlated to this increased seismicity, our understanding of the actual mechanisms involved is somewhat superficial. To address this shortcoming, I initiated an integrated study to characterize and model the Arbuckle-basement system to increase our understanding of the subsurface dynamics during the wastewater-disposal process. I constructed a 3D geological model that integrates 3D seismic data, well logs, core measurements and injection data. Poststack-data conditioning and seismic attributes provided images of faults and the rugose top of the basement, while a modified-Hall analysis provided insights into the injection behavior of the wells. Using a Pareto-based history-matching technique, I calibrated the 3D models using injection rate and pressure data. The history-matching process showed the dominant parameters to be formation-water properties, permeability, porosity, and horizontal anisotropy of the Arbuckle Group. Based on the pressure buildup responses from the calibrated models, I identified sealing and conductive characteristics of the key faults. My analysis shows the average porosity and permeability of Arbuckle Group to be approximately *7%* and *10* mD, respectively. The simulation models also showed pockets of non-uniform and large pressure buildups in these formations indicating that faults play an important role in fluid movement within the Arbuckle Group-basement system.

As one of the first integrated investigations conducted to understand the potential hydraulic coupling between the Arbuckle Group and the underlying basement, I show the need for both improved data recording and additional data collection. In particular, I recommend that operators wishing to pursue this type of analysis record their injection data on a daily rather than averaged basis. A more quantitative estimation of reservoir properties requires the acquisition of P-wave and dipole sonic logs in addition to the commonly acquired triple-combo logs. Finally, to better quantify flow units with the disposal reservoir, I recommend that operators acquire sufficient core to characterize the reservoir heterogeneity.

Introduction

According to The Office of the Secretary of Energy and Environment (Oklahoma), the State of Oklahoma has experienced limited but consistent level of seismicity in the recorded history dating back to 1882 (earthquakes.ok.gov). However, north-central Oklahoma has experienced a recent and dramatic rise in the number of earthquake events. This cannot be solely attributed to the natural causes. Walsh and Zoback (2015) provide a discussion of the increase in seismicity (Figure 2**Error! Reference source not found.**). They mentioned that no other state has witnessed an increase in seismicity as much as Oklahoma in the recent years. Jacobs (2016) reported more than *2,500* seismic events with *>2.5* Richter magnitude between 2010 and 2015 in Oklahoma.

Multiple studies including but not limited to Zoback (2010), Horton (2012), Kim (2013), McGarr et al. (2015), and Walters et al. (2015) indicate that the seismicity is linked with the wastewater disposal. To address this issue, the Oklahoma Corporation Commission implemented a “stoplight” plan of action that required the reduction (a yellow light) or cessation (a red light) of injected wastewater volumes and a stop light for fracking. Since the plan has been implemented, there has been a reduction in earthquakes exceeding magnitude 3 or greater from *903* in 2015, to *623* in 2016, *302* in 2017, and *196* in 2018 (Tulsa World, 2019). This decrease in seismicity occurred while the volume of oil produced increased from *166* MMBBL in 2015 to *192* MMBBL in 2018 (EIA, 2019). The increased cost of wastewater disposal, public relations concerns, and new exploration opportunities have shifted oil and gas production from the high water-cut Mississippian Limestone play of north-central Oklahoma (e.g., Matson, 2013) to the lower water-cut STACK and SCOOP plays of central and south-central Oklahoma (Pickett, 2018). Outside of Oklahoma, hydraulic-fracturing operations have been attributed to be the primary cause of induced seismicity (Holland, 2013; B ritish Columbia Oil and Gas Commission, 2011; Friberg et al., 2014; Walters et al., 2015). Although several seismic events in Oklahoma have been linked to hydraulic-fracture stimulation (Holland, 2013), none have been reported in north-central Oklahoma where most seismic events have occurred and where my study focusses. Therefore, this study does not focus on hydraulic-fracture-induced seismicity.

The United States Environmental Protection Agency (EPA) designates Class II wells as those used to inject fluids associated with oil and gas into the subsurface. In general, permeable formations are the target of Class II wells. According to the U.S. Geological Survey (www.usgs.gov), *40,000* out of *150,000* Class II wells operating in the USA are used for oil and gas wastewater (primarily brine) disposal. Other class II wells include those used for enhanced recovery and hydrocarbon storage. The total produced water volume in the USA exceeded *20* billion stock-tank barrels (STB) in 2007 as reported by Clark and Veil (2009). Enhanced recovery operations consumed over *55%* of this water, while about *39%* of the water was disposed of through waste water injection wells. A small fraction of these disposal wells has caused induced seismicity, thereby triggering a large concern among the public and governmental organizations. This increase in seismicity has led federal and state bodies to find ways to mitigate the risk of induced seismicity. The State of Oklahoma Underground Injection Control division recognizes three necessary components for significant injection-induced seismicity: 1) sufficient pressure buildup from disposal activities, 2) the presence of faults, and 3) a pathway allowing the increased pressure to communicate with the faults.

Resource plays such as the Mississippian Limestone of Oklahoma and Kansas are characterized by up to *95%* hypersaline water production. Although the entire State of Oklahoma has thousands of water disposal wells, it is only north-central Oklahoma that has experienced a recent increase in seismicity. Walsh and Zoback (2015) state that in north-central Oklahoma, most of wastewater is disposed of in the high porosity, high permeability, and often karsted Arbuckle Group. Also, these authors hypothesize that this formation is in hydraulic communication with the underlying crystalline basement. Increases in pressure in the Arbuckle Group are transmitted into the basement, thereby modifying the ambient stress field, facilitating slippage along preexisting zones of weakness. The exact details of such pressure transmission are unknown, with some scientists suggesting fluid flow into the basement along faults and others proposing a somewhat simpler loading process, since pressure is transmitted much more quickly than fluid.

Although different authors have established spatio-temporal correlations between wastewater injection and earthquakes across the USA and other countries (Evans, 1966; van der Baan and Calixto, 2017; Walsh and Zoback, 2015), there is still a poor understanding of the mechanisms of earthquake triggering in north-central Oklahoma. However, one aspect is clear; geological variability controls the occurrence of such events and basement rocks in Oklahoma and is not homogeneous (Elebiju et al., 2011; Chopra et al., 2018; Kolawole et al., 2018). To further investigate these issues, data for this study include modern wide-azimuth 3D seismic data volumes, well logs, and injection volumes in Payne County, Oklahoma. These data were used to provide a better understanding of the subsurface geology and ideally, insight on how to mitigate future seismic events. I conduct, to my knowledge, the first integrated, multidisciplinary characterization study of the Arbuckle Group-basement wastewater disposal system.

We begin this paper with a review of the geologic setting and the data available, followed by a summary of the 3-step data-integration workflow. The first step includes establishing the structural and stratigraphic framework for the basement, Arbuckle Group and overlying strata and constructing a 3D reservoir model of the subsurface geology. The second step includes calibrating and analyzing injection-well data. The third step includes history matching where I evaluate whether key faults act as fluid conduits or seals and where I also discuss some of the limitations for the methodology presented. Each of these steps required perturbing the other two steps. I conclude with a summary of my results, a discussion of the strengths and weaknesses of my analysis, and a list of conclusions including recommendations for data acquisition for improved wastewater reservoir characterization studies.

Geologic setting

The Arbuckle Group of central and northern Oklahoma was deposited during the Cambrian and Ordovician as an extensive carbonate platform that covered most of the region. Strata in the study area are *100s* to *1,000s* of feet thick and were altered, in part, by fracturing, dolomitization, and karstification processes. Cambrian and Ordovician carbonates are underlain by *50 - 100* ft of interbedded sandstones and dolomites of the Reagan Sandstone (Stringer, 1958) which in turn lies upon faulted Pre-Cambrian/Cambrian granites and rhyolites that form the shallow part of the basement throughout much of Oklahoma (Johnson, 1991). The heavily fractured and karsted carbonate formations have been the main disposal units for salt-water disposal (SWD) wells throughout much of Oklahoma (Murray, 2015).

Methods

Our first objective was to construct a stratigraphic and structural framework consistent with our understanding of the stratigraphic and tectonic history of the area that honored the well log, core, and 3D seismic data.

3D Seismic Processing, Interpretation, and Attribute Analysis

In this study, I processed and interpreted a wide-azimuth, high-fold 3D-seismic survey acquired in Summer 2014 using state-of-the-art processing techniques, including modern surface-consistent statics, careful velocity analysis, and pre-stack time migration to optimally focus on the shallower Mississippi Lime and Red Fork exploration targets. The image of the deeper, stratigraphically complex Arbuckle Group is excellent, while that of the still deeper more structurally complex basement is sub-optimal. Without access to the original shot gathers at the time, I was unable to reprocess the data using pre-stack depth migration to account for the lateral velocity variation of the overburden (Figure 5a). Nevertheless, I was still able to improve the signal-to-noise ratio (though not the focusing and position) of these deeper reflectors using a structure-oriented-filter to remove noise components cutting across structural dip, along with spectral balancing. Next, guided by the data owner, I applied a phase shift of *-114*° to properly allocate reflectors sign to the corresponding lithologies (Figure 5b).

A suite of different seismic attributes was computed to characterize the system, using the software developed at the University of Oklahoma (AASPI, 2017). Figure 6 shows a suite of horizon slices through three of the attributes that proved to be most useful in mapping structural features along the top Arbuckle Group.

Coherence, which normally delineates faults that exhibit finite reflector offset, is the workhorse of most modern 3D seismic structural interpretation workflows (Bahorich and Farmer, 1995; and Chopra and Marfurt, 2007). However, in this study, the resulting images were disappointing, as the chaotic nature of the basement does not permit for faults to be clearly delineated by this attribute (Figure 6b). Along the top Arbuckle and top basement where the seismic image quality is excellent, the vertical fault displacements are either too small, or alternatively, too smeared (where the displacement is distributed by conjugate faults over a finite zone) to be delineated by coherence. Curvature provided a better delineation of some faults (Figure 6c and Figure 6d). An alternative geologic interpretation is that many of these faults are strike-slip in origin, where the deformation is accommodated by Riedel shears and flexures that exhibit little vertical offset, forming a fault damage zone.

In contrast to coherence, structural curvature “sees” such smeared images as a flexure (Figure 6c and Figure 6d). Numerically, curvature is defined in two dimensions as the inverse of the radius of a circle tangent to and fitting a curve, with anticlines having positive curvature and synclines having negative curvature. Planar features exhibit zero curvature (Chopra and Marfurt, 2007). For a normal fault, the footwall will exhibit a positive curvature anomaly (an antiform) whereas the hanging wall will exhibit a negative curvature anomaly (a synform). In general, these two curvature anomalies will bracket a normal fault. Analyzing the strike-slip El Reno Fault *65* miles west of the study area, Liao et al. (2017) found that curvature could delineate not only Riedel shears, but also a suite of rhombochasms forming a wide damage zone. Most-positive curvature will delineate the axis of up thrown structures.

Aberrancy measures the lateral change (or gradient) of curvature along an interpreted or inferred surface. Whereas curvature anomalies will bracket a fault, aberrancy will track the coherence anomaly and fall between the most-positive curvature anomalies defining the footwall and the most-negative curvature anomalies defining the hanging wall. For this reason, aberrancy can delineate faults whose throw falls below seismic resolution (Qi and Marfurt, 2017). Aberrancy is the third derivative of structure, highlighting discontinuities with a small vertical displacement. I can use this attribute to further characterize discontinuities by their azimuthal orientation (Figure 7). Seismic azimuth is perpendicular (±*90*°) to the geological strike and defined as 0° from the North, increasing in the clockwise direction to a maximum of *359*°, e.g. if the structural strike of a seismic feature is East-West dipping to the South, its corresponding azimuth is *180*°

In general, seismic attributes such as coherence, curvature, and aberrancy provide excellent images of subtle features in well-imaged seismic data volumes. In contrast, deeper within the basement, pre-stack time-migration operator aliasing artifacts and misalignment of reflectors with fault edges makes most attribute analyses difficult.

Well-Log Cross-Sections and Formation Correlation

Well-log data were used to interpret formation tops and to create a grid of structural and stratigraphic cross sections. The interpreted formations included the Ordovician Arbuckle Group through the Pennsylvanian Oolagah ("Big Lime") Formation (Figure 8). Structure-contour and isopach maps were generated for the Arbuckle Group and each of the other overlying sedimentary formations.

Structure-Contour and Isopach Mapping

We created structure-contour maps (surfaces) for the formations that overly the Arbuckle Group using only interpreted well-log tops. I could not use 3D seismic data for these overlying formations due to restrictions based on the seismic licensing agreement. I constructed the structure-contour map for the top of Arbuckle Group from both formation tops in *29* wells and the corresponding depth-converted seismic horizons using least squares to fit the seismic horizon trend to the well tops map. I followed a similar approach for the top of the basement. In this case, however, since there was no marker for the basement in most wells, because it is not an exploration target, I assumed that for each well, the drilling stopped once the basement rock was hit. With this I approximated the depth of the basement to the TD of the wells. Figure 9 shows the surface constructed for the Arbuckle Group top is structurally highest in the northeast and dips towards the southwest. I also constructed an isopach map for the Arbuckle Group by subtracting the basement top depths from the Arbuckle top depths.

Construction of a 3D Reservoir Model

Interpreted faults (or fault surfaces) from the 3D seismic data do not exhibit significant vertical offset; therefore, I did not explicitly include them in the 3D reservoir model grid. However, I subsequently mapped porosity trends using the fault surfaces within the Arbuckle-basement interval and included the faults in the fluid-flow simulation model for calibration. I included a part of the basement (*500*-ft or *152.4* m thick interval) in the 3D simulation grid below the Arbuckle Group. The choice for the *500* ft interval of basement in the model was due to lack of well log deep into the Basement, and also because I do not expect pressure effects to extend too deep into the basement. I included the Arbuckle Group, as well as the Simpson and Viola formations in the 3D reservoir model grid based on the interpreted surfaces. The 3D grid consists of cells with aerial dimensions of *500* ft by *500* ft (*152* m by *152* m) and an average layer thickness of *3* ft (*0.9* m) resulting in a total of approximately *6.5* million cells.

Porosity Modeling

Upscaled total porosity logs (based on neutron and density porosity logs) and variogram parameters constrained the 3D porosity models. Core data do not exist within the study area. I calculated the total porosity logs (ϕ_t) using the root-mean-square method using the NPHI and DPHI curves. The total porosity logs were upscaled to the cell dimensions and modeled using variogram-based Sequential-Gaussian simulation (SGS). For the Arbuckle Group and shallower formations, the variogram ranges were set to *7,000* ft (*2,134* m) for both horizontal directions and *10* ft (*0.6* m) for the vertical direction. Due to the lack of well-log data for the basement, I modeled the porosity distribution in the basement assuming that the porosity for igneous and metamorphic lithologies is in general greater near the faults and essentially zero in non-faulted areas. This porosity distribution was computed using a “distance-to-object” property using commercial software in which the interpreted fault surfaces are the objects. This approach resulted in porosity values of $\varphi=6\%$ near fault surfaces and linearly decreasing to $\varphi=0\%$ *3,000* ft away from the fault

Permeability Modeling

The porosity models, discussed above, and a Buckle's (Schlumberger, 1991a) relationship between calculated irreducible water saturation and porosity constrained the three-dimensional permeability models. Buckle's method estimates the irreducible water saturation, Sw_{irr}, using an empirical relationship between the effective porosity, φ_e, the fractional volume of shale, Vsh, and the Buckle's number κ_{Buckle}:

$$Sw_{irr} = \frac{\kappa_{BUCKL}}{\varphi_e(1-V_{sh})} \quad . \tag{1}$$

V_{sh} is commonly calculated using the gamma ray log. In this case, V_{sh} was set to be zero to assume only the presence of water.

After irreducible water saturation was estimated, qualitative permeability estimates were calculated using the Tixier Equation

$$\kappa = \left(250\frac{\varphi_e^3}{Sw_{irr}}\right)^2 , \tag{2}$$

and the Timur Equation (Schlumberger, 1991b).

$$\kappa = \left(100\frac{\varphi_e^{2.25}}{Sw_{irr}}\right)^2 , \tag{3}$$

which are a function of the irreducible water saturation and the total porosity model. Three iterations of this process using **equations 2** and **3** were run using $\kappa_{BUCKL} = 0.01$ for vuggy, $\kappa_{BUCKL} = 0.005$ for crystalline, and $\kappa_{BUCKL} = 0.001$ for fractured rocks, corresponding to the three possible rock matrix types. An additional six models were run assuming *100%* water saturation and the absence of any hydrocarbons. A vuggy to fine vuggy matrix was assumed for the Arbuckle Group.

Analysis of the Injection Data

I investigated the well performance of the *29* disposal wells within the seismic survey area, analyzing the daily injection rates, surface-tubing pressures and well-completions data. I carefully examined the available data to identify anomalous entries. I either corrected (whenever possible) or removed the anomalous data from further analyses. Completions reports provided the perforation depths for all the wells. To perform the analysis at subsurface conditions, I converted the wellhead pressures to bottom-hole pressure using commercial software. This conversion also entailed carrying out sensitivity analyses using salinity, multiphase-flow correlations and water-injection temperature in order to identify any artifacts introduced in this pressure conversion process.

I employed the Modified-Hall Analysis (MHA) described by Izgec and Kabir (2011) to investigate the well performance of the *29* disposal wells. Average ambient pressure around the wells is required to calculate the Hall Integrals. Next, I used Silin slope analysis (Silin et al. 2005) to calculate the ambient reservoir pressure. Note that Silin analysis yields reliable result only with injection data within a transient flow regime. I identified the flow regimes using material-balance-time diagnostics plots (Anderson and Mattar, 2004). Material balance time is the ratio between the cumulative injection and the instantaneous injection rates. A log-log plot of the daily injection rate against the material-balance time helps diagnose the well-flow regimes. The steady-state regime corresponds to unit slope in the resulting log-log plot. Ascertaining the onset of the steady-state regime provides a means to identify the appropriate range for pressure and injection data for subsequent Modified Hall Analysis (MHA).

In MHA, I plot Hall integrals and their derivatives (modified Hall derivatives) with respect to cumulative injection (Izgec and Kabir, 2011) against the cumulative injection. One can consider Hall integral a measure of injection-pressure buildup with time, while the modified Hall derivatives indicate the rate of pressure buildup with incremental injection. In a normal injection scenario, both curves (Hall integrals and the modified Hall derivatives) will have similar slope against cumulative injection. Whenever the two curves deviate away from each other, normal injection ceases. If the slope of the Hall derivatives increases faster than the Hall integral, the well is struggling to inject fluid causing the pressure to build up rapidly. This rapid pressure builds up is an injectivity-loss scenario: for instance, formation plugging and any other kind of formation damage. In contrast, if the slope of the Hall derivatives declines rapidly compared to the Hall integrals, the injected fluid has found less resistant flow path and the pressure is not building up any further. In fact, the disposal well may experience a pressure decline at this point. This decrease in pressure is a typical disposal well-pressure behavior after formation-fracturing has taken place.

We diagnosed the injectivity pattern of all *29* disposal wells using MHA diagnostics explained above. Finally, I formed clusters of wells with similar injection patterns. This provided insights into the history-matching of the simulation model discussed next.

History-Matching Methodology

We considered the Viola, Simpson, Arbuckle Group and basement formations as flow units in the geological model. The model has *500* ft by *500* ft grid cells, *164* grid points in the x (north), *217* grid points in y (east), and *185* grid points in the z (vertical) directions, resulting in a *6.5* million cell model that extended laterally approximately *66,500* ft. × *98,300* ft. Figure 10 shows the schematic of the simulation model.

After the creation of the major formations, I assigned geological porosity and permeability parameters to the simulation model. I assigned rock properties based on the type of the formations. With respect to the initial fluid distribution, I considered the Arbuckle Group and the basement formations to be water-filled. I modeled completions of all *29* wells according to the available completion reports. In the simulation, I employed well injection rates and bottom-hole pressures for the period between January 2005 and May 2016. I included the faults delineated from the seismic interpretation in the simulation models.

We used Pareto-based history-matching process, first identifying regions of interest for history-matching where the Arbuckle Group formation is the main disposal zone of interest in my study. I used both bottom-hole pressure and injection rates as the model response variables for the history-match.

The next step was to identify uncertain parameters for history matching. In this study, I used permeability, horizontal and vertical anisotropy, porosity and compressibility of the Viola, Simpson, Arbuckle Group and basement formations as the uncertain parameters. I also considered formation-water properties such as compressibility, viscosity, density and formation-volume factor to be uncertain. After attaining moderate history match, I adjusted the injection-well productivity multipliers.

We employed reasonably broad ranges for all the uncertain parameters at the start of history-matching. At each stage of history matching, I performed a screening analysis, using Pareto plots to determine those parameters that most impacted the response variables. These key parameters were those associated to the Arbuckle Group formations and wells. Based on the degree of impact, I adjusted the ranges of the values for subsequent stages of history match. I repeated this process until I obtained an acceptable match of the bottom-hole pressure and the injection rates.

Results

Core and Log Properties of the Arbuckle Group

Figure 11displays a type log of the Arbuckle group showing the primary log curves used in picking the formation tops. From left to right I display gamma ray, depth, resistivity, porosity, and bulk density tracks. Gamma ray values in the Arbuckle range from *25-50* API units with a few more clay rich units near the top of the group with porosities consistently ranging from *5-10%*.

Top Basement Structure-Contour Map including Key Faults based on Seismic Data

We analyzed the seismic attributes through the seismic surfaces corresponding to the Arbuckle Group and basement tops. This indicated three major faults from the Arbuckle Group top surface recognized throughout the seismic survey extending into the basement (Figure 12). Fault A, to the north, has an east-west strike orientation, as does fault C to the south, whereas fault B has a strike orientation of northwest-southeast. Additional smaller basement faults were interpreted as potential flow barriers**.**

Arbuckle Group Structure-Contour and Isopach Trends based on Seismic and Well Data

Figure 13 and Figure 14 show the interpreted faults for the basement and Arbuckle Group, respectively. The topography appears to be striking at the same orientation as the middle fault suggesting that that the topographic features are controlled by Fault B.

Figure 15 displays an isopach map of the Arbuckle Group. The interval becomes thicker toward the southwest and northwest, and has an average thickness of approximately *1200* ft.

3D Reservoir Model Grid (3D Stratigraphic and Structural Framework)

Given the absence of seismic control above the top Arbuckle Formation, I used a simple proportional layering scheme, resulting in a grid containing approximately *6.5* million cells. Figure 16 shows the resulting stratigraphic zones from the basement interval to the top of the Viola Limestone. The basement zone was constructed by creating an arbitrary surface *500* ft (*152* m) below the top of basement surface.

Porosity Distribution of the Arbuckle Group and Basement

Porosity in the basement ranges within *0.1* to *6%,* and log-derived porosity in the Arbuckle Group ranges in *5 - 10%.* For the overlying Simpson group, the porosity is significantly higher (*15 - 20%*), whereas in the shallower Viola Limestone porosity ranges between *0.1* to *5%* (Figure 17).

Permeability Distribution of Arbuckle Group and Basement

Permeability in the Arbuckle Group ranges between *1* and *5* mD based on the cores discussed previously. Higher permeability exists in the faulted region in the basement and Arbuckle Group ranging between *10 – 100* mD (Figure 18).

Quality Control and Preconditioning of the Injection Data

The quality of publicly available data can be questionable. Variation in the reporting formats, changes in types of measurements and tools, human-errors - all can contribute to significant variation in record-keeping. For this reason, I used a five-step quality control process:

1. *Data quality analysis*

We first analyzed the pressure and injection-rate data to detect anomalies and rectify them accordingly. Data quality analysis for a random well is shown in Figure 19.

We did not consider pressure data with null records in the study. I also ignored outliers, such as extremely high pressure or injection rates. Possible reasons for null records or anomalous data could be erroneous measurements, meters not operational, lack of calibration, lack of injection, and so forth.

2. *Conversion of wellhead pressures to bottom hole pressures*

For reservoir studies, we require bottom-hole pressure, whereas, we measure pressures at the wellhead. I therefore used well-hydraulics correlation models to convert the surface pressure to bottom-hole pressures. Figure 20 shows the results of the pressure conversion for a well.

We conducted sensitivity analysis of the pressure conversion for water salinity, well-hydraulics correlation models, and injection-water temperature. For the base-case pressure conversion, I used a salinity value of 190,000 ppm as recommended by an operator in the region and a water-injection temperature of 60°F.

3. *Flow-regime identification*

To analyze the well performance, I first identified the flow-regimes to determine the transient or boundary-dominated nature of the injection wells. In the boundary-dominated state, the rates versus material-balance time curve attains unit slope in a log-log plot. Material-balance time is the ratio of the cumulative injection volume and the instantaneous injection rate. Figure 21 shows the material balance time plot of a well indicating the onset of boundary-dominated state by the dashed line.

4. *Estimation of ambient reservoir pressure*

To determine the ambient pressure around the well, I resorted to Silin slope analysis (Silin et al., 2005) since I do not have any other means to determine the pressure at the start of the injection process. Note such analysis only yields an approximation of the ambient pressure. Additionally, I need early-time transient-state pressure and rates data to determine a reasonable estimate of the ambient pressure. Figure 22 shows the Silin-slope plot for a well.

The slope of the line was found to be *2,350* psi, which is the ambient reservoir pressure for this well.

5. *Modified Hall Analysis*

Figure 23 shows the modified Hall analysis carried out on a well. As evident in the figure, the Hall derivatives increase faster than the Hall integral, after a certain point. It indicates normal injection ceases at this point and the well is struggling to inject fluid causing the pressure to build up rapidly.

History-Matching Results

As mentioned previously, I calibrated the simulation model using the observed injection rates and pressure data. Initially, I considered some *50* uncertain parameters through sensitivity runs. The major impactful parameters based on history matching include permeability, porosity and horizontal and vertical anisotropy of the Arbuckle Group, permeability and horizontal anisotropy of the overlying Simpson and the underlying basement formations and water density and viscosity. Such an impact of the Arbuckle Group properties is understandable since most of the waste water injection takes place in the forming formations of this unit, and only a few fault planes intercepting the Arbuckle Group penetrate the overlying Simpson and underlying basement. The Viola formation properties had little impact on the history-matching process, corroborating the limited number of injection-fluid pathways to reach the Viola formation.

We carried out multiple stages of history match focusing on the key wells and formations. The injection-rate match for most of the wells was good. Figure 24 presents the aerial view of the wells showing the bottom-hole pressure match where the color coding is based on the percent mismatch. Some of the wells were not used for model calibration since they did not have reliable injection data. These latter wells are color-coded in grey. Green indicates those wells with pressure mismatch less than *10%*, yellow the wells with mismatch between *10%* and *50%* and red with a mismatch greater than *50%*.

While I am permitted to present the profiles of the bottom-hole pressure and injection rates to validate my scientific analysis, my license agreement does not allow me to disclose actual well names or locations. For the sake of brevity, I only show the bottom-hole pressure and injection rate match for *2* of the *29* wells in Figure 25**.**

Based on the history-match, Table 1 and Table 2 present the minimum, maximum, and average porosity and permeability results respectively for Arbuckle Group and Simpson formations. Average porosity of the Arbuckle Group is approximately *7%* and the average permeability is approximately *10* mD. I observed that a slight lateral permeability anisotropy of *1.25* towards the Northerly direction with respect to the Easterly direction in the Arbuckle Group. I also observed a vertical to lateral permeability anisotropy of *0.01*. Even though these numbers are different than the initially considered in the initial modeling steps, these were the values that best adjusted to the observed water injection.

Figure 26 displays the simulated pressure distribution in the basement formation in January 2005 and January 2016. Figure 27 shows the distribution of corresponding pressure buildup due to wastewater injection measured with respect to the initial pressure before the disposal commenced. These figures clearly indicate pockets of pressure buildup around some of the disposal wells.

We further determined the impact of seismically picked faults in the Arbuckle Group based on the pressure buildup or the lack of it around the disposal wells. I hypothesize that some of the faults may be acting as seals while others as conduits. However, in order to conclusively verify the hypothesis, I will need further investigation. Based on the history-match results, I propose the working hypotheses (refer to Figure 28Error! Reference source not found.**)**:

- The recorded injection pressure in the wells around the faults F1 to F4 were too high. Global and layer-wise adjustments of the history match parameters in the numerical simulation models could not account for such high pressures. The likely explanation for such high pressure could be: 1) incorrect reporting of the pressures; 2) poor storage efficiency of the disposal formation in this area; or 3) these faults are sealing in nature.
- The seismic survey did not extend into the shaded area marked as R1; therefore, it was not possible to identify faults in this region. However, history-match results for several wells in this area indicate the possibility of sealing faults nearby.

Limitations

- Compatibility of injection water and in-situ formation water was not investigated. I assumed full compatibility between injection water and formation water (same thermophysical properties). If fluid incompatibility were to be taken into account, I would expect a higher resistance to flow which would lead to higher pressure buildup due to injection.
- There was no control on the initial fluid distribution in the disposal zone. In this study I assumed it to be an aquifer (completely water saturated). I would expect that a multiphase fluid-distribution model would show capillary trapping or residual trapping. This means more resistance to flow, which would translate into higher pressure buildup.
- We did not account for geomechanical stress and strain changes, which may lead to fault reactivation, different pressure and stress propagation due to injection, among others.
- We did not use well hydraulics modeling. Therefore, the back pressure in the well is not accounted for.

- We did not account for communication between any producing interval and the disposal zones. If there is communication, I expect less pressure increase due to injection.

Conclusions

In an attempt to better understand the occurrence of basement earthquakes, I used well-established reservoir characterization workflows to construct an integrated characterization study of the Arbuckle Group-basement wastewater disposal system. The Arbuckle Group average porosity is approximately *7%*. The corresponding permeability averages about *10* mD, with a lateral permeability anisotropy of *1.25.* The Arbuckle Group vertical to lateral permeability anisotropy, $k_v/k_h \approx 0.01$ approximately *0.01* for the Arbuckle Group.

Dominant parameters affecting history-matching are the porosity as well as the horizontal and vertical permeability of Arbuckle Group, the permeability and the horizontal anisotropy of the overlying Simpson and the underlying basement formations, the formation water density, and the viscosity, and productivity index multipliers of the injection wells. Faults play an important role in fluid movement within Arbuckle and Basement Group formations. I observed pockets of non-uniform and large pressure buildup in these formations.

Given the public sensitivity to seismicity, operators should consider characterizing their disposal reservoirs in a manner similar to their hydrocarbon reservoirs. This study shows the need for both improved data recording and additional data collection. In particular, I recommend that operators wishing to pursue the reservoir characterization analysis used here record their injection data on a daily rather than on a monthly or quarterly averaged basis. Although disposals wells are considered to be an expense, a more quantitative estimation of reservoir properties requires the acquisition of P-wave and dipole sonic logs in addition to the commonly acquired triple-combo logs. Finally, to better quantify flow units with the disposal reservoir, I recommend that operators acquire sufficient core to represent the reservoir heterogeneity.

Acknowledgments

This project was funded as part of the Seismicity Emergency Collaboration project by the State of Oklahoma and coordinated by the Oklahoma Geologic Survey. The authors wish to acknowledge their colleagues in other parts of the larger research project, specifically Dr. Kyle Murray who coordinated our phase of the project fitting into a larger study of groundwater injection throughout Oklahoma. Raster images of the well-log data used in this project were provided by IHS. Wellhead pressures were converted to bottom-hole pressure using commercial software PROSPER. Most of the data interpretation and integration, as well as flow simulation was conducted using Schlumberger software (Petrel, ECLISPE and PIPESIM) provided to the University of Oklahoma for use in research and education. Most importantly, I acknowledge the anonymous oil company operator that wished to further the scientific understanding of the linkage between injection wells and fluid flow near the basement that provided a license to the seismic data volume, initial horizon picks, injection data, and pressure data that were key to conducting this unique research effort.

References

AASPI, 2017, Attribute-Assisted Seismic Processing and Interpretation software documentation: http://mcee.ou.edu/aaspi/documentation.html (Accessed, November 26, 2017).

Anderson, D., and L. Mattar, 2004, Practical diagnostics using production data and flowing pressures: SPE-89939-MS. http://dx.doi.org/10.2118/89939-MS.

British Columbia Oil and Gas Commission, 2012, “Investigation of observed seismicity in the Horn River Basin, at www.bcogc.ca/node/8046/download?documentID=1270. Accessed 31 Jan 2019.

Chopra, S. and K. J. Marfurt, 2007, Seismic attributes for prospect identification and reservoir characterization: SEG Geophysical Developments, **11**, 464p.

Chopra, S., L. Infante-Paez, and K. J. Marfurt, 2018, Intra-basement intrusions in the STACK area of Oklahoma: AAPG Explorer, May Geophysical Corner. https://explorer.aapg.org/story/articleid/46763/intra-basement-intrusions-in-the-stack-area-of-oklahoma) (Accessed January 3, 2019).

Clark, C.E., and J. A. Veil, 2009, Produced Water Volumes and Management Practices in the United States, United States Department of Energy, Argonne National Laboratory ANL/EVS/R-09/1. www.evs.anl.gov/pub//doc/ANL_EVS_R09_produced_water_report_2437.pdf

Elebiju, O. O., S. Matson, G. R. Keller, and K. J. Marfurt, 2011, Integrated geophysical studies of the basement structures, the Mississippi chert, and the Arbuckle Group of Osage County region, Oklahoma: AAPG Bulletin, **95**, 371–393.

EIA, 2019, Petroleum and other liquids for the state of Oklahoma: https://www.eia.gov/dnav/pet/hist/LeafHandler.ashx?f=M&n=PET&s=MCRFPOK1 (Accessed January 3, 2019).

EPA Underground Injection Control National Technical Workgroup, 2014, Minimizing and managing potential impacts of injection- induced seismicity from class II disposal wells: Practical approaches, https://www.slideshare.net/MarcellusDN/epa-report-minimizing-

and-managing-potential-impacts-of-injectioninduced-seismicity-from-class-ii-disposal-wells-practical-approaches.

Evans, D. M., 1966, The Denver area earthquakes and the Rocky Mountain Arsenal disposal well: Mtn. Geologist, v. 3. no. 1, 23-26.

Friberg, P., A. Besana-Ostman and G. M. Dricker, 2014, Characterization of an earthquake sequence triggered by hydraulic fracturing in Harrison County, Ohio: Seismol. Res. Lett. **85**, no. 6, doi: https://doi.org/10.1785/0220140127.

Gogri, M. 2018. Investigation and Real-Time Monitoring for Safe Waste-Water Disposal With a Focus on Arbuckle Group, Oklahoma. MS thesis, University of Oklahoma, Norman, Oklahoma (January 2018).

Holland, A., 2013, Earthquakes triggered by hydraulic fracturing in south-central Oklahoma: Bull. Seismol. Soc. Am. **103**, 1784–1792.

Horton, S., 2012, Disposal of hydrofracking waste fluid by injection into subsurface aquifers triggers earthquake swarm in central Arkansas with potential for damaging earthquake: Seismol. Res. Lett. **83**, 250–260.

Izgec, B., and S. Kabir, 2011, Identification and characterization of high-conductive layers in waterfloods: SPE Reservoir Evaluation & Engineering 14 (1), 113-119, SPE-123930-PA. http://dx.doi.org/10.2118/123930-PA.

Jacobs, T., 2016, Seismic Shifts in Oklahoma Lead to Stricter Regulations: *J Pet Technol* **68** (5), 44–48, SPE-0516-0044-JPT. https://doi.org/10.2118/0516-0044-JPT.

Johnson, K.S., 1991, Geologic overview and economic importance of Late Cambrian and Ordovician rocks in Oklahoma, in Johnson, K. S., ed., Late Cambrian-Ordovician geology of the southern Midcontinent, 1989 Symposium: Oklahoma Geological Survey Circular 92, p.3-14.

Kim, W., 2013, Induced seismicity associated with fluid injection into a deep well in Youngstown, Ohio: J. Geophys. Res. **10**.

Kolawole, F., C. Johnston, J. Chang, K. J. Marfurt, Z. Reches, and B. M. Carpenter, 2018, Characterization of pre-existing structures in the basement of Oklahoma with implications for induced seismicity: GSA Annual Meeting in Indianapolis, Indiana Paper No. 158-6.

Liao, Z., H. Liu, Z. Jiang, K. J. Marfurt, and Z. Reches, 2017, Fault damage zone at subsurface: A case study using 3D seismic attributes and a clay model analog for the Anadarko Basin, Oklahoma: Interpretation, 5, T143-T150.

Matson, S. E., 2013, Mississippi Lime Play: From outcrop to subsurface - The evolution of a play: AAPG Search and Discovery Article #110170. (http://www.searchanddiscovery.com/pdfz/documents/2013/110170matson/ndx_matson.pdf.html?q=%252BtitleStrip%253Amississippi+titleStrip%253Alime+%252ByearSort%253A%255B2011+TO+2018%255D). (Accessed January 3, 2019).

McGarr, A., B. Bekins, N. Burkardt, J. Dewey, P. Earle, W. Ellsworth, S. Hickman, A. Holland, E. Majer, J. Rubinstein and A. Sheehan, 2015, Coping with earthquakes induced by fluid injection: Science 347, no. 6224, 830–831, doi: https://doi.org/10.1126/science.aaa0494

Murray, K. E., 2015, Class II saltwater disposal for 2009-2014 at the annual-, state-, and county-scales by geologic zones of completion, Oklahoma: Oklahoma Geologic Survey Open-File Report OF5-2015.

Oklahoma Corporation Commission, 2017, Oil and gas info, https://apps.occeweb.com/RBDMSWeb_OK/OCCOGOnline.aspx (accessed 10 January 2017).

Pickett, A., 2018, Oil and Gas Reporter, New Play Concept 'Merges' SCOOP and STACK Trends in Red-Hot Central Oklahoma. https://www.aogr.com/magazine/cover-story/new-play-concept-merges-scoop-and-stack-trends-in-red-hot-central-oklahoma. (Accessed January 3, 2019).

Qi, X. and K. J. Marfurt, 2017, Volumetric Aberrancy to Map Subtle Faults and Flexures. Submitted to Interpretation.

Schlumberger Education Services, 1991a, Chapter 8, Determination of saturation, *in*, Log Interpretation Principles/Applications.

Schlumberger Education Services, 1991b, Chapter 10, Permeability and productivity, *in*, Log Interpretation Principles/Applications.

Silin, D. B., R. Holtzman, and T. W. Patzek, 2005, Monitoring waterflood operations: Hall method revisited: SPE-93879-MS, http://dx.doi.org/10.2118/93879-MS

Stringer. C. P., 1958, Subsurface Geology of Western Payne County, Oklahoma: Shale Shaker Digest II v. VI-VIII.

Tulsa World, 2019, Oklahoma earthquakes decrease for 3rd straight year: https://www.apnews.com/216ddc7f8391467c90bd526696beb4f3 (Accessed January 3, 2019).

United States Geological Survey, Do all wastewater disposal wells induce earthquakes?, https://www.usgs.gov/faqs/do-all-wastewater-disposal-wells-induce-earthquakes?qt-news_science_products=0#qt-news_science_products accessed 20 February 2019.

van der Baan, M., and F. J. Calixto, 2017, Human-induced seismicity and large-scale hydrocarbon production in the USA and Canada: Geochem. Geophys. Geosyst., 18, 2467-2485

Walsh, F. R., and M. D. Zoback, 2015, Oklahoma's recent earthquakes and saltwater disposal: American Association for the Advancement of Science, 1, No. 5.

Walters, R., M. Zoback, J. Baker and G. Beroza, 2015, Characterizing and responding to seismic risk associated with earthquakes potentially triggered by saltwater disposal and hydraulic fracturing: Seismol. Res. Lett. **86**, no. 4, doi: https://doi.org/10.1785/0220150048.

Wilson, J. L., R. D. Fritz, and P. L. Medlock, 1991, The Arbuckle Group – Relationship of core and Outcrop Analyses to Cyclic Stratigraphy and Correlation; in Johnson, K. L., Ed., Late Cambrian – Ordovician Geology of the Southern Midcontinent, 1989 Symposium: Oklahoma Geological Survey Circular, **92**, p. 61 – 63.

Zoback, M. D., 2010, Reservoir Geomechanics, Cambridge University Press, 505p.

Figures

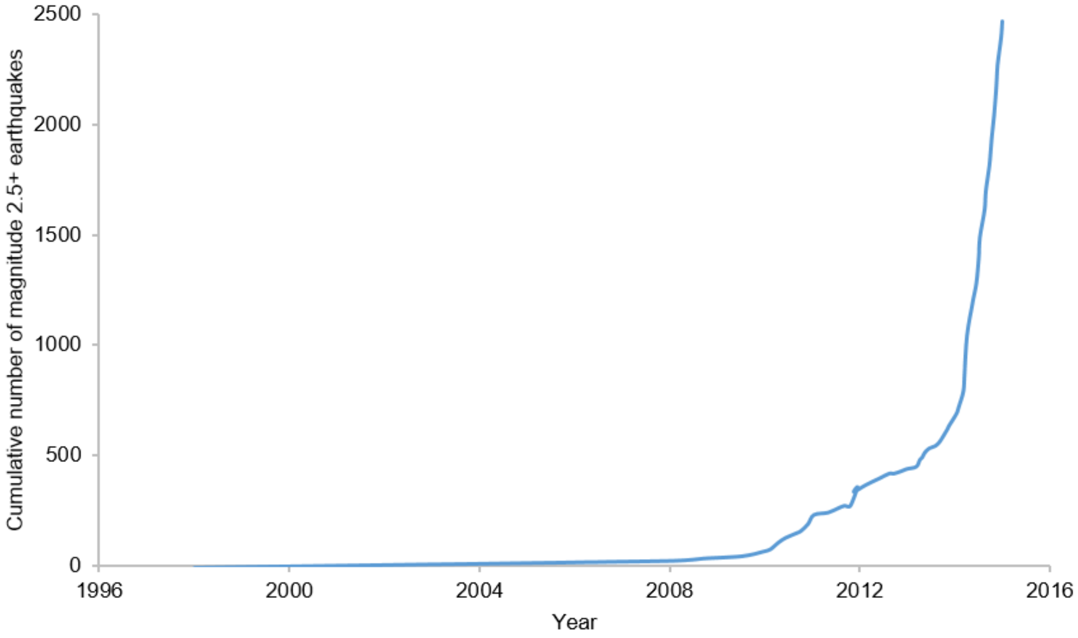

Figure 2. Cumulative number of magnitude 2.5+ earthquakes in Oklahoma (After Walsh and Zoback 2015).

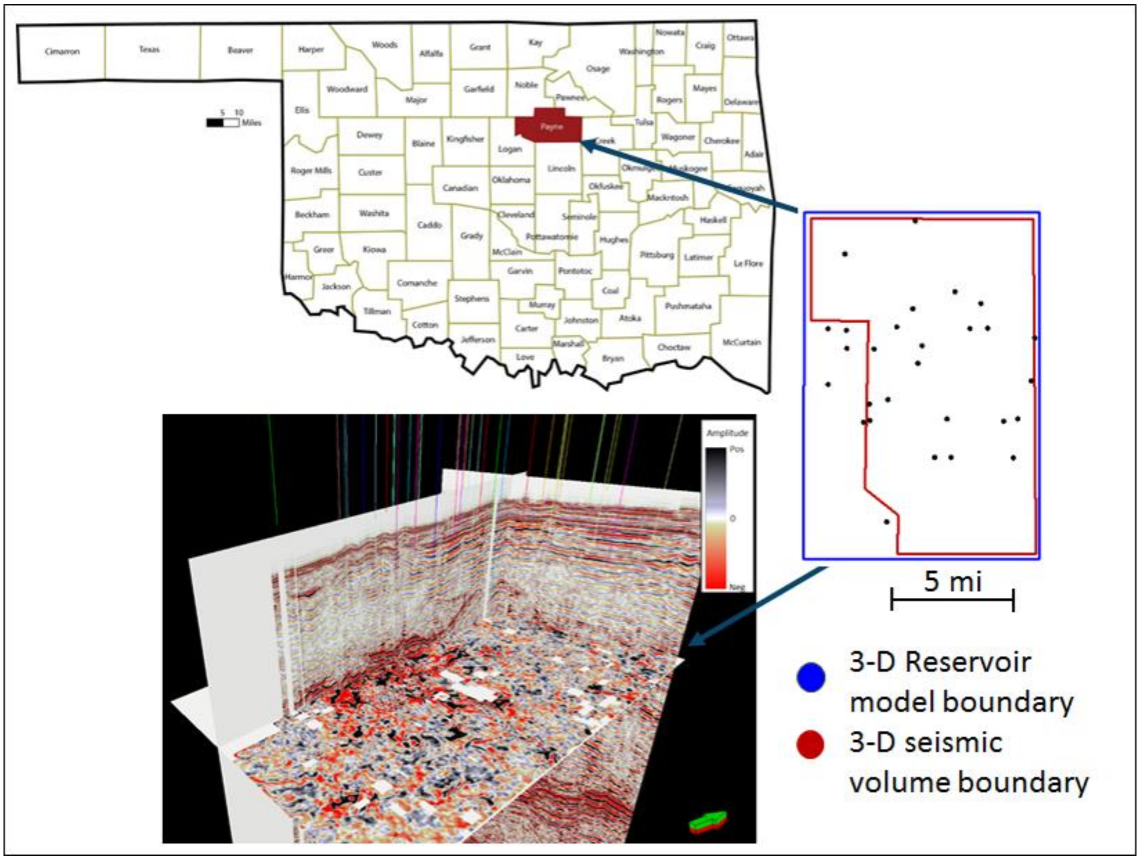

Cimarron
Texas
Beaver
Harper
Woods
Alfalfa
Grant
Kay
Nowata
Craig
Ottawa
Washington
Osage
Woodward
Major
Garfield
Noble
Pawnee
Rogers
Mayes
Delaware
5 10 Miles
Ellis
Dewey
Blaine
Kingfisher
Logan
Payne
Creek
Tulsa
Wagoner
Cherokee
Adair
Roger Mills
Custer
Canadian
Oklahoma
Lincoln
Okfuskee
Okmulgee
Muskogee
Sequoyah
Beckham
Washita
Caddo
Cleveland
Seminole
McIntosh
Haskell
Grady
Pottawatomie
Hughes
Greer
Kiowa
McClain
Pittsburg
Latimer
Le Flore
Harmon
Jackson
Comanche
Garvin
Pontotoc
Coal
Tillman
Stephens
Murray
Johnston
Atoka
Pushmataha
Cotton
Jefferson
Carter
Marshall
Choctaw
McCurtain
Love
Bryan
Amplitude
Pos
0
Neg
5 mi
● 3-D Reservoir model boundary
● 3-D seismic volume boundary

Figure 3. (a) Map showing the location of Payne County, Oklahoma., (b) Boundaries (in crimson) of the 3D seismic survey and (in blue) of the 3D cellular model. Black dots indicate the wells that penetrated the Arbuckle in the study area. (c) A chair display through the seismic amplitude volume. The top of the survey has been cropped 20 ms above the top Arbuckle Formation. The time slice is approximately 800 ms below the top of basement.

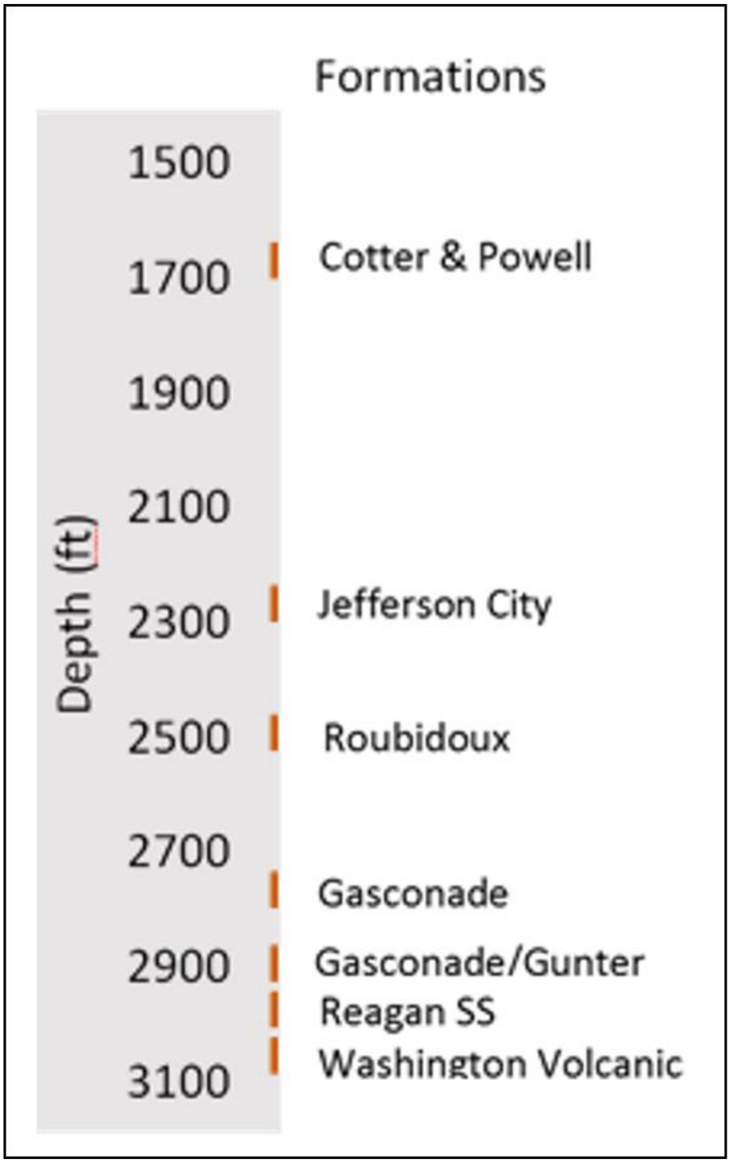

Figure 4. Core from the Catoosa, OK, Amoco Shads #4 Well, with its formations and their respective depths, located in Rogers County (Gogri, 2018).

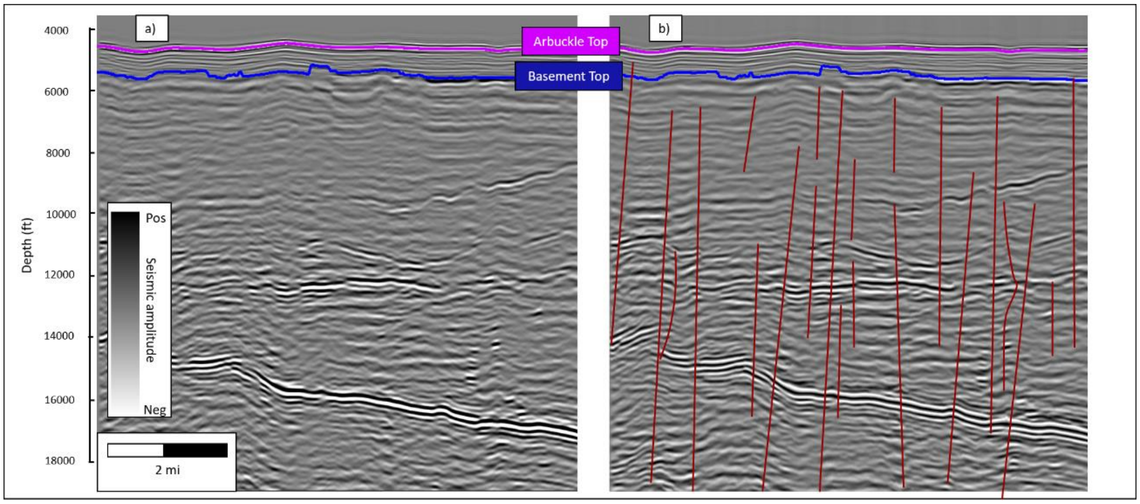

Figure 5. Vertical slice through the 3D seismic amplitude volume (a) before and (b) after structural-oriented-filtering and spectral balancing with a -114° phase shift as guided by the data owner. Red sub vertical lines are example faults interpreted in the basement.

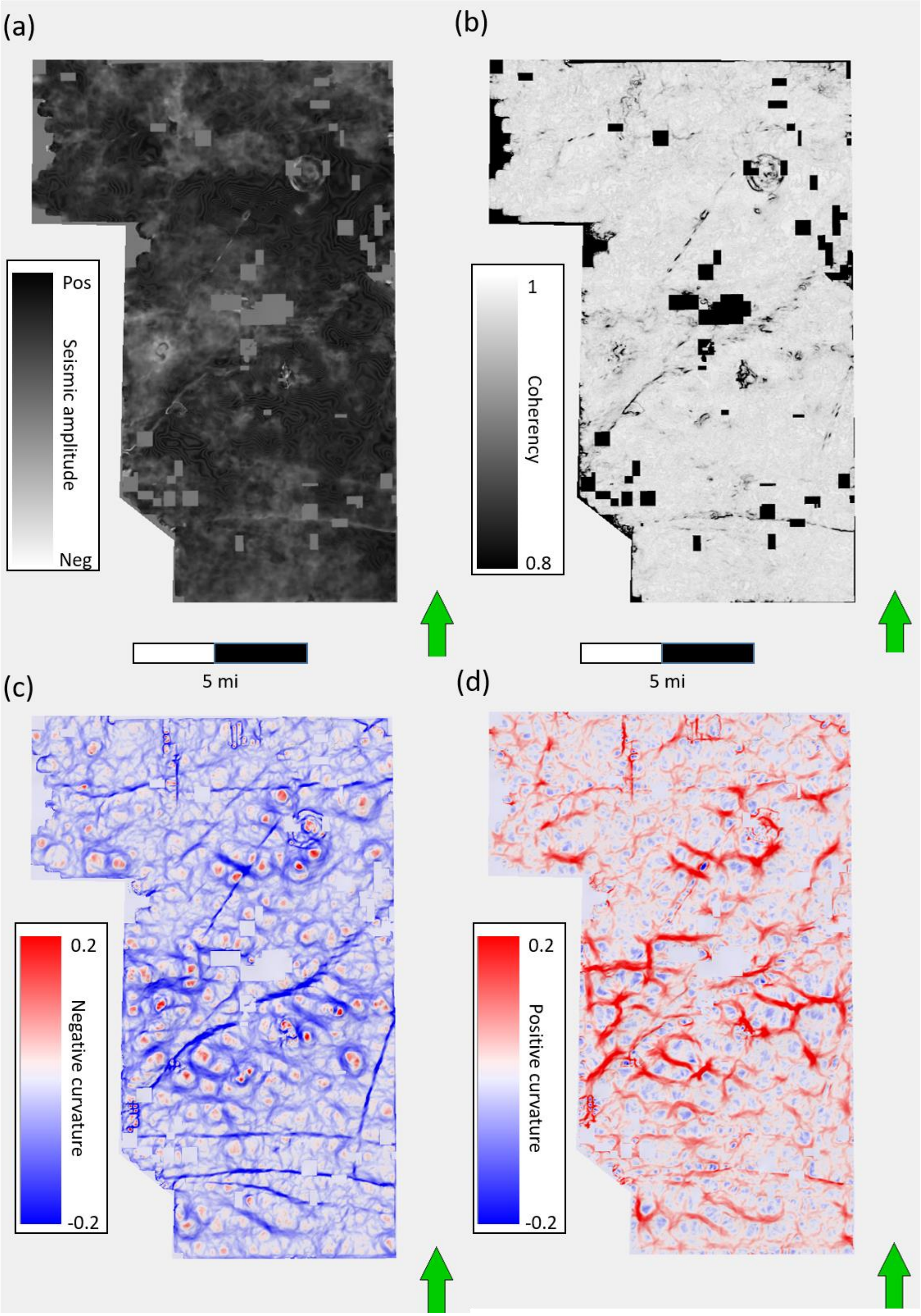
(a)
(b)
Pos
Seismic amplitude
Neg
1
Coherency
0.8
5 mi
5 mi
(c)
(d)
0.2
Negative curvature
-0.2
0.2
Positive curvature
-0.2

Figure 6. Horizon slice of the Arbuckle Group top through (a) seismic amplitude, (b) coherence, (c) negative curvature and (d) positive curvature.

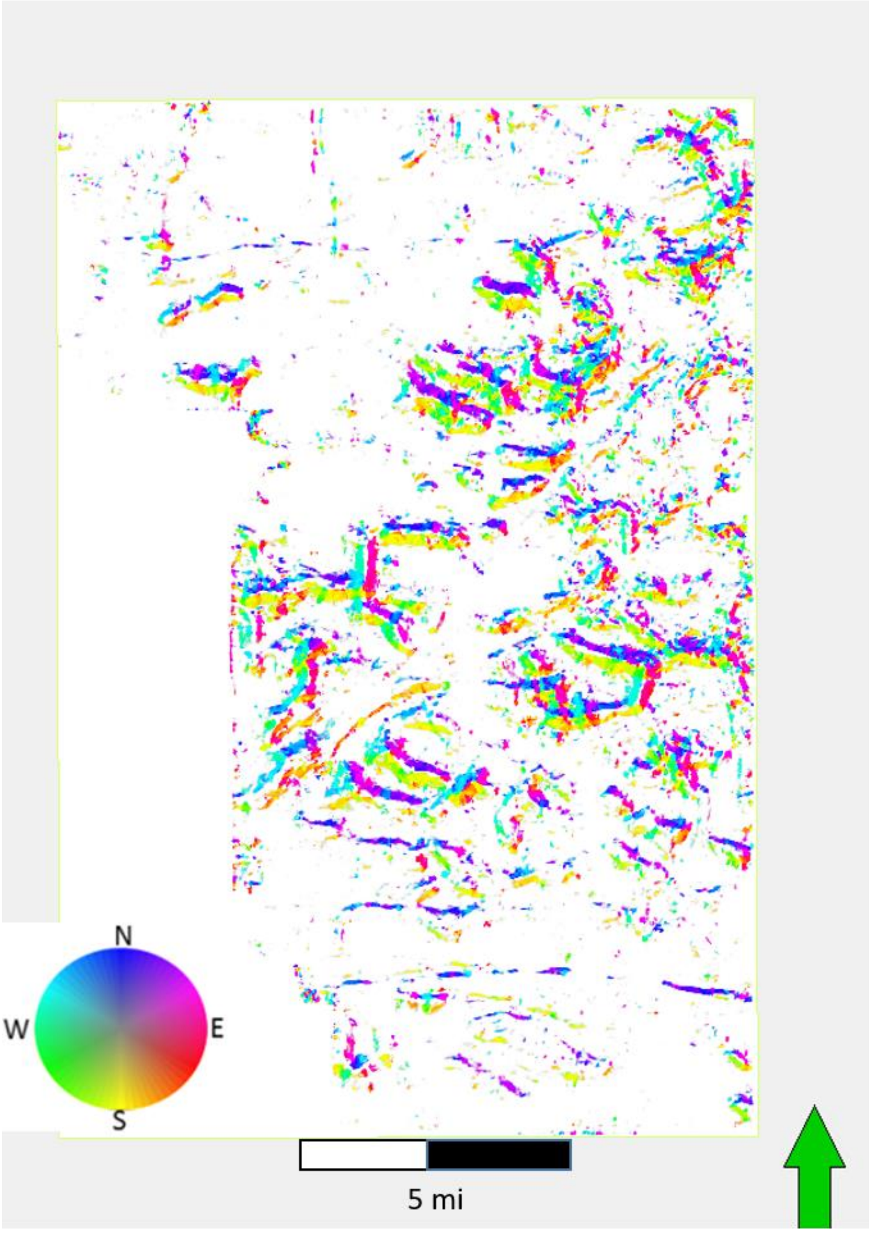

Figure 7. Time slice at the approximate location of the Arbuckle Group top through total aberrancy co-rendered with the azimuth of the aberrancy. An opacity curve is applied such that high aberrancy features appear transparent. Events are colored according to the azimuth in which they are flexing downwards.

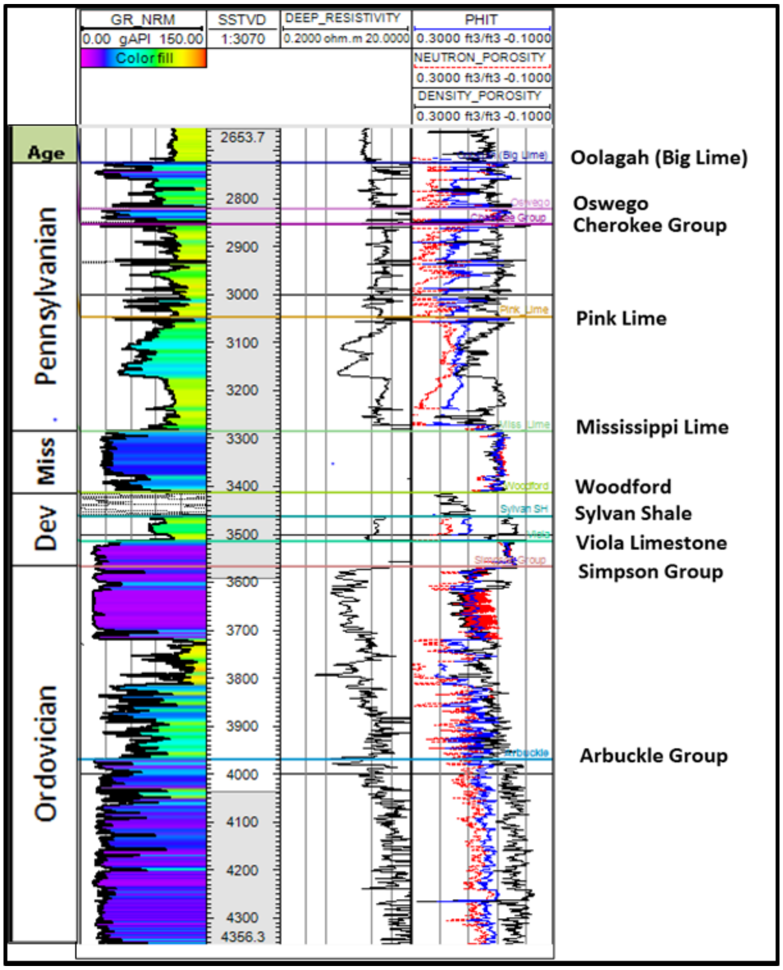

Figure 8. Type log of a gamma ray (to the left) and resistivity and porosity (to the right) showing the major formation tops picked from the Ordovician Arbuckle Group up through the Pennsylvanian Oolagah Limestone showing their ages, as seen on well E. I can see significant contrasts of resistivity and porosity values below the Simpson and Arbuckle Group tops.

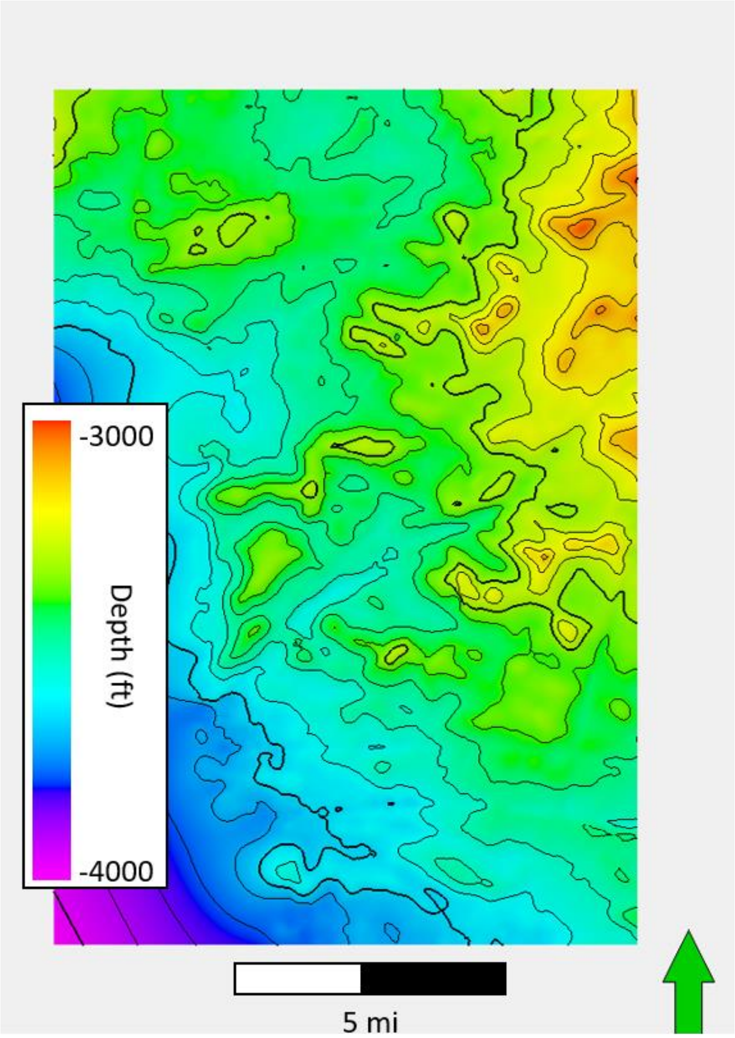
-3000
Depth (ft)
-4000
5 mi

Figure 9. Arbuckle Group structure contour map. The depths increase about 1,000 ft (~300 m) from northeast to southwest.

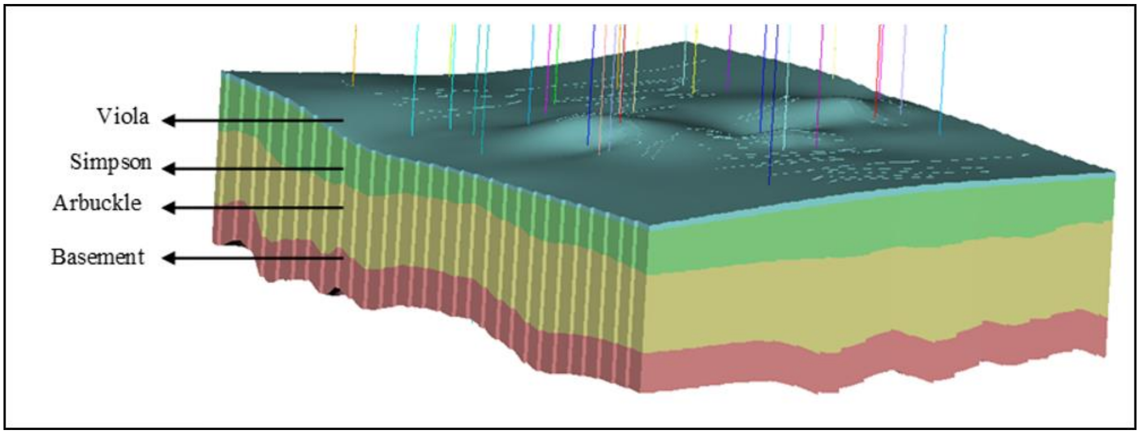
Viola
Simpson
Arbuckle
Basement

Figure 10. Simulation model schematic showing the four major formations. The 3D grid consists of cells with aerial dimensions of 500 ft by 500 ft (152 m by 152 m) and an average layer thickness of 3 ft (0.9 m) resulting in a total of approximately 6.5 million cells.

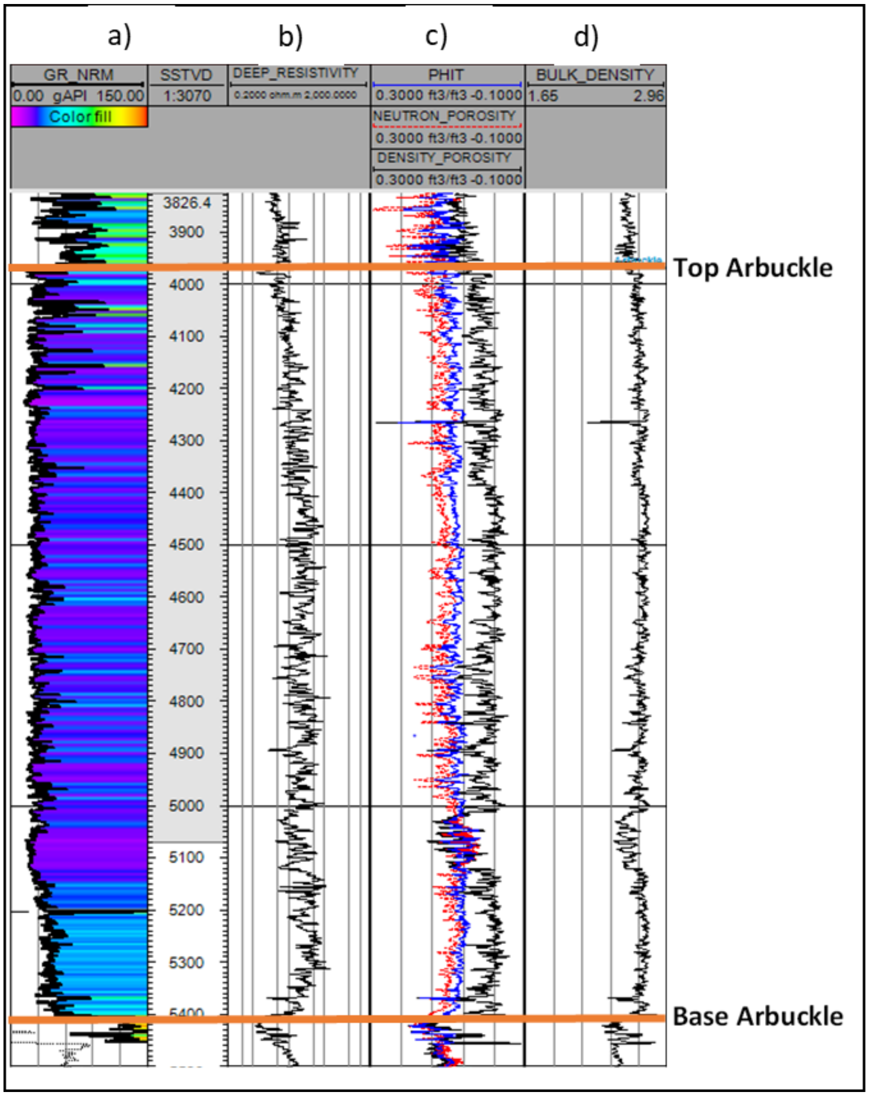

Figure 11. Type log of the Arbuckle group with the following tracks: a) gamma ray curve, b) resistivity, c) porosity, and d) bulk density. This well was located outside of the seismic survey, but within the limits of the reservoir model, as can be seen in **Figure 15**.

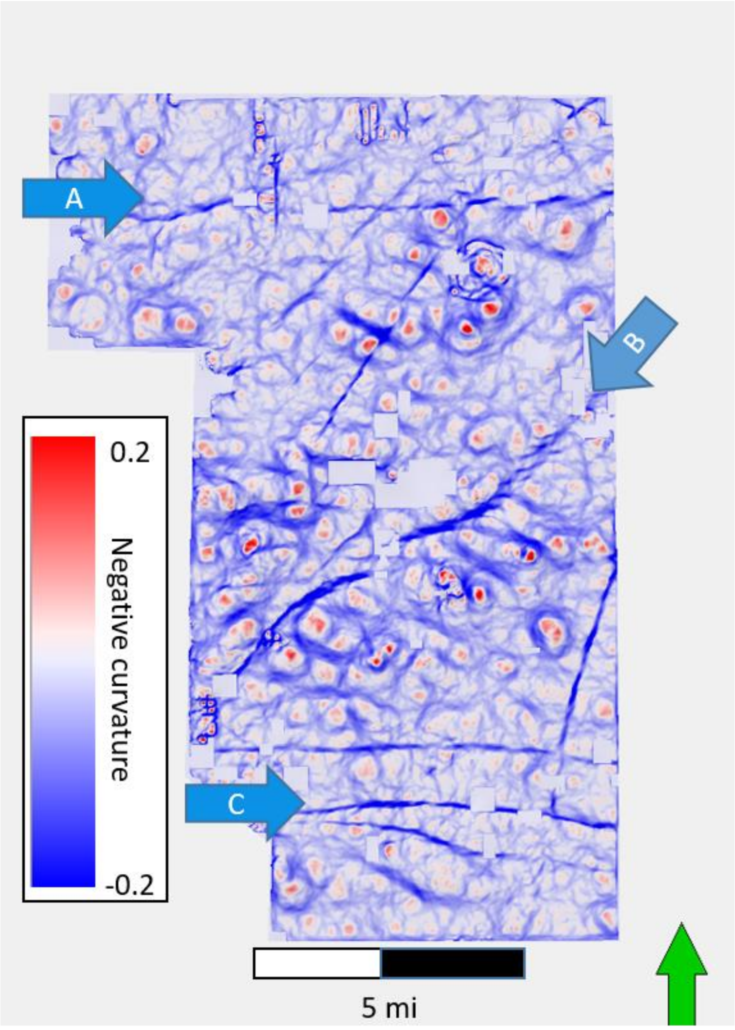

Figure 12. Horizon slice along the top Arbuckle Group through the negative curvature volume showing lineaments corresponding to faults seen on vertical slices through the seismic amplitude volume. Blue arrows indicate three of the larger faults that continue up through the Red Fork formation (personal communication from the data owner).

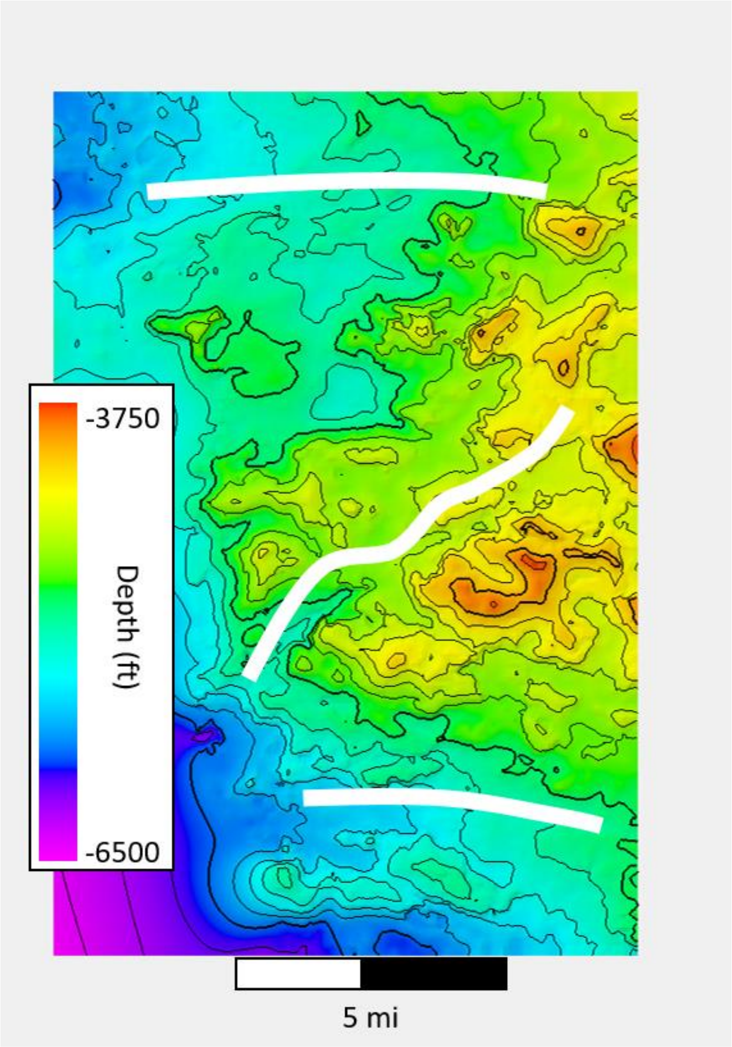
-3750
Depth (ft)
-6500
5 mi

Figure 13. Structure map of basement top. White lines represent location of faults interpreted from curvature attributes.

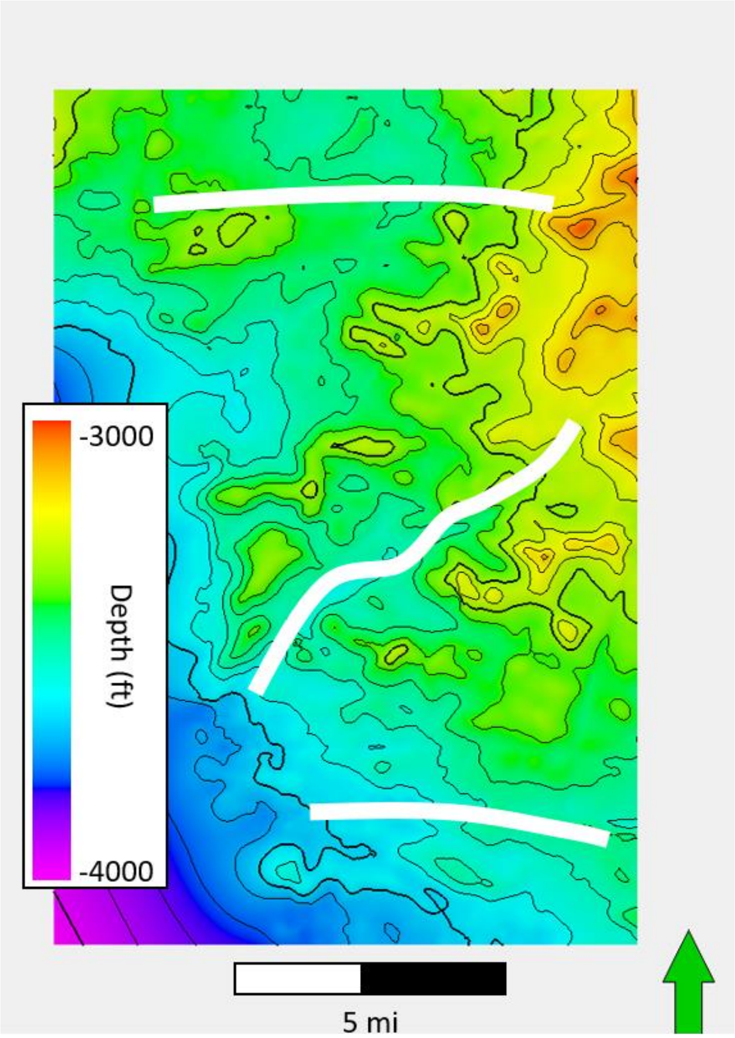
-3000
Depth (ft)
-4000
5 mi

Figure 14. Structure map of Arbuckle Group top. White lines represent location of faults interpreted from curvature attributes.

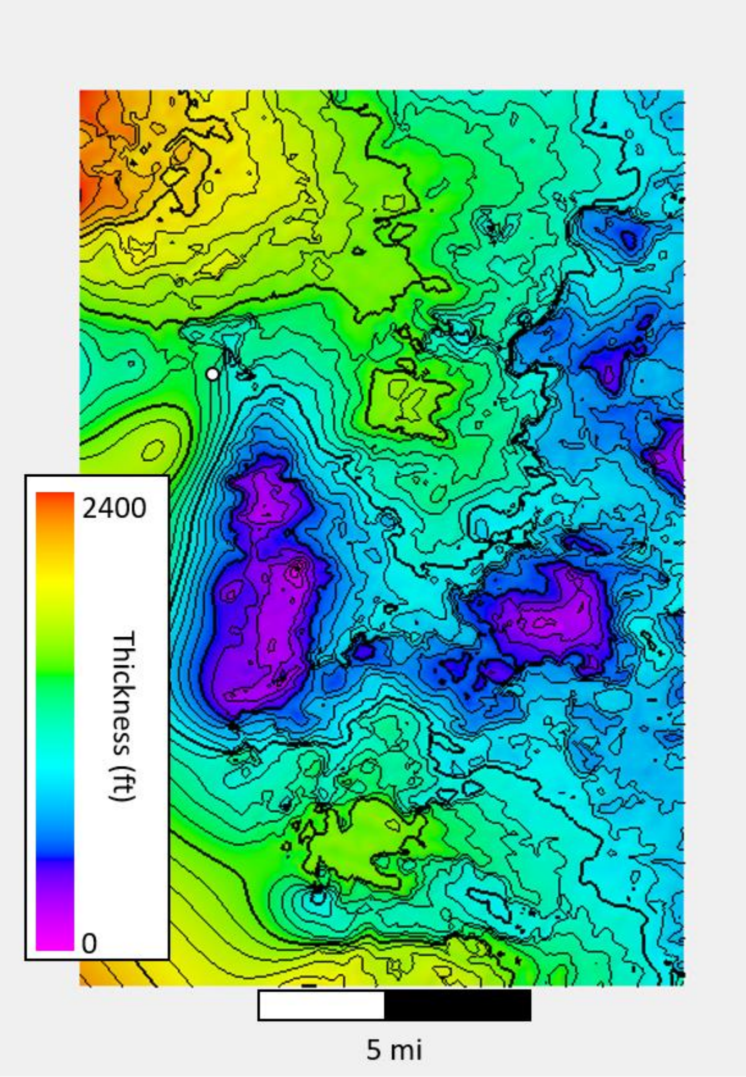

Figure 15. Arbuckle Group Isopach map. The average thickness is approximately 1200 ft. (~380 m) for most of the survey with the unit thickening to the southwest and northwest. White circle represents location of type log shown in **Figure 11**.

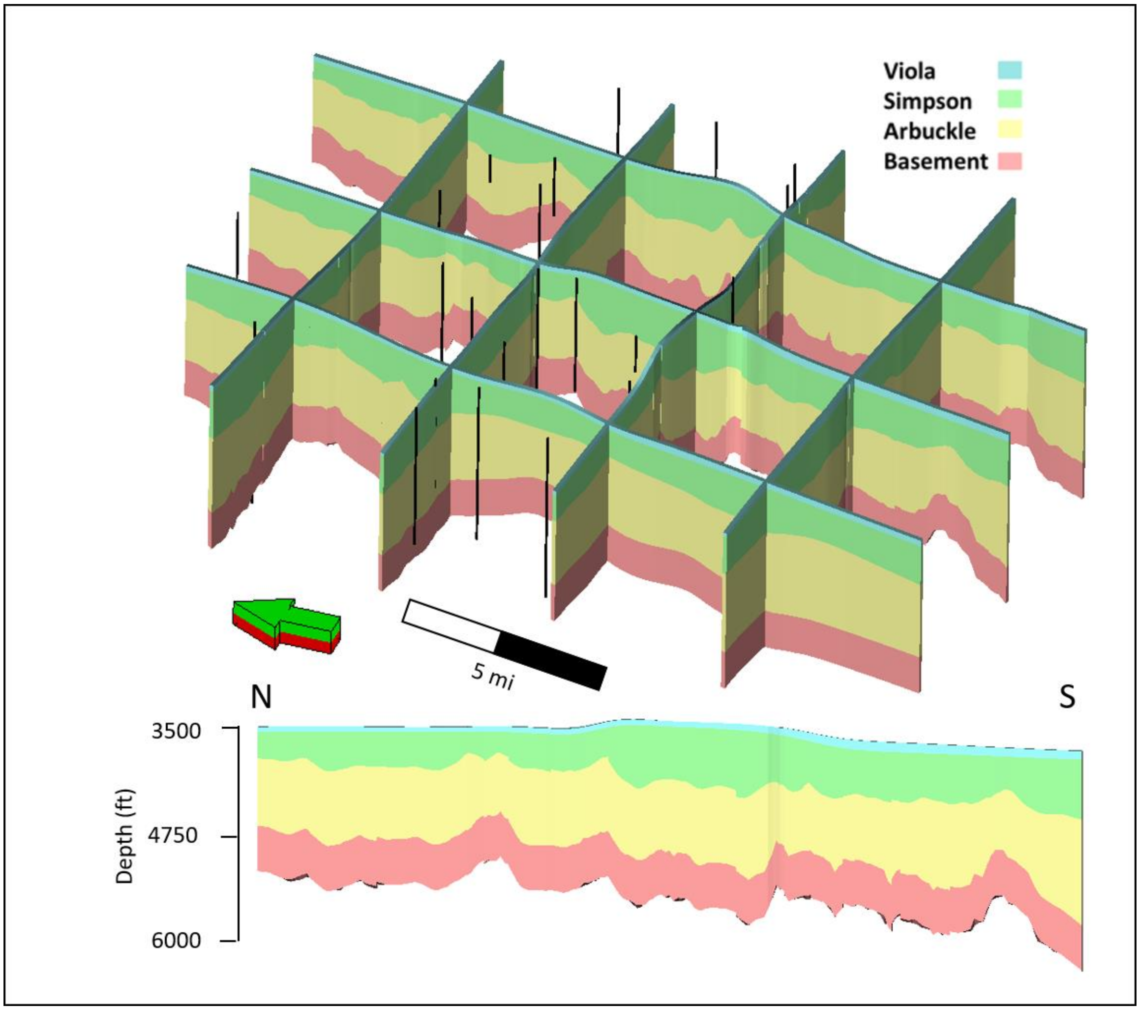
Viola
Simpson
Arbuckle
Basement
5 mi
N
S
3500
4750
6000
Depth (ft)

Figure 16. Stratigraphic framework (3D grid). A proportional layering scheme was used, and the resulting grid contains approximately 6.5 million cells. The 3D grid consists of cells with aerial dimensions of 500 ft. by 500 ft. (152 m by 152 m) and an average layer thickness of 3 ft. (0.9 m).

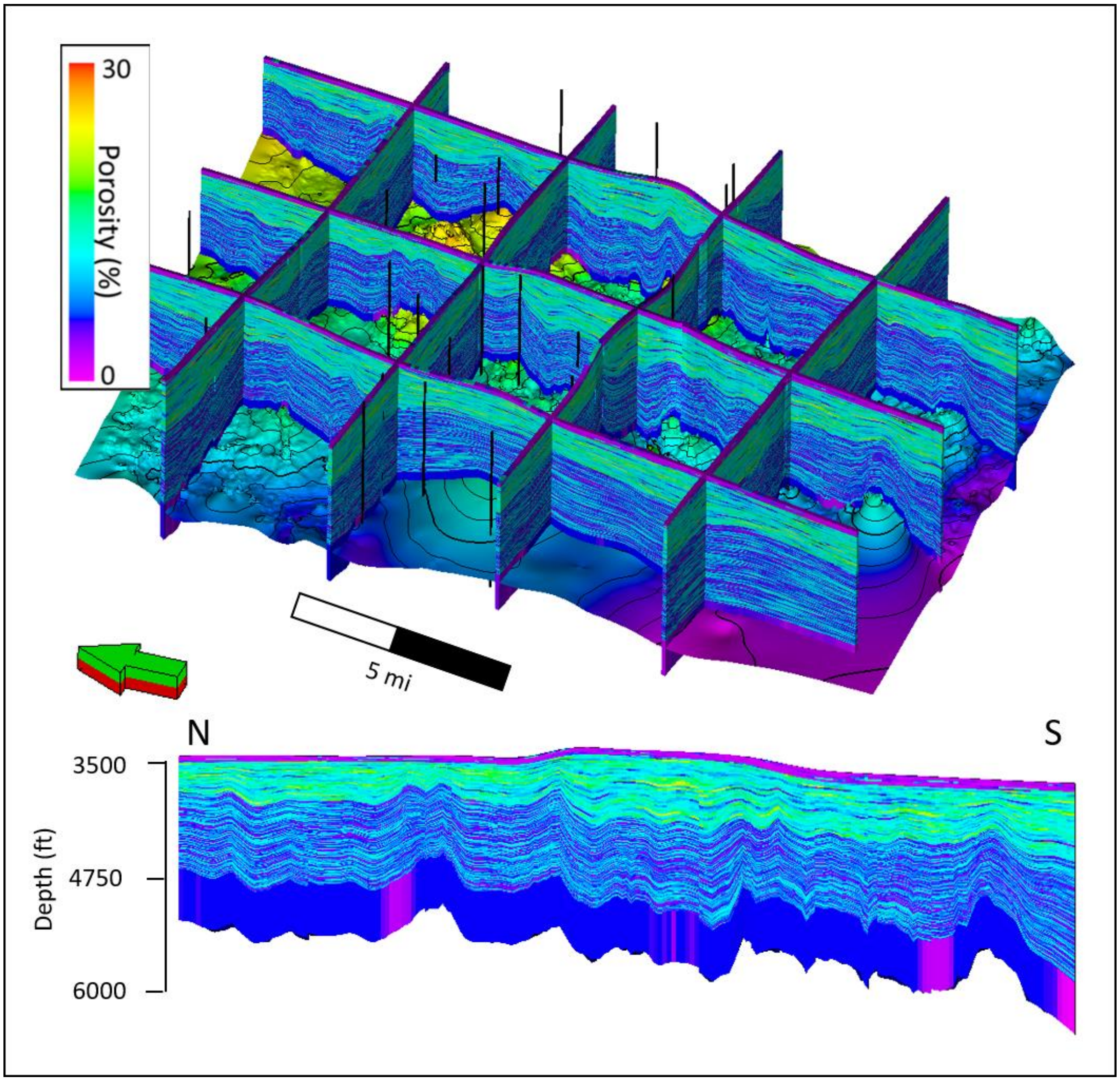
30
Porosity (%)
0
5 mi
N
S
3500
4750
6000
Depth (ft)

Figure 17. Porosity model of the basement through Viola intervals. Vertical exaggeration 10x.

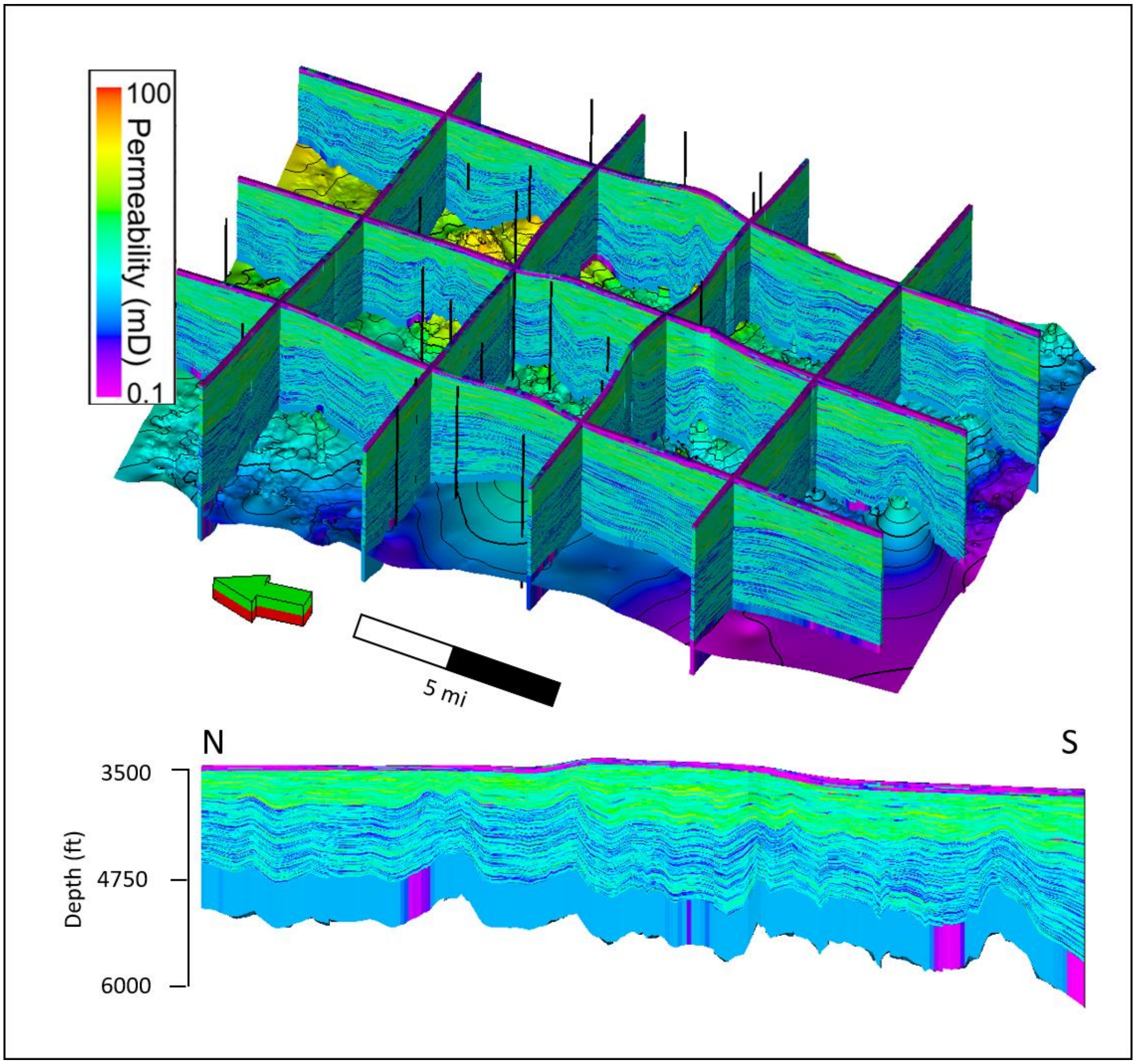
100
Permeability (mD)
0.1
5 mi
N
S
3500
Depth (ft)
4750
6000

Figure 18. Permeability model of the basement through Viola intervals. Permeability values range from 0.1 – 100 mD, with the highest permeability values being associated with faults interpreted from the seismic survey. Vertical exaggeration 10x.

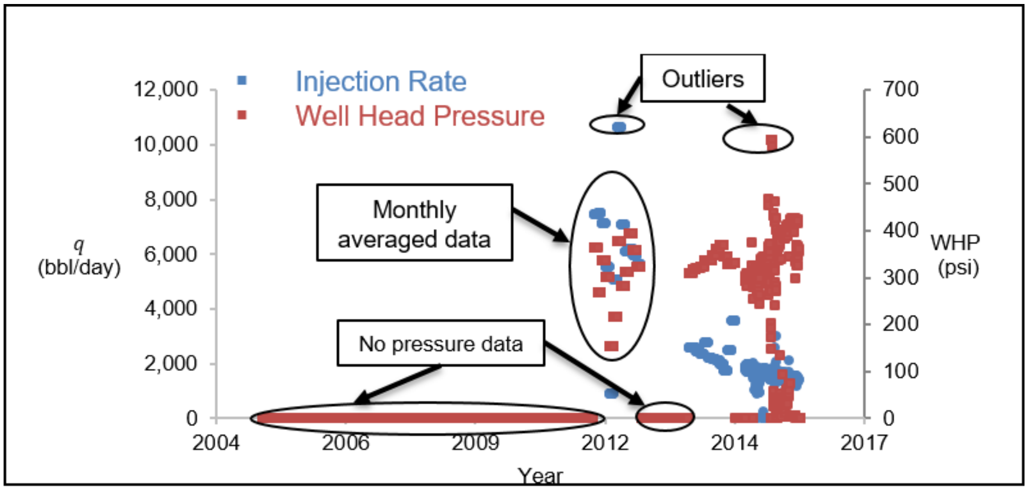

Figure 19. Pressure and injection-rate data for a well highlighting various forms of data quality issues. WHP stands for Well Head Pressure.

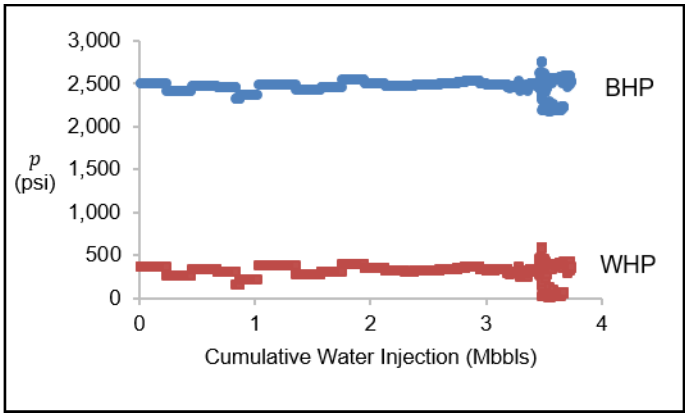

Figure 20. Conversion of wellhead pressure to bottomhole pressure for a well. BHP stands for Bottom Hole pressure.

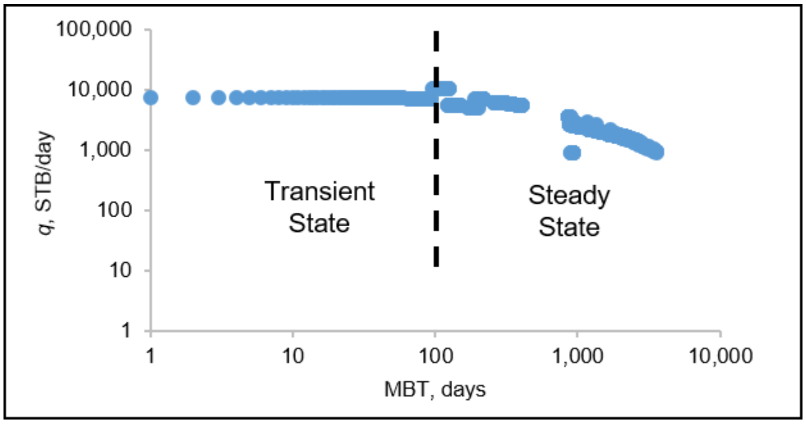

Figure 21. Material-balance-time diagnostics plot of a random well for flow regime identification.

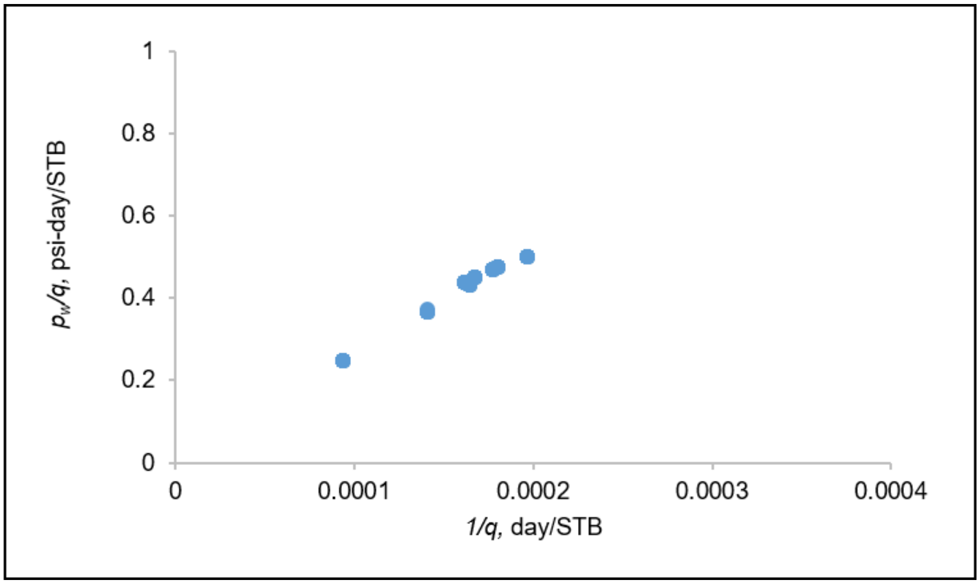

Figure 22. Silin-slope plot.

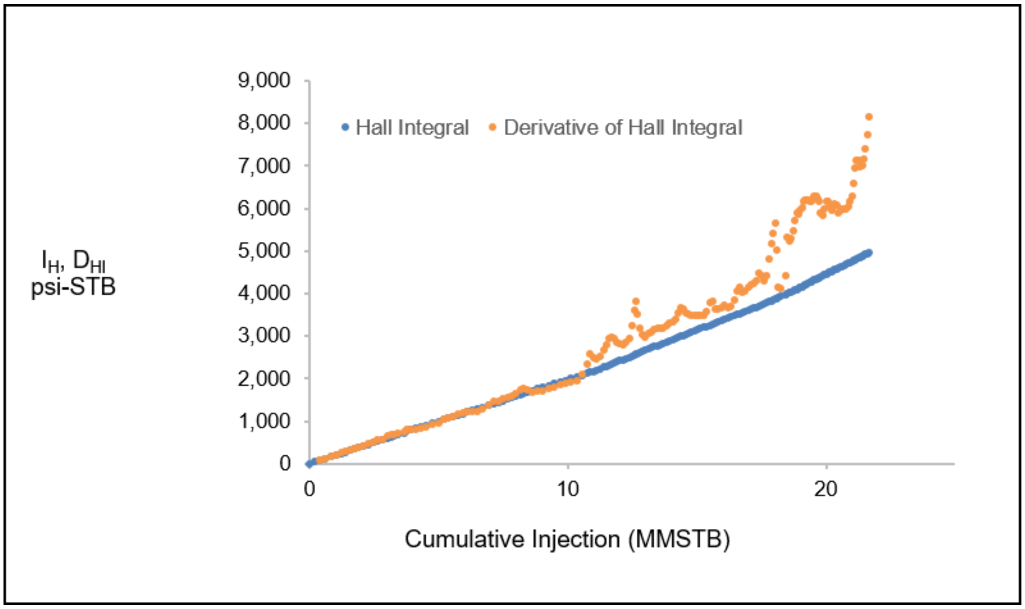

Figure 23. Modified Hall plot analysis of a well.

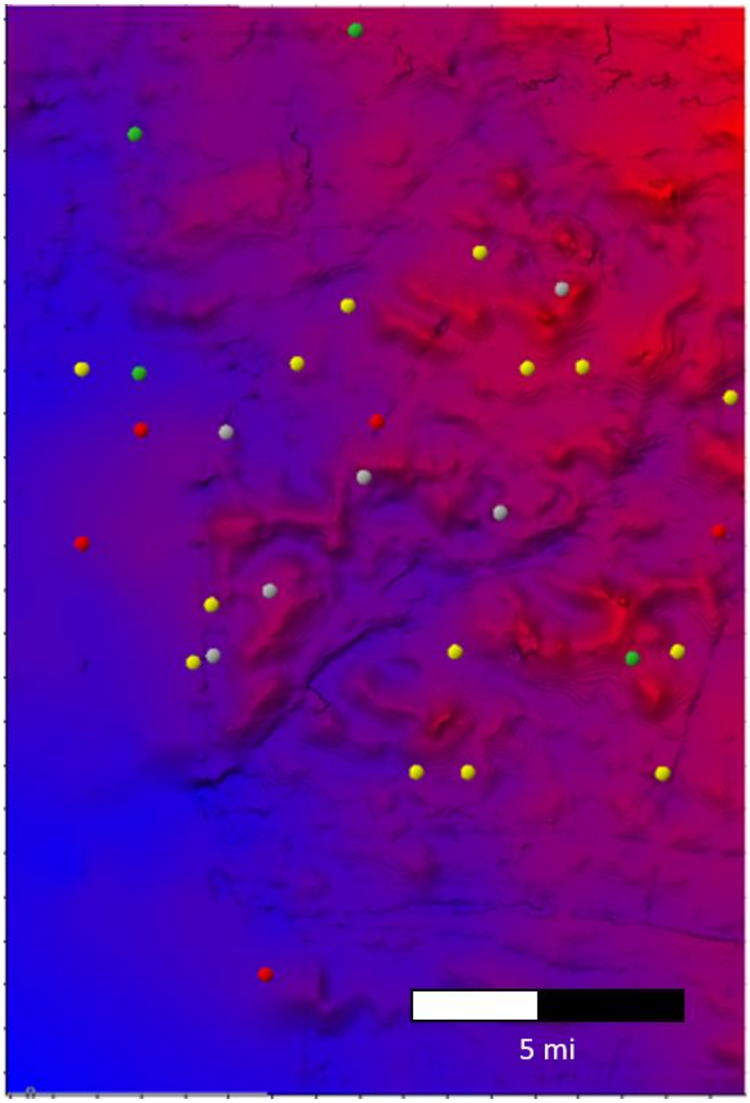

Figure 24. Bottom hole pressure history-match quality. Color coded based on mismatch: Grey – Inconsistent or no data, Green – less than 10%, Yellow – within 10 and 50% and Red – greater than 50%. In the background, I display the elevation of the Arbuckle Group top: blue represents deeper regions while red the shallower regions.

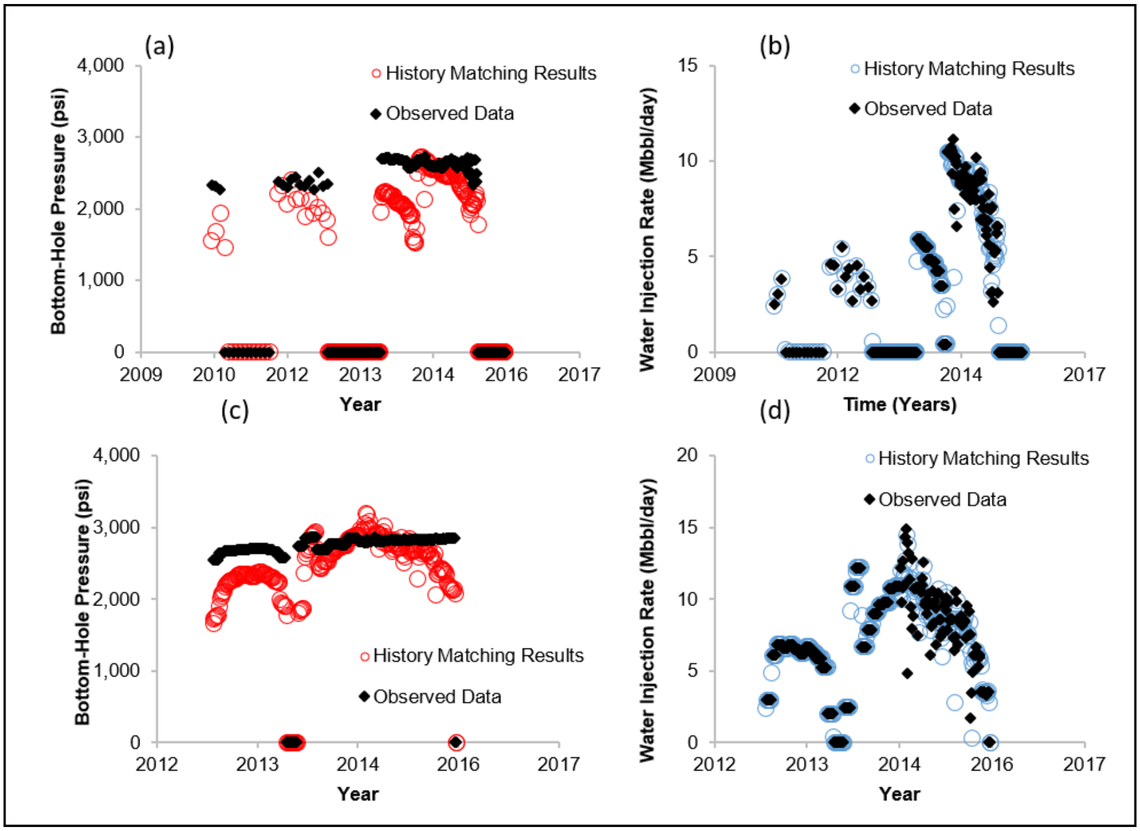

Figure 25. Bottom hole pressure and injection rate match for two wells. (a) Bottom hole pressure for Well 1; (b) Water injection rate for Well 1; (c) Bottom hole pressure for Well 2; and (b) Water injection rate for Well 2.

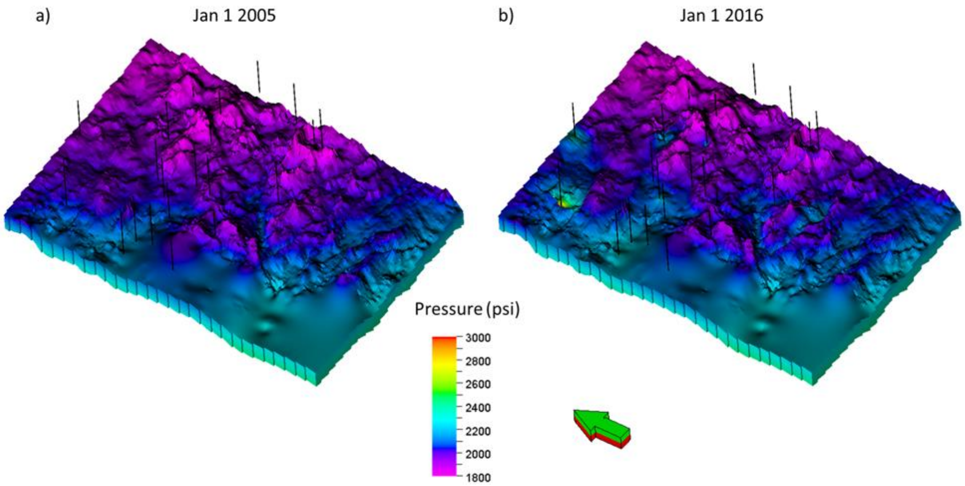
a)
Jan 1 2005
b)
Jan 1 2016
Pressure (psi)
3000
2800
2600
2400
2200
2000
1800

Figure 26. Distribution of pressure in the basement formation at a) the beginning of 2005 and b) the beginning of 2016.

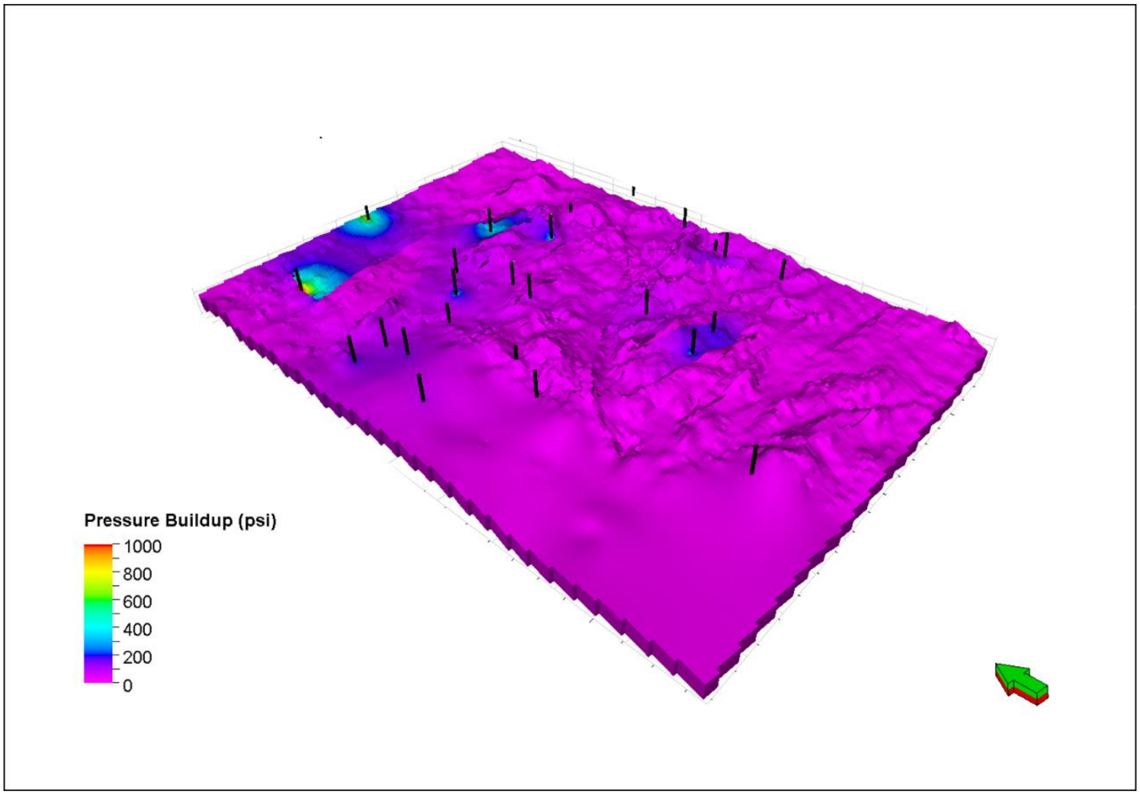
Pressure Buildup (psi)
1000
800
600
400
200
0

Figure 27. Distribution of pressure buildup due to wastewater injection in the basement formation at the beginning of 2016.

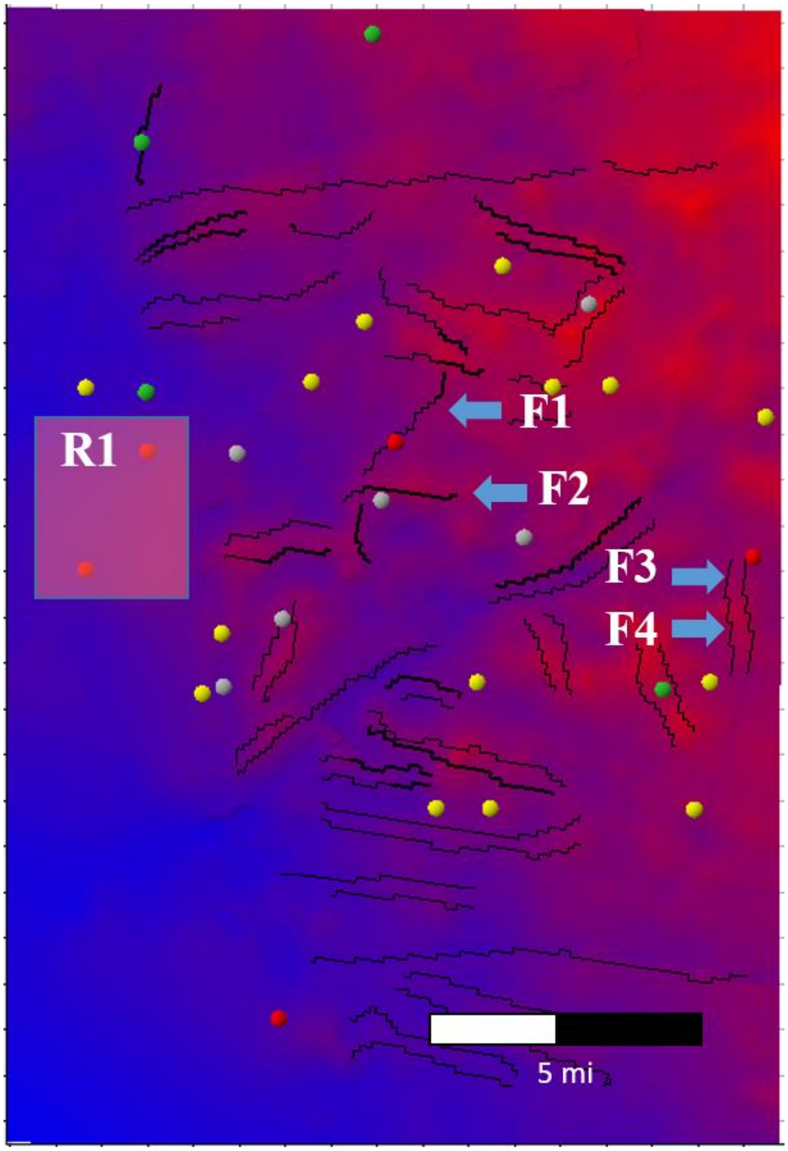

Figure 28. Significance of the interpreted faults based on pressure buildup around the disposal wells. Wells are color coded according to the quality of pressure match as used in **Figure 24**. In the background, I display the elevation of the Arbuckle Group formation top: blue represents deeper regions while red the shallower regions.

Tables

Table 1. Minimum, maximum and average porosity values for Arbuckle and Simpson formations based on history-match.

Formation	Minimum porosity	Maximum porosity	Average porosity
Arbuckle Group	3%	15%	7%
Simpson	2%	22%	12%

Table 2. Minimum, maximum and average permeability values for Arbuckle and Simpson formations based on history match.

Formation	Minimum permeability	Maximum permeability	Average permeability
Arbuckle Group	1 mD	40 mD	10 mD
Simpson	1 mD	130 mD	40 mD

Chapter 3: Mafic sill complexes and interactions in the Precambrian basement of north-central Oklahoma: insights from depth-migrated seismic imaging

Abstract

The composition, distribution and structure of igneous plumbing systems in the basement provide insight into the tectono-thermal and deformational history of the continental crust. Most studies on igneous intrusions are conducted using limited basement outcrops, sparse subsurface geological data and/or time-migrated seismic reflection volumes. These datasets are inadequate in that they either provide only limited extent of the features or they do not adequately image their structural geometries. Here, I depth-migrate a 3-D pre-stack seismic volume in north central Oklahoma where recent studies have highlighted the presence of basement igneous sills (BIS), expressed as intra-basement seismic reflectors (IBR), possibly associated with the Mid-Continent Rift. The depth-migrated data allow me to better delineate the geophysical characteristics of the BIS, and I integrate it with outcrop observations and well log data to constrain my geological interpretations. Further, I create geologically-realistic 2D seismic forward models of the sills to assess the limitations to resolving the BIS stacking patterns observed in wireline logs. I find that (1) depth-migration of the seismic volume provides better imaging of the geometry of the BIS, (2) 2D forward models show that distinct geometries for fault-controlled basement sill steps can be distinguished in seismic reflection data and (3) salient geometric features of the BIS observed in outcrops are consistent to those in the depth-migrated seismic data. My study provides the first results on the application of depth-migrated seismic data to the investigation of basement intrusions, and also provides important insights into the seismic imaging of sill complexes.

Introduction

Igneous sheet intrusions have been studied in various tectonic settings across the globe, including sedimentary basin types and exposed igneous provinces (Stephens et al., 2017; Thomson and Schofield, 2008). Such intrusions are of special interest for understanding the tectonothermal evolution of the continental crust and hazardous magmatic systems in active tectonic basins (Galland, 2012). Also, sedimentary-hosted igneous intrusions pose important implications for the petroleum system of petroliferous sedimentary basins (Senger et al., 2017; Schofield et al., 2015). Igneous sheet intrusions show relatively high acoustic impedance contrast with overlying and underlying sedimentary sequences, thus they are easily recognized in seismic reflection volumes (Eide et al., 2017; Infante and Marfurt, 2017; Magee et al., 2013; Magee et al., 2016). This high reflectivity characteristic also makes them good candidates for forward modeling, for which different authors have studied their interactions with geological structures or other types of rock in terms of amplitude or frequency changes (Eide et al., 2017; Magee et al., 2015).

However, most of the studies that I have analyzed focus their results and interpretation on time-migrated seismic volumes that, while attaining relevant results that further our understanding of igneous intrusions and their interactions with host rocks and structures, may not properly map important components of these features, such as accurate dip and horizontal spatial location of events. Time migration assumes a laterally invariant velocity field that in the presence of a complex overburden may erroneously locate seismic events in space (Yilmaz, 2001; Jones et al., 2014). A carefully processed depth migration can lead to a more accurate location of seismic events of interest within a volume through the utilization of a velocity model that also takes into account lateral velocity changes (Etgen and Kumar, 2012; Yilmaz, 2001).

In this study, I utilize carefully modeled synthetic seismograms based on field observations of granite-hosted mafic sheet intrusions (sills) in the Mill Creek area, southern Oklahoma to study the seismic expression of the geometrical structure of mafic sills hosted in a felsic igneous basement rock. The models are parametrized using realistic velocities and density values from analogue locations in Oklahoma. From these synthetics, I study the seismic attribute response of such intrusions to evaluate if these can be further utilized in my interpretation workflow for a real seismic volume from north-central Oklahoma. I then reprocess and depth-migrate the seismic data volume building a carefully constructed state-of-the-art velocity model to enhance the seismic image of the basement intrusions within the data set.

Although the attribute expression of igneous intrusions has been studied by previous authors (Infante and Marfurt, 2017), understanding the response of synthetic models and what information is recoverable from seismic attributes is the next logical step for studies presented by Eide et al., (2017) and Magee et al. (2015). I take special care of which seismic attributes to select in order to avoid erroneous interpretations (Lubo and Marfurt, 2019). I find that the modeled responses can be recognized in real igneous intrusions in the basement of Oklahoma. I also find that by previously depth-migrating the seismic volume, we can image geological structures not previously revealed by the time-migration.

Geologic setting and data available

Oklahoma's basement is comprised of igneous rocks of the Proterozoic (*1.35 – 1.4* Ga) Southern Granite Rhyolite Terrane of south-Central United States (Thomas et al., 1984; Bickford et al., 2015) Since its emplacement, this basement has experienced repeated episodes of magmatic extensional tectonic events. It has been shown that the *1.1* Ga Mid-Continent Rift, one of the world's largest continental igneous provinces, extends southwards across central Oklahoma (Stein et al., 2014; Stein et al., 2018). In a subsequent Early to Middle Cambrian episode of rift-related igneous activity, thick sequences of granites, rhyolites, gabbros and basalts were emplaced along fault-bounded troughs in southern Oklahoma., (Gilbert, 1983; Keller et al., 2007; Johnson, 2008; Hanson et al., 2012).In the Late Paleozoic, the Cambrian rift and surrounding areas were subjected to compressional stresses related to the Appalachian Orogeny, resulting in the uplifted of the Cambrian rift (Southern Oklahoma Aulacogen, SOA) and reactivation and upward propagation of basement faults in north-central Oklahoma (e.g., Johnson, 2008). Overall, the sedimentary cover of the Anadarko Basin and Arkoma Basin and their associated shelf areas are directly underlain by the Precambrian igneous basement (Johnson, 2008). This basement outcrops in two areas: 1) in a small area (~*7.23* km^2) in the Spavinaw area, Mayes County, NE Oklahoma (Hawes, 1952; Benson, 2014), and 2) in a large area (>*300* km^2) in Mill Creek, Johnston County, southern Oklahoma (e.g., Lidiak et al., 2014; Kolawole et al., 2019). The exposures of this granitic basement in the Mill Creek area reveal pervasive intrusions of diabase sills and dikes, and sub-vertical and horizontal fracture networks (Denison, 1995; Lidiak et al., 2014; Kolawole et al., 2019). The seismic reflection data used in this present study is located within the Spavinaw Granite of NE Oklahoma, at ~*170* km west of the surface exposures of the rocks (Figure 29). The Spavinaw Granite is a reddish medium-grained micrographic granite porphyry, primarily composed of reddish plagioclase, perthite, and quartz (Denison, 1981), and black, opaque magnetite accessory minerals (Merritt, 1960). The U-Pb dating of the granite indicates *1,370 +/- 20* Ma age (Bickford and Lewis, 1979). I note that within the limited exposure of the Spavinaw Granite, no mafic sheet intrusions have been observed. However, excellent exposures of mafic sills in granitic basement of similar age and tectonic history as the Spavinaw Granite in southern Oklahoma provides me the opportunity to observe the geometrical character of the sills and incorporate into my geophysical models.

The wide-azimuth seismic survey for this study is located in Payne County, Oklahoma (Figure 29) covering approximately *170* mi^2 with a bin size of *82.5 x 82.5* ft. The sampling interval is *2* ms, a recording time of 6 s, resulting in a volume including *785* inlines and *1166* crosslines. Because of active development of shallower hydrocarbon objectives, our data licensing agreement limits the display of seismic data to the data falling below the top of the Arbuckle Group.

Based on maps from Shah and Keller (2017), my study area falls within the southern granite-rhyolite province, specifically within the Spavinaw granite sills region (Figure 29). The Spavinaw granite is characterized as a deep-red, fine-to-medium-grained granite porphyry, with primary minerals being reddish plagioclase, perthite and quartz (Benson, 2014; and Denison, 1981).

Outcrop images from southern Oklahoma were used in this project to create geometric models that would later be used for the creation of synthetic seismograms (Figure 29c and Figure 29d). Figure 29c displays the interaction of sills with pre-existing fractures that I aim to replicate, while Figure 29d shows the image of sills when no previous fault or fracture system is in place. For the rock properties to model, I used the results presented by Kibikas et al., (2019), summarized in Figure 32.

Given a recording time of *6* s and a basement velocity averaging *20,000* ft/s, our resulting time-migrated, depth converted and depth-migrated volumes image approximately *30,000* ft of subsurface seismic reflections. From wireline logs from the STACK play in Kingfisher county

(Kolawole et al., 2019), I interpret strong reflectors within the basement portion of the survey (Figure 30) to be mafic diabase/gabbro intrusions of Precambrian age within the felsic granite basement. These intrusions are a consequence of the magmatism that created the Mid-Continent Rift System in this part of Oklahoma (Chopra et al., 2018; Kolawole et al., 2019).

Methodology

Prestack time vs prestack depth migration

In contrast to simple stacking, prestack seismic migration is a process that aims to construct an image from recorded seismic data by repositioning data into their true geologic position in the subsurface (Jones et al., 2008). Given an accurate velocity model, migration moves dipping reflections to their true position and collapses diffractions, thereby increasing spatial resolution and yielding a more accurate seismic image of the subsurface. Although there are different migration algorithms, Kirchhoff migration is the most commonly used for land surveys. Kirchhoff migration is based on traveltime tables computed from the surface. As such, it not only images steep dips and accounts for lateral and vertical velocity variations, but also can be directly applied to irregular topography and irregular shot and receiver acquisition geometries.

Because one of the goals of this paper is to compare a depth-migrated seismic volume with a time-migrated depth-converted volume, I focus on the practical difference between both algorithms. The main difference between prestack time migration (PSTM) and prestack depth migration (PSDM) is in how the background velocity model is necessary to compute the traveltimes used for the location of events. In PSTM, each event is located using local one-dimension *v(t)* velocity model. For non-zero-offset events the traveltime tables are created without any information about lateral variations in the velocity field, which can lead to spatial mislocation.

In contrast, for depth migration, traveltime maps are created by shooting rays, extrapolating wavefronts, or using other methods, from the surface into a 3D velocity model, thereby honoring Snell's Law in areas of lateral velocity variation. If the velocity model is accurate, depth-migrated volumes, while computationally more expensive, provide more accurate dip and spatial location of seismic events (Etgen and Kumar, 2012).

Processing Workflow

Figure 31 summarizes my reprocessing effort for the seismic volume shown in Figure 30, beginning with geometrical corrections related to the acquisition parameters, followed by Surface Consistent Spiking Deconvolution (SCSD) provides a compressed, zero-lag wavelet, attenuates reverberations, and increases temporal resolution. Next, I iteratively constructed my velocity model using of Constant Velocity Stacks (CVS) followed by residual statics to correct for near-surface heterogeneities. This process was repeated until residual statics fell consistently below a threshold of *2* ms. With this velocity model I convert my stacking velocities to interval velocities and use a Kirchhoff algorithm to Pre-Stack Depth Migrate (PSDM) the data. I provided residual moveout errors to a tomographic velocity analysis algorithm, providing the next iteration of the velocity model. This process of migration followed by tomography was iterated until improvements in the resulting depth migrated volume were sufficiently small to no longer justify the computational effort of repeating the process. Tomography was computed for two successive depth migration iteration, where residual migration velocity analysis was calculated to fine-tune the background velocity models.

How thin is thin in the basement?

Following Eide et al. (2017), I generate a synthetic wedge model to evaluate the limits of seismic resolution for the diabase intrusions within the granite basement in my seismic data set (Figure 32). Figure 32a shows the geometry modeled for mafic diabase intrusions in a felsic granite host rock. The wedge thins from the right (*h*=1200 ft) towards the left (*h*= 0 ft).

I convolve the reflectivity model generated from Figure 32a with a *20* Hz and a *50* Hz Ricker wavelet to generate the synthetic seismograms displayed in Figure 32b and Figure 32c. I choose these two frequency values is to represent an ideal, higher resolution (*50* Hz) and a more realistic resolution lower resolution (*20* Hz) scenarios. Since I am not modeling seismic noise in my synthetic seismograms, I choose a peak frequency that resembles the frequency range I recover from the basement depth in my seismic data set, thereby allowing me to estimate a resolution limit that more closely resembles the Payne County seismic data volume.

Figure 32d and Figure 32e display the amplitude vs thickness plot for Figure 32b and Figure 32c respectively. Blue arrows indicate the onset of interference patterns, which peak at about *160* ft and *400* ft for Figure 32b and Figure 32c, respectively. Based on the rock parameters displayed in Figure 32a, the one-quarter-wavelength tuning thickness is approximately *100* ft and *250* ft for seismograms in Figure 32b and Figure 32c, respectively. This is our modeled resolution limit for the intrusions in the area. The practical resolution limit will be higher due to a plethora of other seismic artifacts that can contaminate the data. The difference can be explained from the fact that the Ricker wavelet used for convolving with the reflectivity model does not only include *50* or *20* Hz, but also a range of frequencies below and above such values, which will also interact with the reflectivity series.

We make three important observations from the wedge modeling in Figure 32. First, because I did not include noise in my synthetics, they provide an upper limit to the resolution that I can anticipate in the real data. Different forms of seismic noise, such as intrabed multiples, diffractions from faults, and amplitude variation with offset effects, are not included in the simple convolutional model and can alter the seismic image, Second, utilizing amplitude as a proxy for thickness estimation is limited due to the non-unique character of amplitude responses across the spectrum of thicknesses considered in the model. For example, in Figure 32e, an intrusion with a thickness of h = 280 ft has the same seismic amplitude than an intrusion with a thickness h = 600 ft. Therefore, a seismic amplitude of *0.10* can be associated to either a *600* ft or a *280* ft thick intrusion. Third, while the wedge models provide the backbone for seismic resolution within my seismic volume, it does not to say that intrusions below these thresholds cannot be detected. Different studies (Sheriff and Geldart, 1995; and Eide et al., 2017) have shown that detectability well below $\lambda/20$ or $\lambda/30$ is possible depending on the acoustic impedance contrast between the interacting layers. In my current study, given the acoustic impedance contrast between granite and diabase, I would expect to detect layers below the resolution limit, although in the absence of well control I cannot reliably estimate their thickness from seismic data.

Outcrop-based models

Sheet intrusion analysis is important as they allow for inference of regional stress regimes or of layering anisotropic interactions (Baer et al., 1994; Stephens et al., 2017). Based on field observations in South Oklahoma, I built three geometric models of sill emplacement in the presence or absence of pre-existing vertical faults. Such models are displayed in Figure 33. I propose a similar sill emplacement process as the one described by Stephens et al. (2017), although the host rock in my case is igneous granite. I create synthetic seismograms by convolving synthetic Ricker wavelets with the reflectivity models derived from the proposed geometric models. Rock properties for the creation of synthetic seismograms are extracted from Kibikas, (2019) (Figure 32).

In the presence of pre-existing vertical fractures, Figure 33a and Figure 33b show the first stage of intrusion into shallow fractures with magma segments adjacent to steep discontinuities. The proposed geometric model for seismogram construction is displayed in Figure 33c. I will refer to this model as the "faulted" model for the rest of this manuscript, based on the displayed geometry. Figure 33d and Figure 33e show a later stage of the intruding process, where the initial sills inflate until linking occurs due to stepping or breaching of relay structures. Figure 33f shows the proposed geometric model for the synthetic seismogram construction. I will refer to this model as the "inflated" model, based on the underlying physical process I intend to demonstrate. Finally, if no pre-existing fault is present, the sills will continue to expand laterally until eventually merging or remain separate if there is no fracture set connecting both segments (Figure 33g and Figure 33h). The corresponding geometric model is displayed in Figure 33i. I will refer to this model as the "overlap" model.

Even though the processes described before will affect the thickness of the resulting intrusion, I am not considering thickness changes in my geometric models and successive synthetic seismograms, since subtle changes in intrusion thickness will most likely not be resolvable in the seismic data (Figure 32). I do consider changes in the vertical step of the pre-existing fault with regards to the intrusion thickness, since such geometric differences may exhibit different seismic responses through attributes.

Seismic attributes

The SEG Wiki (http://wiki.seg.org/wiki/Seismic_atributes) defines a seismic attribute as a "quantity extracted or derived from seismic data that can be analyzed in order to enhance information that might be more subtle in a traditional seismic image, leading to a better geological or geophysical interpretation of the data". Seismic attributes are routinely used for revealing information from seismic data that is not evident for the naked eye. I computed a suite of seismic attributes for the synthetic seismograms described in Figure 33 to better understand the igneous sills response to wavelet interactions, and improve interpretation workflows for such intrusions.

Coherence is a seismic attribute commonly used for mapping discontinuities in seismic data. Coherence attributes fall within two broad categories: those that are sensitive only to changes in waveform, and those that are sensitive to changes in waveform and amplitude (Marfurt, 2018). For my current implementation, I compute energy-ratio similarity (Chopra and Marfurt, 2007) on synthetic seismograms to evaluate its sensitivity to the presence of pre-existing vertical fault in the image of the igneous intrusions.

"In 2D, curvature (*k*) is defined as the inverse of the radius of the circle that is not only tangent to the surface but that also fits the surface" (Marfurt, 2018). It is an attribute that measures how curved a reflector is within a seismic volume. Following Marfurt (2018) I define curvature to be positive if it defines convex up, and negative a concave down surfaces. I computed curvature attributes for the synthetic seismograms to evaluate if the deformation associated to mafic intrusions can be a distinguishable characteristic of such igneous sills.

Attributes that separate and classify seismic events within each trace based on their frequency content are called spectral decomposition attributes (SEG Wiki, http://wiki.seg.org/wiki/Seismic_atributes). Through spectral decomposition, I computed the peak magnitude (the tuning frequency for Widess' (1973) wedge model) of the spectrally balanced synthetic seismograms to evaluate how interference patterns may be created from the specific geometries I am modeling. Such interference patterns may then be used to infer thickness variations or the presence of discontinuities in the seismic data. The results of the application of these attributes are displayed later in this manuscript.

Results

Time versus depth migration

Seismic migration is a process that aims to properly locate events in subsurface. **Figure 34** and Figure **35** provide a visual comparison of both migration methods presented. **Figure 34**a is a representative cross section through seismic amplitude of the time-migrated, depth converted volume. Two red squares are drawn to focus on two distinct sets of intrusions and how they vary with each migration method. **Figure 34**b shows a fault interpretation performed on the volume. Dotted lines represent interpreted faults with less confidence. I map the intrusion zoomed-in on **Figure 34**d in **Figure 34**e, which will contrast with the mapped result of the same feature through depth-migration on **Figure 35**e.

Figure 35a is a representative vertical cross section through seismic amplitude of the depth-migrated volume. Figure 35c and Figure 35d show the zoomed-in areas on the both red rectangles. **Figure 35**b shows the interpreted faults in the given volume. Notice how the confidence in the fault mapping process increases after depth migration. Also note that depth migration shows the intrusions dip to be considerably flatter. The depth migration also presents better continuity of reflections toward the right side, in contrast with the time-migrated, depth-converted image. In the depth-migrated image the intrusion appears clearly cut by a nearly vertical fault, as shown in Figure 35e. This fault does not appear in the time-migrated image shown in **Figure 34**e. Also, the depth-migrated intrusion exhibits a steeper dip than its time-migrated, depth converted counterpart.

Outcrop-based models seismic attribute response

Different authors have shown that forward modeling is a useful tool for studying the seismic expression of igneous intrusions (Magee et al., 2015; Eide et al., 2017). Magee et al. (2015) show that the appearance of intrusions in seismic data is controlled by parameters such as the thickness of the intrusion, the frequency of the source wavelet and the fracture style of the host rock. It therefore follows that seismic attributes can help to characterize such features. From the geometric models in Figure 33 I generated reflectivity series which were then convolved with different wavelets to generate synthetic seismograms. Figure 36 through 38 show the expression through different seismic attributes of computed from the synthetic seismograms built from the three models, in the absence of noise. For all figures, I evaluate the attribute response for two cases: first, the frequency of the wavelet used for the creation of the synthetic seismogram, and second, the throw of the in-place fault. The modeled thickness for the intrusions is approximately *150* ft. The first and third row of Figure 36 throughFigure 40 displays the seismic attribute response for seismograms computed using a *20* Hz source Ricker wavelet. The second and fourth display the resulting seismograms using a *50* Hz source Ricker wavelet, through a suite of seismic attributes. The first column of each figure from Figure 36-Figure 40 represents the results for the “fault” model described in Figure Figure 33c, the second column will correspond to the “inflated” model and the third to the “overlap” model. I evaluate the case of the in-place fault to be half the thickness of the intrusion, or approximately *75* ft, for subfigures (a), (b), (d), and (e) for Figure 36 through Figure 40. I repeat this process for twice the thickness of the intrusion, or approximately *300* ft, in subfigures (g)- (j). For subfigures (c) and (f), the vertical separation between sills is the same as the thickness of the intrusions, or approximately 150 ft. The horizontal displacement for subfigures (b), (e), (h) and (j) is half the intrusion thickness, or approximately 75 ft.

In Figure 36 I examine the seismic amplitude response. Faults and oblique displacements are easily discernible for the “faulted” and “inflated” model, with higher frequencies showing a more condensed and clearer image of the reflectors. Because of the wavelet size in relation to the vertical separation between reflectors, an interference pattern is created in Figure 36c in the overlapping region between the two intrusions. The effect of the interference is to decrease the amplitude of the reflections in the overlapping region. For a higher source wavelet frequency, in Figure 36f, some interference between side lobes and main lobes of the other intrusion takes place, resulting in slightly increased amplitude values in the overlapping region.

Figure 37 shows the results of the seismograms response through coherence. Because this attribute measures the similarity of adjacent traces, I expect low coherence values for my faulted models. Note that for “inflated” model, low frequency cases exhibit a small or inexistent coherence anomaly (Figure 37b and Figure 37h). while high frequency cases display a clear discontinuity in the attribute for a sufficiently large fault throw (Figure 37j). All cases for the “faulted” model show fault displacement resulting in low coherence anomalies. However, this model is not as sensitive to changes in the fault throw as the “inflated” model. The interference patterns present in the "overlap" model are not detected by coherence (Figure 37c and Figure 37f), but the edges of the overlapping zone are clearly defined.

Unlike coherence, curvature is sensitive to changes in the dip of reflectors, such that this attribute is capable of highlighting the small changes in the reflector shape in Figure 38b and Figure 38h. Since the configuration of the "faulted" model is of perfectly flat reflectors on each side of the fault, the resulting curvature is zero. For the "inflated" model, curvature anomalies are clearly distinguished on each side of the fault, with decreasing curvature magnitudes as the source frequency increases. For the "overlap" model, curvature only highlights edges of overlapping zone, probably due to the algorithm interpreting interference patterns as "signal". If the interference is not present due to a higher source wavelet frequency, then the curvature anomaly disappears (Figure 38f).

In Figure 39, I compute the envelope (Taner et al., 1979), which is a measure of the reflection strength, and is independent of the phase. The envelope times the cosine of the phase reconstructs the original seismic amplitude data. Like the original seismic amplitude, the envelope follows the shape of the reflector and respects any discontinuity present. However, the envelope highlights the interference patters for the "overlap" model in a better way than seismic amplitude itself. Examining Figure 38c, note that the decrease in amplitude envelope becomes evident in the overlapping zone (Figure 39c), while it increases in the same region for Figure 39f.

Among the plethora of spectral decomposition attributes (Marfurt, 2018) I choose the peak magnitude of spectral components to highlight the behavior of my models in the frequency domain. The results are displayed in Figure 40. In the same way as the amplitude attributes, spectral peak magnitudes do not show any special behavior for the "faulted" or "inflated" models, except for the fact that they only highlight the top of the intrusion. This is due to my layers having thicknesses below tuning, and so spectral magnitudes will merge and only recognize one event in this interference (Machado et al., 2020). Although exhibiting a similar response in every case for the "faulted" and "inflated" models, the spectral magnitude differs from the amplitude envelope in that the interference pattern for low frequencies of the "overlap" model shows a magnitude high (Figure 40c) as opposed to an envelope low (Figure 39c). For high frequencies, the spectral magnitude also displays a magnitude high (Figure 40f).

Comparison with real depth-migrated seismic data

While forward modeling provides a powerful tool for understanding the seismic response of specific geological geometries to wavelet interactions, I need to examine the actual seismic responses of what I believe are mafic diabase intrusions in a felsic granite basement host rock to validate my interpretations.

Figure 41 shows a vertical cross section through a seismic volume in Payne County, Oklahoma, through different attributes (seismic amplitude, coherence, k_1 most positive curvature, peak spectral magnitude, peak spectral frequency and envelope). I observe that like my simple geological models, the basement intrusions are characterized as high amplitude coherent reflectors with different curvature values, high spectral peak magnitudes and envelope and an overall peak spectral frequency of approximately 5 cycles/kft. I zoom-in to a specific area, highlighted by the red square, where I hypothesize that the intrusions correspond to the geometries observed in outcrops and modeled in this paper. The shallower intrusion would correspond to the "faulted" model and the deeper intrusion to the "inflated" model. I display the zoomed-in results in Figure 42.

The seismic amplitude response of both zoomed-in reflectors in Figure 42 is high, showing a discontinuity for the top intrusion, but fully continuous for the low one. For the top reflector, such interruption is characterized by a vertical, low coherence anomaly, which does not appear to cut through the deeper intrusion. In contrast, the deeper intrusion shows higher magnitudes of most positive curvature, consistent with the contrasts observed for both coherence and most positive curvature analysis of the “faulted” and the “inflated” models in Figure 37 and Figure 38. Such responses confirm my hypothesis of geometries consistent with the proposed models. I also observe interference patterns that, similarly to the “overlap” model, cause a low envelope in the top intrusion that is also characterized by a low amplitude envelope. Such behavior is probably caused by the relationship between the intrusion thickness and the wavelet size at that depth. Finally, both intrusions exhibit a spectral peak frequency of approximately 5 cycles/kft.

Limitations

Forward modeling coupled with seismic attributes provides a powerful means to characterize and understand igneous intrusions in seismic volumes. However, a few observations need to be done in order to ascertain the limitations of the workflows I propose.

First, my synthetics were noise free. Seismic processors and interpreters commonly have to deal with many different types of noise that can hinder the exploration or development project. For example, acquisition footprint commonly contaminates the shallower parts of the seismic data volume. High amplitude direct and refracted waves can mask the signal associated with deeper subsurface reflections of interest. Ground roll, bad receiver coupling and other logistical problems may tarnish the quality of the final seismic volume. None of these noise sources was modeled in the synthetic seismograms. Attention should be given how such artifacts can affect the final computed seismic attribute (Cahoj et al., 2015).

Second, for the reprocessing of the original gathers, I encounter two major limitations in using the 3D surface seismic data in estimating the velocity of the deeper reflectors. First, and most important, the largest source-receiver offsets are approximately *10,000* ft, the top of basement is approximately *6,000* ft, while the basement features to be imaged range between *10,000* and *30,000* ft. Assuming flat reflectors and a basement velocity of *20,000* ft/s, the angles of incidence at a depth of *20,000* ft are less than *25°* and at *30,000* ft are less than *20°*, resulting in very small moveout. Given the faulted nature of the deeper reflectors, it is also difficult to differentiate between specular reflections and diffracted energy. Mistakenly applying velocity analysis to deep, but strong diffracted events may give rise to erroneously high apparent velocities.

Third, given the high number and types of seismic attributes that exist in commercial and research software, special care needs to be taken care to assure that the attributes selected are computed independently of each other (Lubo and Marfurt, 2019; Marfurt, 2018). Mistakenly computing mutually dependent seismic attributes can give the impression of a consistent geologic expression while in fact I am seeing a consistent mathematical expression. I propose that, where possible, well information be utilized to corroborate interpretations done from my proposed workflow, to avoid fatal errors of planning and execution. For my current project, given the depth of the targets I am imaging, and the fact that they are limited to basement rocks, no well logs were available that would permit a corroboration of the interpretations generated.

Discussion and conclusions

Igneous intrusions within igneous host rocks have not been studied in seismic data to the extent that igneous intrusions in sedimentary rocks. Seismic data provides a powerful tool for understanding their geometries and interactions with other geological features, as well as lateral and vertical extent. Therefore, determining the limits of seismic resolution and detectability for igneous intrusions becomes crucial for a better understanding their effects over the tectonic evolution of basins and over the petroleum system elements in place. By utilizing a simple wedge model and realistic rock parameters, I have estimated the limits for seismic resolution of basement intrusions in a seismic volume from Payne County, Oklahoma. Such modeling was performed in the absence of noise, and care should be taken to understand to extend these results to other areas with similar magmatic intrusions.

In order to further improve current workflows for analyzing igneous intrusions within a different host rock, I have forward modeled intrusions observed from outcrops and constructed simple models and their corresponding synthetic seismic response. I have applied a suite of seismic attributes to such seismograms to isolate their complex wavelet response and understand how to effectively use them for better characterization of mafic intrusions within an igneous host rock. I then compare the modeled results to those obtained from a real seismic volume and find that similar attribute responses can aid to identify the sill emplacement mechanism that takes place deep in the basement of my study region.

Most studies conducted on igneous intrusions are performed through the use of time migrated seismic data. While good at preserving original amplitude of events, time migration suffers from limitations in terms of true dip and spatial location of events imaged. To compensate for this, I conducted depth migration to better image the intrusions of interest. I find that, perhaps unsurprisingly, depth migration provides a more accurate depiction of dipping events in the basement, and provides a more continuous and clearer image of igneous intrusions. Events that should be interpreted independently become unambiguous when imaged through depth migration, and some geological features, such as faults, can be revealed likewise.

Acknowledgments

The author would like to first acknowledge an anonymous oil company for providing the seismic data set to facilitate further scientific understanding of basement geology in the state of Oklahoma. Second, I thank Star Geophysics for their most generous assistance with processing and prestack depth migration, providing technical expertise and software capabilities for most of the tasks performed. I acknowledge Schlumberger for Petrel licenses used for display purposes, and Landmark for Promax SeisSpace used in the processing and depth migration. I would also like to acknowledge friends and colleagues who have provided meaningful contributions: Abidin Caf, Thang Ha and Bin Lyu.

References

Baer, G., M. Beyth, and Z. Reches, 1994, Dikes emplaced into fractured basement, Timna Igneous Complex, Israel: Journal of Geophysical Research, **99**, 24,039-24,050.

Benson. W. A., 2014, The Spavinaw Granite (Proterozoic), Mayes County, Oklahoma: The Shale Shaker, **65**, 258-264.

Blackford. M. E., and R. D. Lewis, 1979, U-Pb geochronology of exposed basement rocks in Oklahoma: Geological Society of America Bulletin, **90**, 540-544.

Cahoj. M. P., S. Verma., B. Hutchinson., J. Qi., and K. J. Marfurt, 2015, Pitfalls in seismic processing: part 2 velocity analysis sourced acquisition footprint: SEG Technical Program Expanded Abstracts, 3890-3894.

Chopra, S., L. Infante-Paez, and K. J. Marfurt, 2018, Intra-basement intrusions in the STACK area of Oklahoma: AAPG Explorer, May Geophysical Corner. https://explorer.aapg.org/story/articleid/46763/intra-basement-intrusions-in-the-stack-area-of-oklahoma) (Accessed February 27, 2019).

Chopra, S. and K. J. Marfurt, 2007, Seismic attributes for prospect identification and reservoir characterization: SEG Geophysical Developments, **11**, 464p.

Denison. R. E., 1981, Basement rocks in northeastern Oklahoma: Oklahoma Geological Survey Circular 84, 84 p.

Denison, R.E., 1995. Significance of air-photograph linears in the basement rocks of the Arbuckle Mountains: CIRCULAR-OKLAHOMA GEOLOGICAL SURVEY, **97**, pp.119-131.

Eide, C. H., N. Schofield., I. Lecomte., S. Buckley., and J. A. Howell, 2017, Seismic interpretation of sill complexes in sedimentary basins: implications for the sub-sill imaging problem: Journal of the Geological Society of London, **175**, 193-209, https://doi.org/10.1144/jgs2017-096

Etgen, J. T., and C. Kumar, 2012, What really is the difference between Time and Depth Migration? A tutorial, 82nd Annual International Meeting, SEG, Expanded Abstracts, 1-5, doi 10.1190/segam2012-0266.1.

Galland. O., 2012, Experimental modelling of ground deformation associated with shallow magma intrusions: Earth and Planetary Science Letters, **317**, 145-156

Gilbert, M.C., 1983. Timing and chemistry of igneous events associated with the southern Oklahoma aulacogen: Developments in Geotectonics, **19**, pp. 439-455.

Hanson, R.E., R. E. Puckett Jr, G. R. Keller, M. E. Brueseke, C. L. Bulen, S. A. Mertzman, S. A. Finegan. and D. A. McCleery, 2013. Intraplate magmatism related to opening of the southern Iapetus Ocean: Cambrian Wichita igneous province in the Southern Oklahoma rift zone. Lithos, **174**, pp.57-70.

Hawes, J., 1952. A magnetic study of the Spavinaw granite area: Oklahoma. Geophysics, **17**(1), pp.27-55.

Johnson, K.S., 1991, Geologic overview and economic importance of Late Cambrian and Ordovician rocks in Oklahoma, in Johnson, K. S., ed., Late Cambrian-Ordovician geology of the southern Midcontinent, 1989 Symposium: Oklahoma Geological Survey Circular 92, p.3-14.

Johnson, K. S., 2008, Geologic History of Oklahoma, Educational Publication 9

Jones, I. F., R. I. Bloor, B. L. Biondi, and J. T. Etgen, 2008, Prestack depth migration and velocity model building: SEG Geophysics Reprints Series No. 25.

Infante-Paez. L., and K. J. Marfurt, 2017, Seismic expression and geomorphology of igneous bodies: A Taranaki Basin, New Zealand case study: Interpretation, 5, SK121-SK140, https://doi.org/10.1190/int-2016-0244.1

Keller, G.R., T. A. Stephenson, R. D. Hatcher, M. P. Carlson, and J. H. McBride, 2007. The southern Oklahoma and Dniepr-Donets aulacogens: A comparative analysis: Memoirs-Geological Society of America, **200**, p.127.

Kibikas, W. M., B. M. Carpenter, and A. Ghassemi, 2019, The Petrophysical and Mechanical Properties of Oklahoma's Crystalline Basement: American Rock Mechanics Association.

Kolawole, F., B. M. Carpenter, and M. Simpson-Turko, 2019, The intra-basement reflectors in the STACK area of Oklahoma: What are they really?: AAPG Explorer, April Geophysical Corner.

Lidiak, E.G., R. E. Denison, and R. J. Stern, 2014. Cambrian (?) Mill Creek Diabase Dike Swarm, Eastern Arbuckles: A Glimpse of Cambrian Rifting in the Southern Oklahoma Aulacogen: Oklahoma Geological Survey, Guidebook, **38,** pp.105-122.

Lubo-Robles, D., and K. J. Marfurt, 2019, Independent component analysis for reservoir geomorphology and unsupervised seismic facies classification in the Taranaki Basin, New Zealand: Interpretation, **7**, no. 3, SE19-SE42, doi: 10.1190/INT-2018-0109.1

Machado. G., T. Ha, B. Lyu, K. J. Marfurt, 2020, Limitations to thin bed resolution (to be submitted).

Magee. C., C. A. L. Jackson., and N. Schofield, 2013, The influence of normal fault geometry on igneous sill emplacement and morphology: Geological Society of America, **41**, 407-410.

Magee. C., S. M. Maharak., R. Wrona., and C. A. L. Jackson., 2015, Controls on the expression of igneous intrusions in seismic reflection data, Geosphere, **11**, 1024-1041.

Magee, C., J. D. Muirhead, A. Karvelas, S. P. Holford, C. A. Jackson, I. D. Bastow, N. Schofield, C. T. Stevenson, C. McLean, W. McCarthy, and O. Shtukert, 2016, Lateral magma flow in mafic sill complexes: Geosphere, **12**, 809–841, doi: 10.1130/GES01256.1.

Marfurt, K. J., 2018, Seismic attributes as the framework for data integration throughout the oilfield life cycle: Society of Exploration Geophysicists, Distinguish Instructor Series.

Merritt, C.A., 1960, Petrography of the Spavinaw Granite: Oklahoma Geological Notes, **20**, 224-288.

Senger. K., J. Millet., S. Planke, K. Ogata, C. H. Eide., M. Festoy, O. Galland, and D. A. Jeram, Effects of igneous intrusions on the petroleum system: a review: First Break, **35**, 47-56.

Shah. A. K., and G. R. Keller, 2017, Geologic influence on induced seismicity: Constraints from potential field data in Oklahoma: Geophysical Research Letters, **44**, 152-161.

Schofield. N., S., S. Holford, J. Millet, D. Brown, D. Jolley, S. R. Passey, D. Muirhead, C. Grove, C. Magee, J. Murray, M. Hole, C. A. –L. Jackson, and C. Stevenson, 2015, regional magma plumbing and emplacement mechanisms of the Faroe-Shetland Sill Complex: implications for magma transport and petroleum systems within sedimentary basins: Basin research, **29**, 41-63.

Sheriff. R. E., and L. P. Geldart, 1995, Exploration Seismology: 2nd edition Cambridge University Press, Cambridge.

Stein, C.A., S. Stein, M. Merino, G. R. Keller, L. M. Flesch, D. M. Jurdy, 2014. Was the Mid-continent Rift part of a successful seafloor-spreading episode?: Geophys. Res. Lett. **41**, 1465–1470.

Stein, S., C. A. Stein, R. Elling, J. Kley, G. R. Keller, M. Wysession, T. Rooney, A. Frederiksen, R. Moucha, 2018. Insights form North America’s failed Midcontinent Rift into the evolution of continental rifts and passive continental margins: Tectonophysics, **744**. p. 403-421.

Stephens. T. L., R. J. Walker., D. Healy., A. Bubeck., R. W. England., K. J. W. McCaffrey, 2017, Igneous sill record far-field and near-field stress interactions during volcano construction: Isle of Mull, Scotland, **478**, 159-174.

Taner, M. T., E. Koehler, and R. E. Sheriff, 1979, Complex seismic trace analysis: Geophysics, **44**,1041-1063.

Thomas, J.J., R. D. Shuster, and M. E. Bickford, 1984. A terrane of 1,350-to 1,400-my-old silicic volcanic and plutonic rocks in the buried Proterozoic of the mid-continent and in the Wet Mountains, Colorado: Geological Society of America Bulletin, **95**(10), pp.1150-1157.

Thomsom. K., and N. Schofield, 2008, Lithological and structural controls on the emplacement and morphology of sills in sedimentary basins: Geol. Soc. Lond. Spec. Publ, **302**, 31-44.

Yilmaz, O., 2001, Seismic data analysis: processing, inversion and interpretation of seismic data: Society of Exploration Geophysicists.

Widess, M., 1973, How thin is a thin bed?: Geophysics, **38**, 1176-1180.

Figures

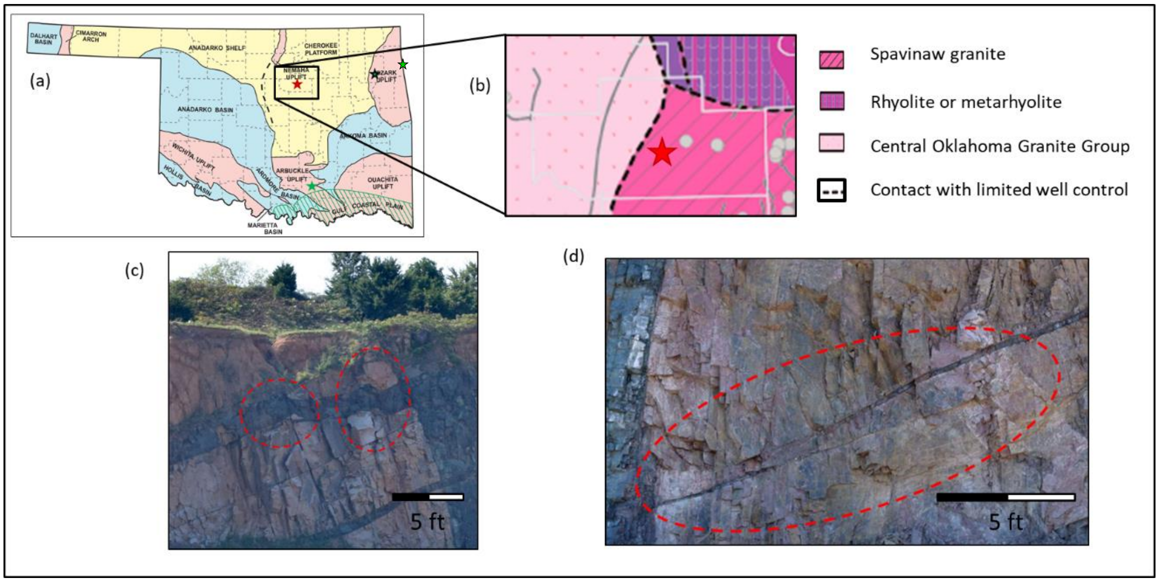
(a)
DALHART BASIN
CIMARRON ARCH
ANADARKO SHELF
CHEROKEE PLATFORM
NEMAHA UPLIFT
OZARK UPLIFT
ANADARKO BASIN
ARKOMA BASIN
WICHITA UPLIFT
HOLLIS BASIN
ARBUCKLE UPLIFT
ARDMORE BASIN
OUACHITA UPLIFT
GULF COASTAL PLAIN
MARIETTA BASIN
(b)
Spavinaw granite
Rhyolite or metarhyolite
Central Oklahoma Granite Group
Contact with limited well control
(c)
5 ft
(d)
5 ft

Figure 29. (a) Map of geologic provinces of Oklahoma, with red star indicating location of seismic survey in Payne county (modified from Johnson, 2008) and blue star indicating location of outcrops in (c) and (d). The green star indicates the outcrop of the Spavinaw Granite host rock. (b) Map of geologic interpretation of basement rocks based on geophysical and drill hole data (modified after Shah and Keller, 2017). (c) and (d) are photographs of characteristic geometries observed in diabase sills in granite host rock, south Oklahoma. (c) shows intrusion interaction with pre-existent fracture in place, while (d) represent the interaction of mafic sill in the absence of a pre-existing fracture.

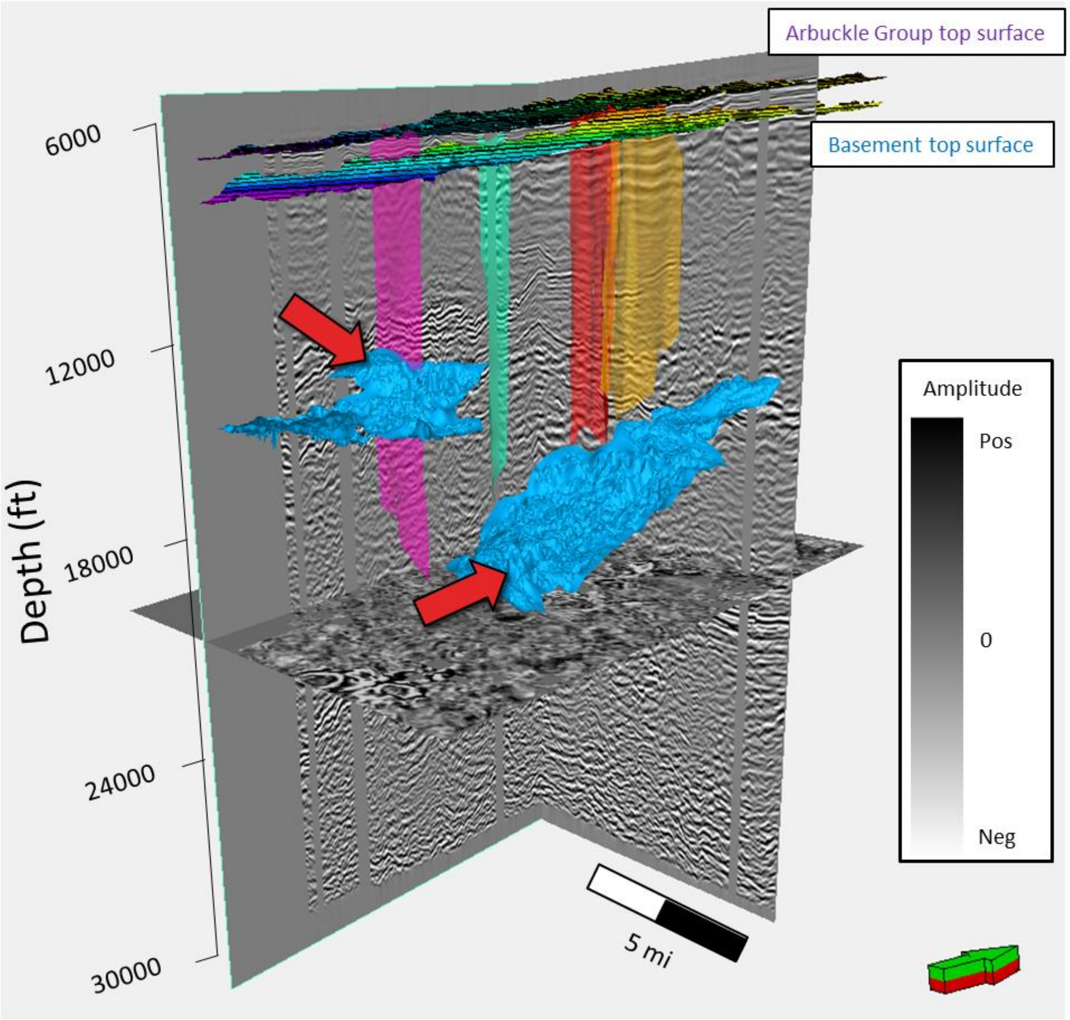
Arbuckle Group top surface
Basement top surface
Depth (ft)
6000
12000
18000
24000
30000
Amplitude
Pos
0
Neg
5 mi

Figure 30. Chair display of time-migrated, depth-converted seismic amplitude volume used in this study showing the Top Arbuckle Group and Top Basement surfaces, along with four interpreted basement faults as colored polygons. Red arrows indicate mapped amplitude anomalies interpreted in the basement as mafic intrusions (after Kolawole et al., 2019).

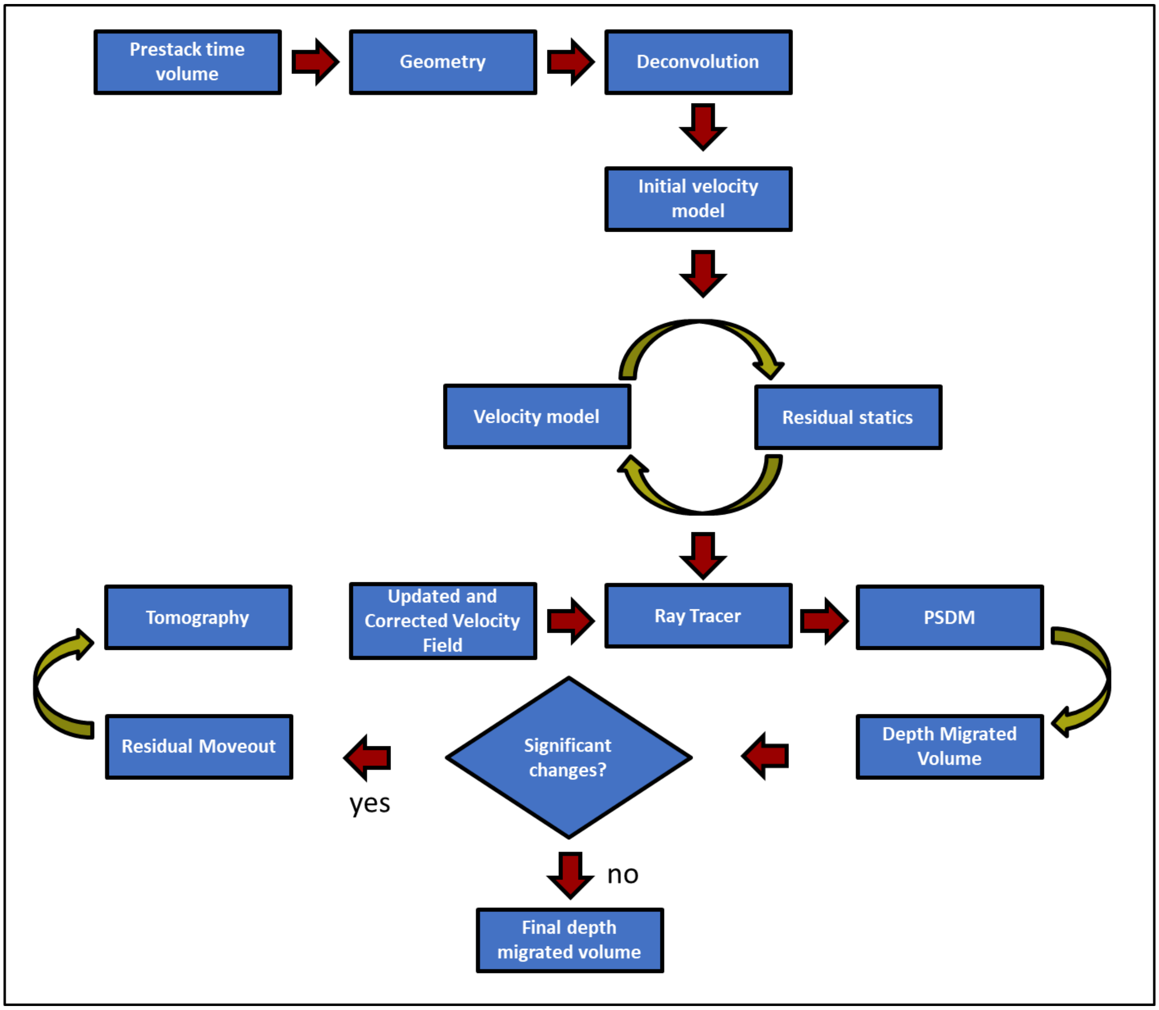
Prestack time volume
Geometry
Deconvolution
Initial velocity model
Velocity model
Residual statics
Tomography
Updated and Corrected Velocity Field
Ray Tracer
PSDM
Residual Moveout
Significant changes?
Depth Migrated Volume
yes
no
Final depth migrated volume

Figure 31. Workflow for depth migrating the seismic volume. Three iterations of velocity spectral semblance analysis and residual statics were computed before improving the velocity further using a tomographic solution. Two iterations of PSDM were computed before converging to a depth migration volume.

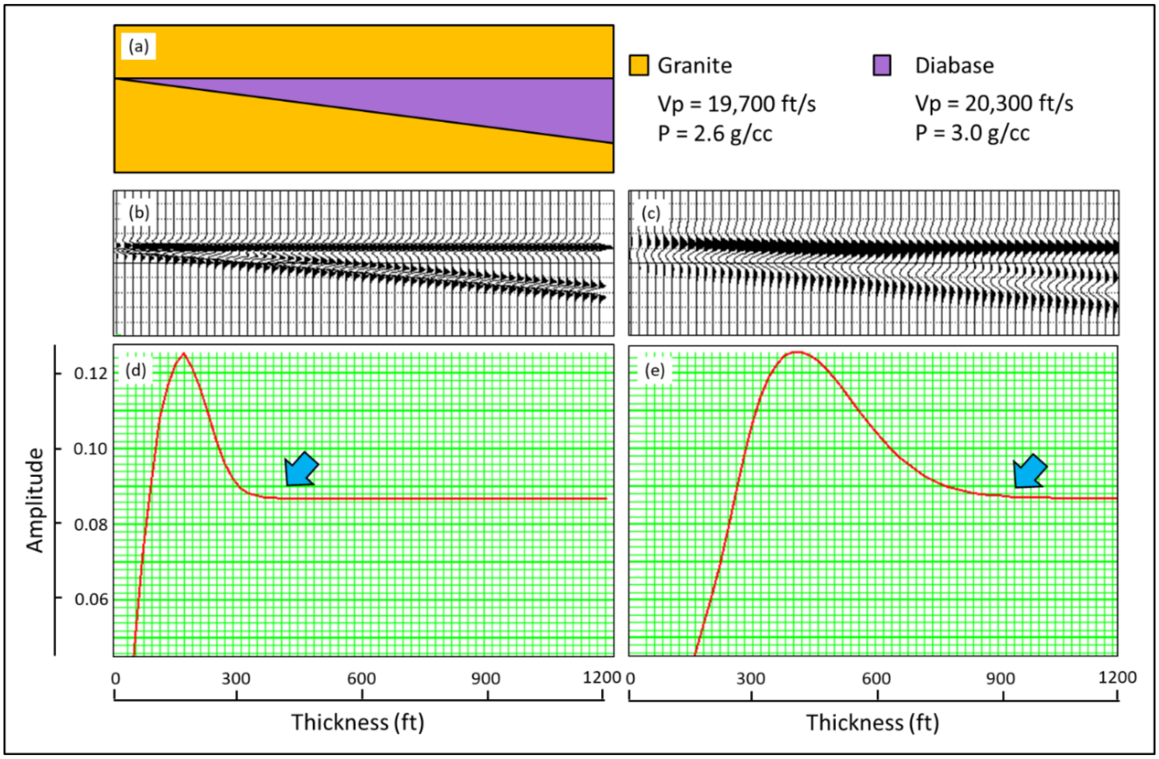

Figure 32. Wedge model generated to test the limits of seismic resolution of diabase intrusions on granite host rock. (a) Conceptual model geometry of mafic diabase intrusion in felsic granite basement rock. The model contains a wedge with a 0-1200 ft varying thickness thinning towards the left. Reflectivity coefficients calculated from (a) are convolved with a 20 Hz and 50 Hz Ricker wavelet to generate synthetic seismograms in (b) and (c). Amplitude vs thickness plots are constructed for (b) and (c) in (d) and (e). Blue arrows indicate the onset of tuning for both cases. Peak in amplitude occurs at 160 ft for (d) and 400 ft for (e). Thickness less than these cannot be estimated through conventional two-way traveltime analysis (Widess, 1973). Note that beds of different thicknesses may exhibit the same amplitude response, hence amplitude is not a reliable indicator of thickness for this model below a specific threshold.

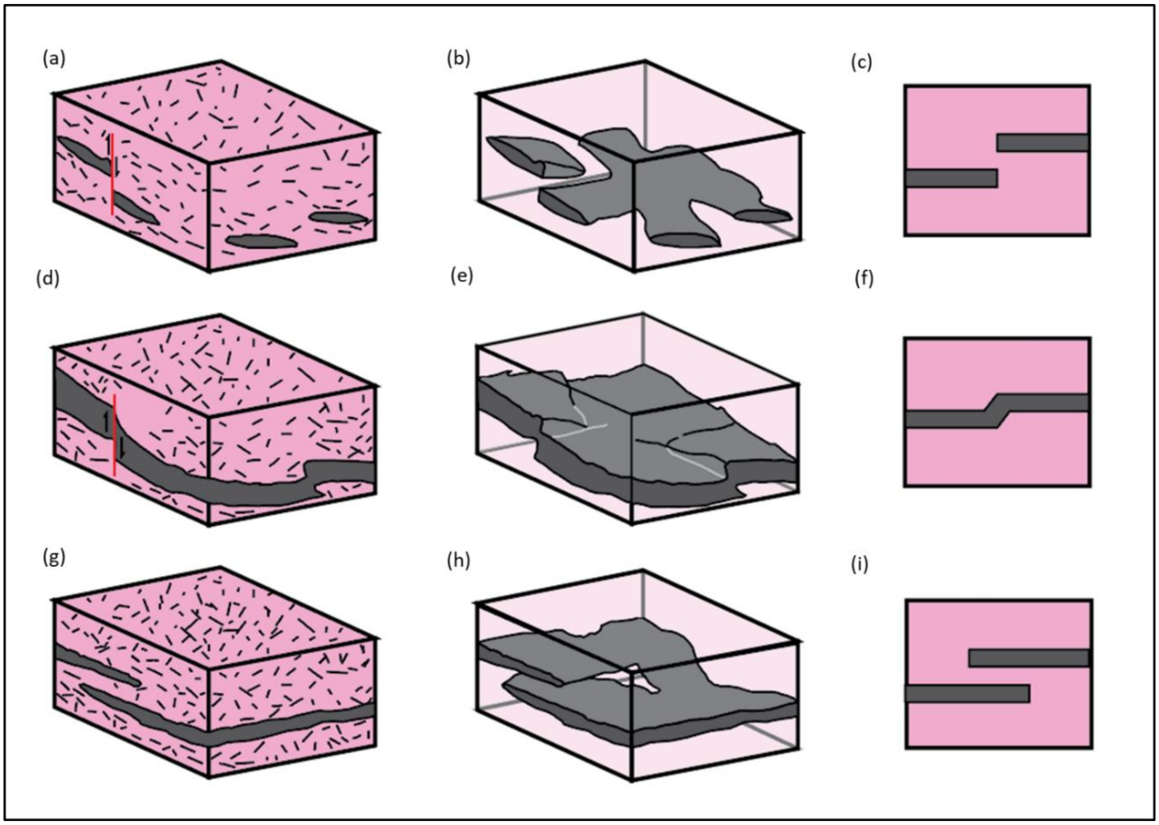

Figure 33. Conceptual and geometric models of diabase sills hosted in granite host rock in the presence or absence of pre-existing faults (modified from Stephens et al., 2017). (a) and (b) Conceptual models of mafic emplacement in an early stage of shallow intrusion with magma segments adjacent to a steep discontinuity. (c) my corresponding synthetic model. (d) and (e) Conceptual model of mafic emplacement in later stages of shallow intrusion with magma segments inflation of the initial sill segments leading to linkage through stepping or breached relay structures. (f) my corresponding synthetic model. (g) and (h) Conceptual models of mafic emplacement in the absence of pre-existing discontinuities that lead to the development of sub-parallel sill segments. (i) my corresponding synthetic model.

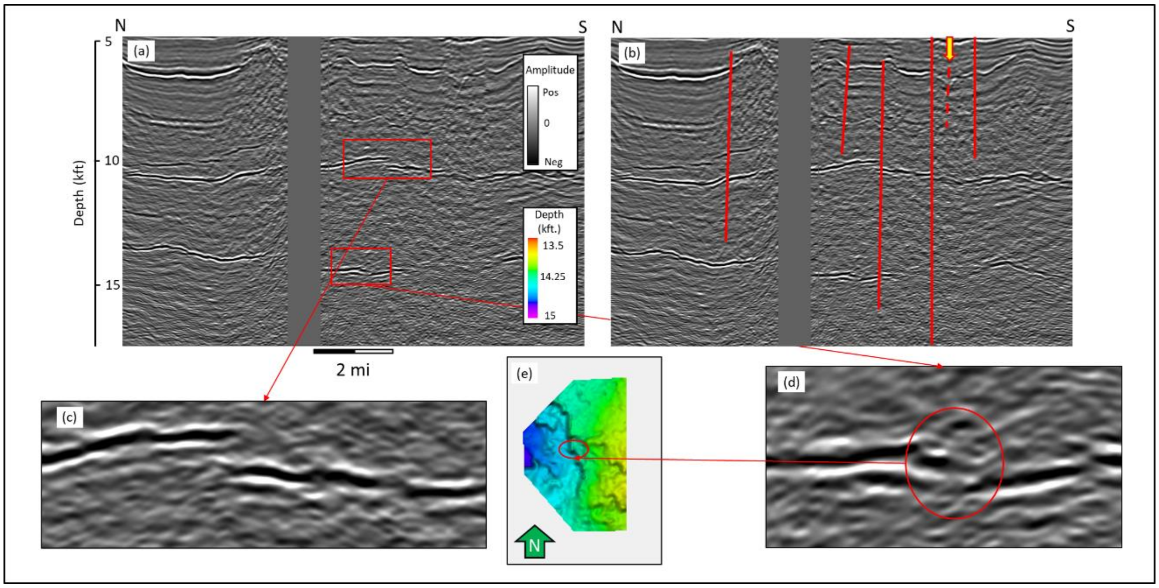

Figure 34. (a) Representative vertical cross section of time-migrated, depth-converted seismic amplitude volume. The blank area in the middle of the line is due to lack of a seismic acquisition permit. (b) highlights my fault interpretation. Red rectangles are zoomed-in mafic intrusions in (c) and (d). Depth conversion was performed with the same velocity model as in depth conversion in **Figure 35**. The intrusion from (d) was mapped in (e) Red ellipses highlights interpreted fault defining geometry of reflector after time migration.

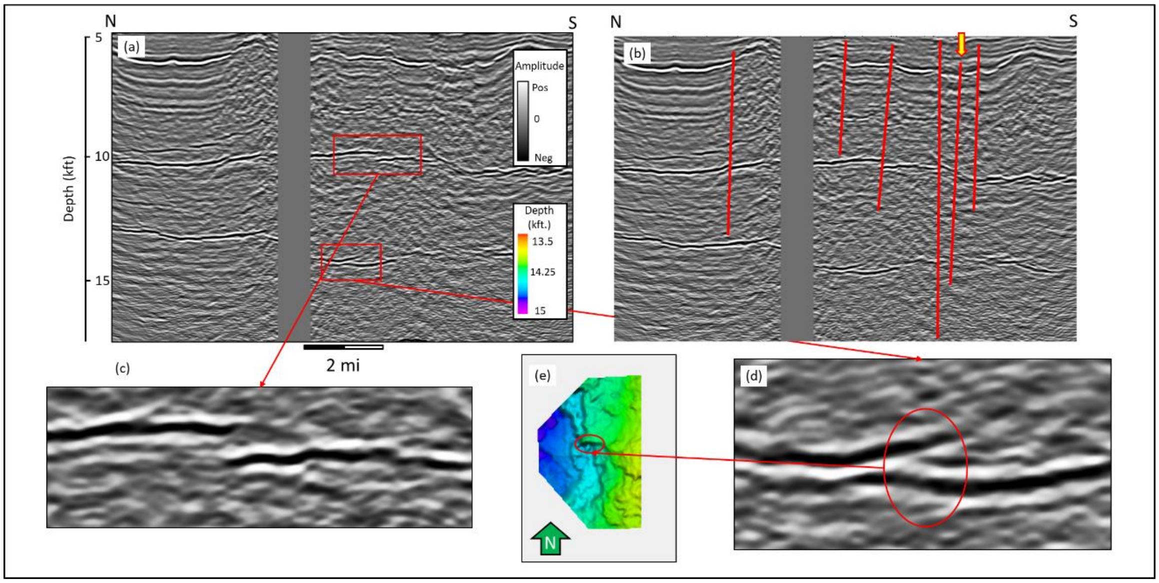

Figure 35. (a) Representative vertical cross section of depth-migrated seismic amplitude volume. The blank area in the middle of the line is due to lack of a seismic acquisition permit. (b) highlights my fault interpretation. Red rectangles are zoomed-in mafic intrusions in (c) and (d). Depth migration was performed with the same velocity model as in depth conversion. Depth migration and depth conversion were performed with the same velocity model. Notice that after depth migration, the overall appearance of such intrusion is flatter. The intrusion from (d) was mapped in (e) Red ellipses highlights interpreted fault defining geometry of reflector not seen in time-migrated, depth converted data.

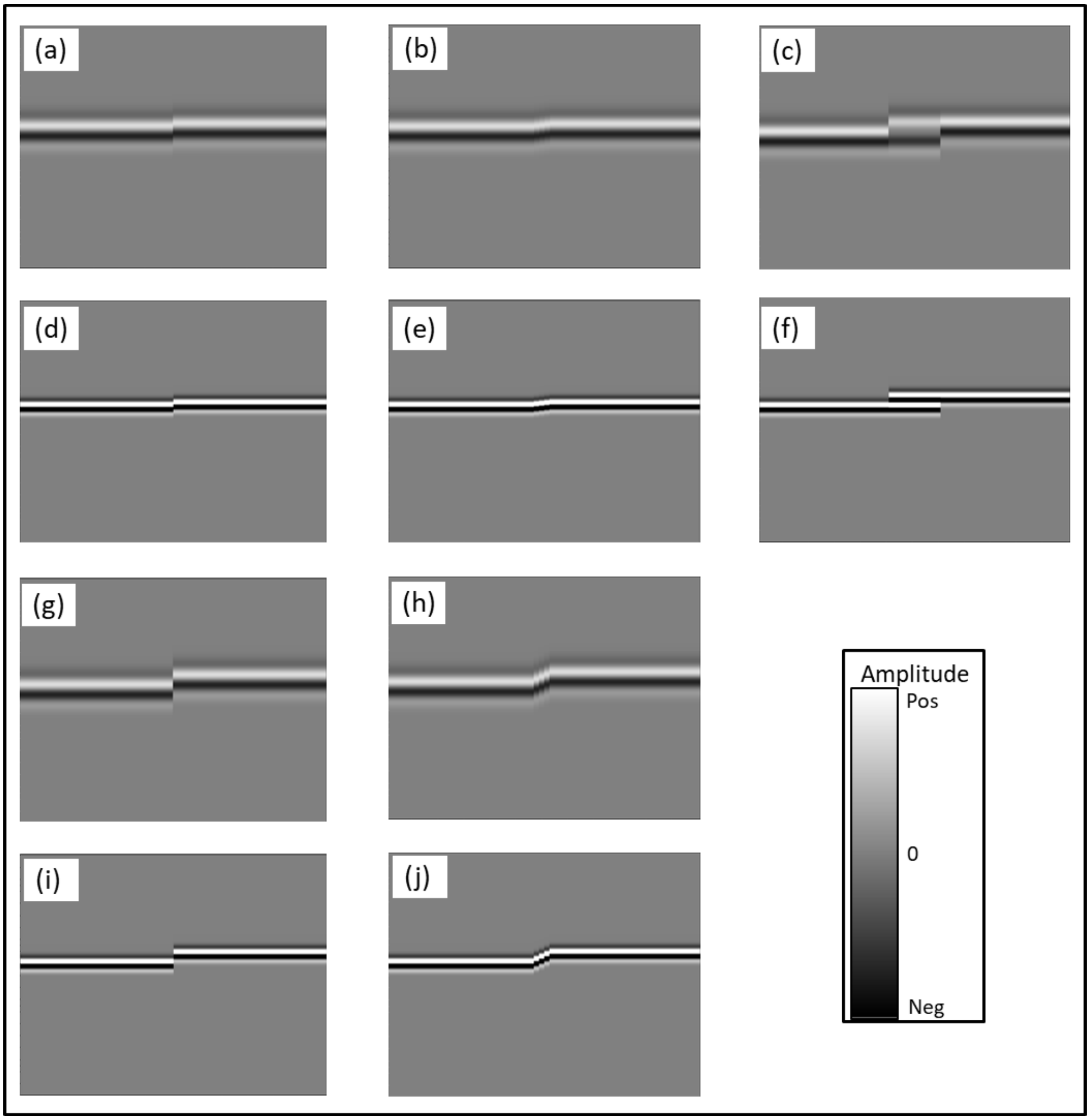

Figure 36. Synthetic models of diabase intrusions in granite host rock based on outcrop observation through seismic amplitude. The modeled intrusion thickness is approximately 150 ft. First column represents synthetic seismograms for "faulted" model, second column for "inflated" model and third column for "overlap" model. The reflectivity series generated from each geometric model was convolved with a 20 Hz Ricker wavelet (a), (b), (c), (g) and (h) or a 50 Hz Ricker wavelet (d), €, (f), (i), and (j). (a), (b), (d) and (e) are modeled with a fault throw of half he intrusion thickness, or approximately 75 ft; (g), (h), (i) and (j) are modeled with a fault throw of twice the intrusion thickness, or approximately 300 ft. The horizontal displacement for the column corresponding to "inflated" model is half the thickness of the layer, or approximately 75 ft. Separation between sills in "overlap" model is equal to the thickness of the intrusion, or approximately 150 ft. There is a clear contrast between the models generated with a 20 Hz Ricker wavelet and the ones generated with a 50 Hz wavelet in how condensed and clear the reflections appear. Note the wavelet interference patter in (f) due to the closeness of the layers with regards to the size of wavelet. Such interference lowers the overall amplitude of the reflections in the overlapped region.

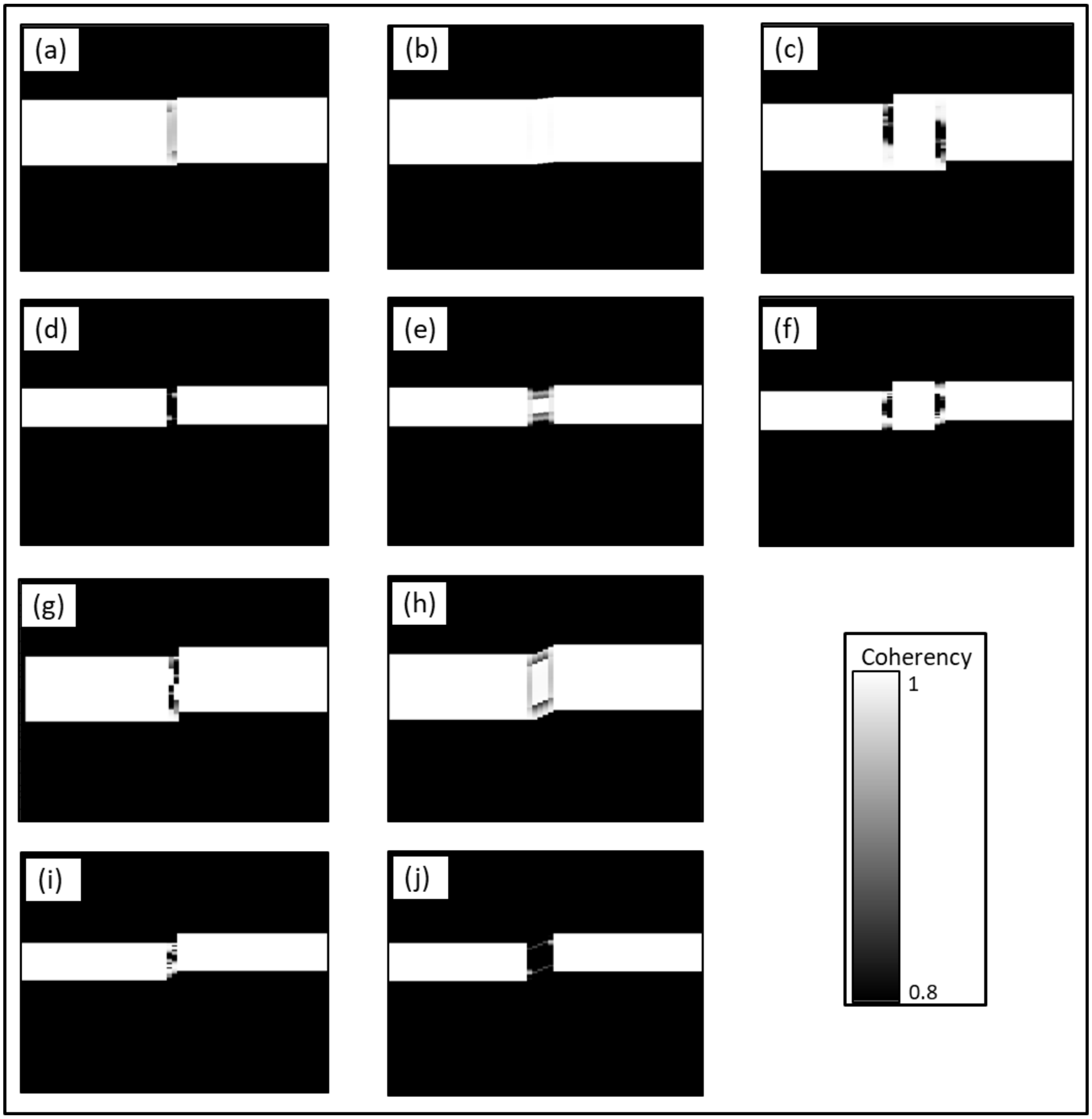

Figure 37. Synthetic models of diabase intrusions in granite host rock based on outcrop observation through coherence. The modeled intrusion thickness is approximately 150 ft. First column represents synthetic seismograms for "faulted" model, second column for "inflated" model and third column for "overlap" model. The reflectivity series generated from each geometric model was convolved with a 20 Hz Ricker wavelet (a, b, c, g and h) or a 50 Hz Ricker wavelet (d, e, f, i and j). (a), (b), (d) and (e) are modeled with a fault throw of half he intrusion thickness, or approximately 75 ft; (g), (h), (i) and (j) are modeled with a fault throw of twice the intrusion thickness, or approximately 300 ft. The horizontal displacement for the column corresponding to "inflated" model is half the thickness of the layer, or approximately 75 ft. Separation between sills in "overlap" model is equal to the thickness of the intrusion, or approximately 150 ft. Low frequency synthetics show more coherence than their high frequency counterparts. Higher fault throws show lower coherence than small fault throws. Wavelet interference patterns from "overlap" model are not detected by coherence, as seen on (c) and (f), but the edges of the overlap are clearly

determined. Even though coherence anomalies from “inflated” model are generally weaker than those exhibited by” faulted” model, a large enough throw will be detected, as shown in (j). In contrast, for “faulted” model, most cases show a distinct coherence anomaly, but a large fault throw does not appear different than a relatively smaller one (compare g with i).

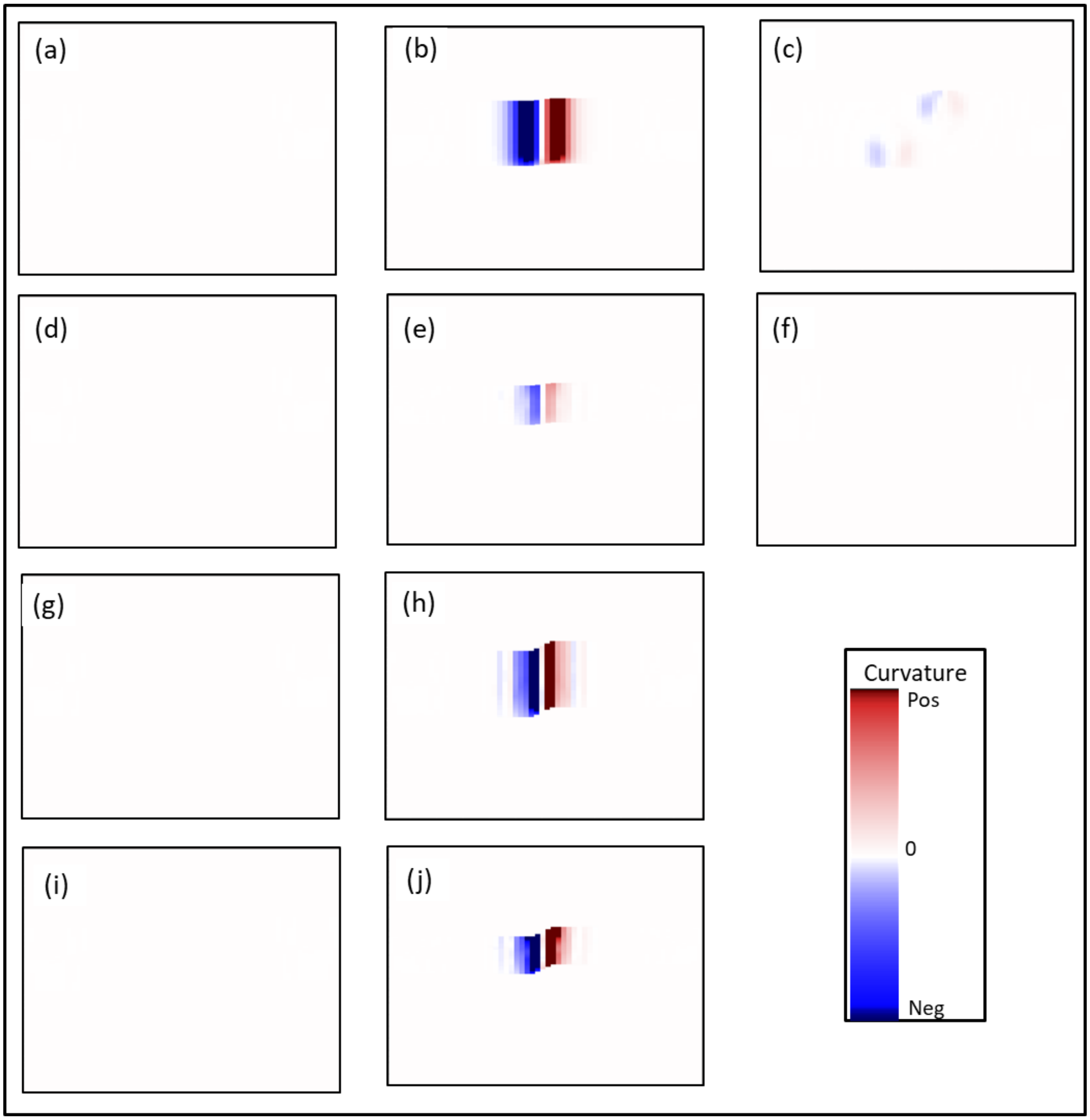

Figure 38. Synthetic models of diabase intrusions in granite host rock based on outcrop observation through curvature. The modeled intrusion thickness is approximately 150 ft. First column represents synthetic seismograms for "faulted" model, second column for "inflated" model and third column for "overlap" model. The reflectivity series generated from each geometric model was convolved with a 20 Hz Ricker wavelet (a, b, c, g and h) or a 50 Hz Ricker wavelet (d, e, f, i and j). (a), (b), (d) and (e) are modeled with a fault throw of half he intrusion thickness, or approximately 75 ft; (g), (h), (i) and (j) are modeled with a fault throw of twice the intrusion thickness, or approximately 300 ft. The horizontal displacement for the column corresponding to "inflated" model is half the thickness of the layer, or approximately 75 ft. Separation between sills in "overlap" model is equal to the thickness of the intrusion, or approximately 150 ft. Because of the configuration of the "faulted" model, no curvature anomaly is detected, as expected, as both sides of the fault are perfectly flat and thus, their curvature is zero. Similarly, for "overlap" model, curvature only partially detects the edges of the model for the low frequency case, due to interference patterns being interpreted as "signal" by the algorithm, but not for the high frequency case. For "inflated" model, the curvature anomaly is present in all cases, seeming to decrease in magnitude with higher frequencies.

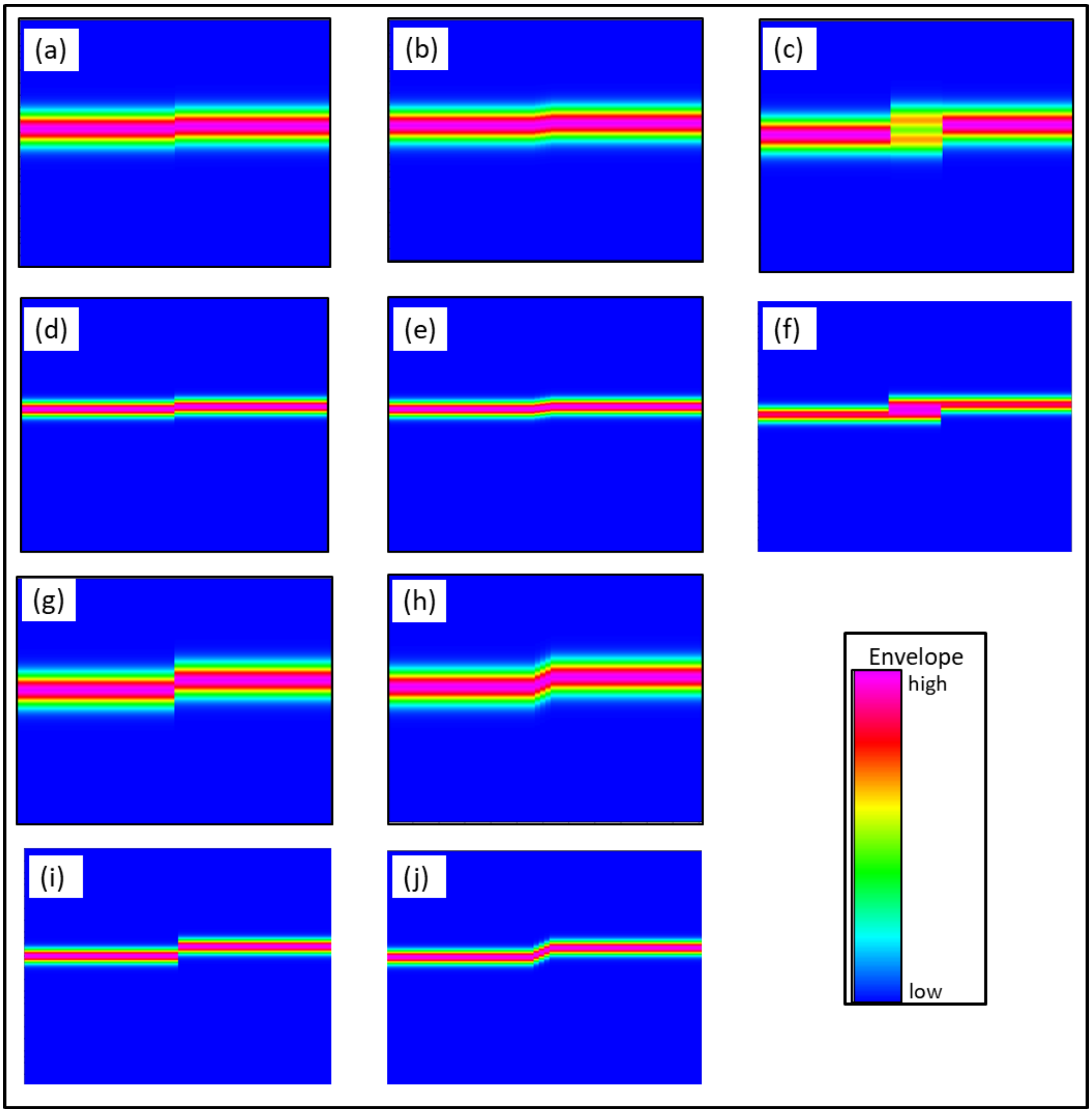

Figure 39. Synthetic models of diabase intrusions in granite host rock based on outcrop observation through curvature. The modeled intrusion thickness is approximately 150 ft. First column represents synthetic seismograms for "faulted" model, second column for "inflated" model and third column for "overlap" model. The reflectivity series generated from each geometric model was convolved with a 20 Hz Ricker wavelet (a, b, c, g and h) or a 50 Hz Ricker wavelet (d, e, f, i and j). (a), (b), (d) and (e) are modeled with a fault throw of half he intrusion thickness, or approximately 75 ft; (g), (h), (i) and (j) are modeled with a fault throw of twice the intrusion thickness, or approximately 300 ft. The horizontal displacement for the column corresponding to "inflated" model is half the thickness of the layer, or approximately 75 ft. Separation between sills in "overlap" model is equal to the thickness of the intrusion, or approximately 150 ft. There are no distinct differences for both the "faulted" and the "inflated" models, both in terms of their response to this attribute when compared with seismic amplitude. The "overlap" model further proves that interference patterns in overlapping region decrease the amplitude of the reflectors in the area for low frequencies, but for high frequencies the amplitude is increased.

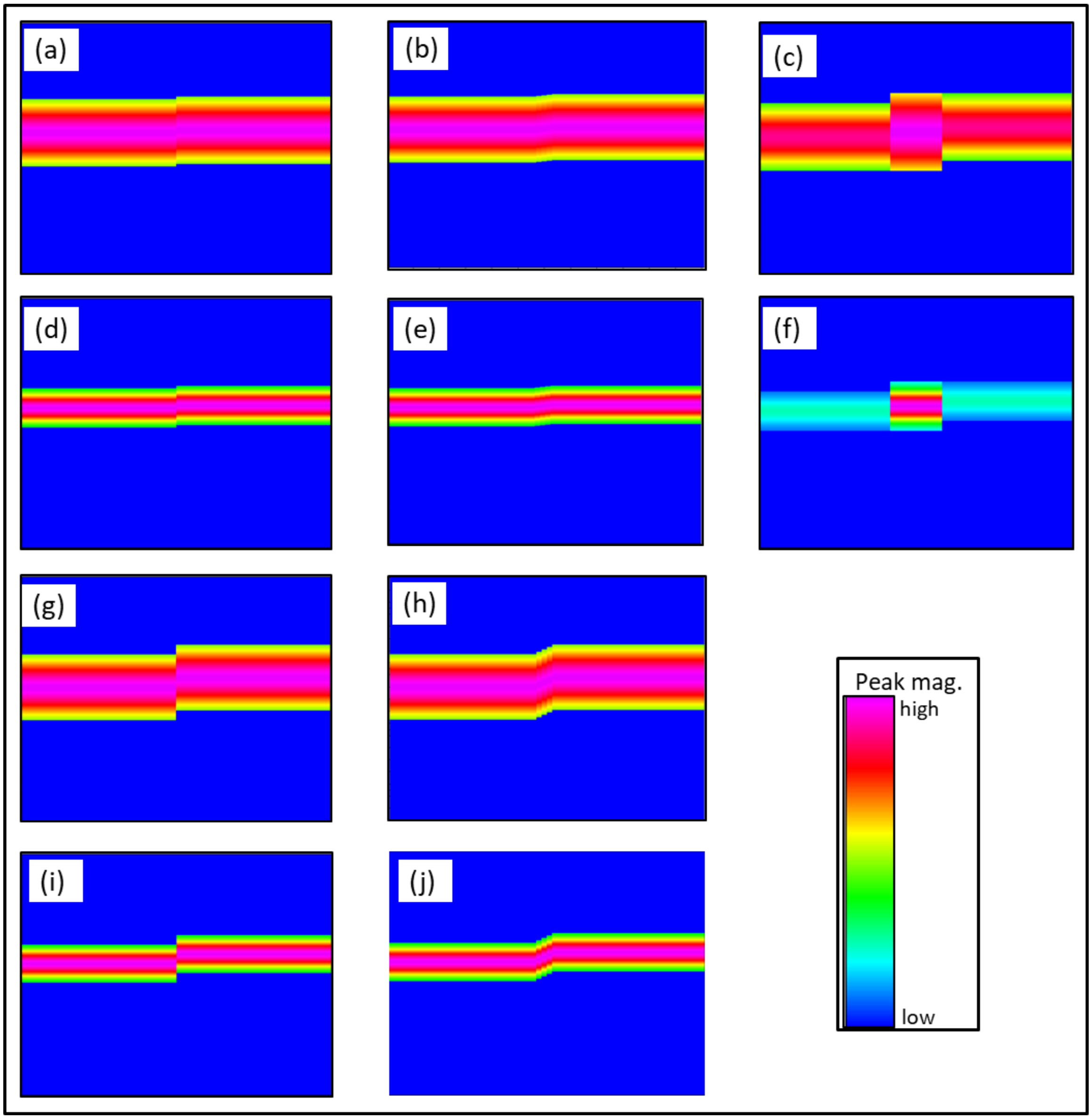

Figure 40. Synthetic models of diabase intrusions in granite host rock based on outcrop observation through curvature. The modeled intrusion thickness is approximately 150 ft. First column represents synthetic seismograms for "faulted" model, second column for "inflated" model and third column for "overlap" model. The reflectivity series generated from each geometric model was convolved with a 20 Hz Ricker wavelet (a, b, c, g and h) or a 50 Hz Ricker wavelet (d, e, f, i and j). (a), (b), (d) and (e) are modeled with a fault throw of half he intrusion thickness, or approximately 75 ft; (g), (h), (i) and (j) are modeled with a fault throw of twice the intrusion thickness, or approximately 300 ft. The horizontal displacement for the column corresponding to "inflated" model is half the thickness of the layer, or approximately 75 ft. Separation between sills in "overlap" model is equal to the thickness of the intrusion, or approximately 150 ft. In a similar way to **Figure 39**, there are no distinct responses of this attributes for "faulted" or "inflated" models when compared with seismic amplitude. The attribute only recognizes one event in all of these cases because the model's thicknesses are below tuning, as shown wit **Figure 32**. In contrast with **Figure 39**, (c) shows an increase in the spectral peak magnitude from the wavelet interference within overlapping zone for the low source wavelet frequency case. In the same way as **Figure 39**f, for the high source wavelet frequency case in (f), there is a distinct increase in the peak magnitude observed in the overlapping zone.

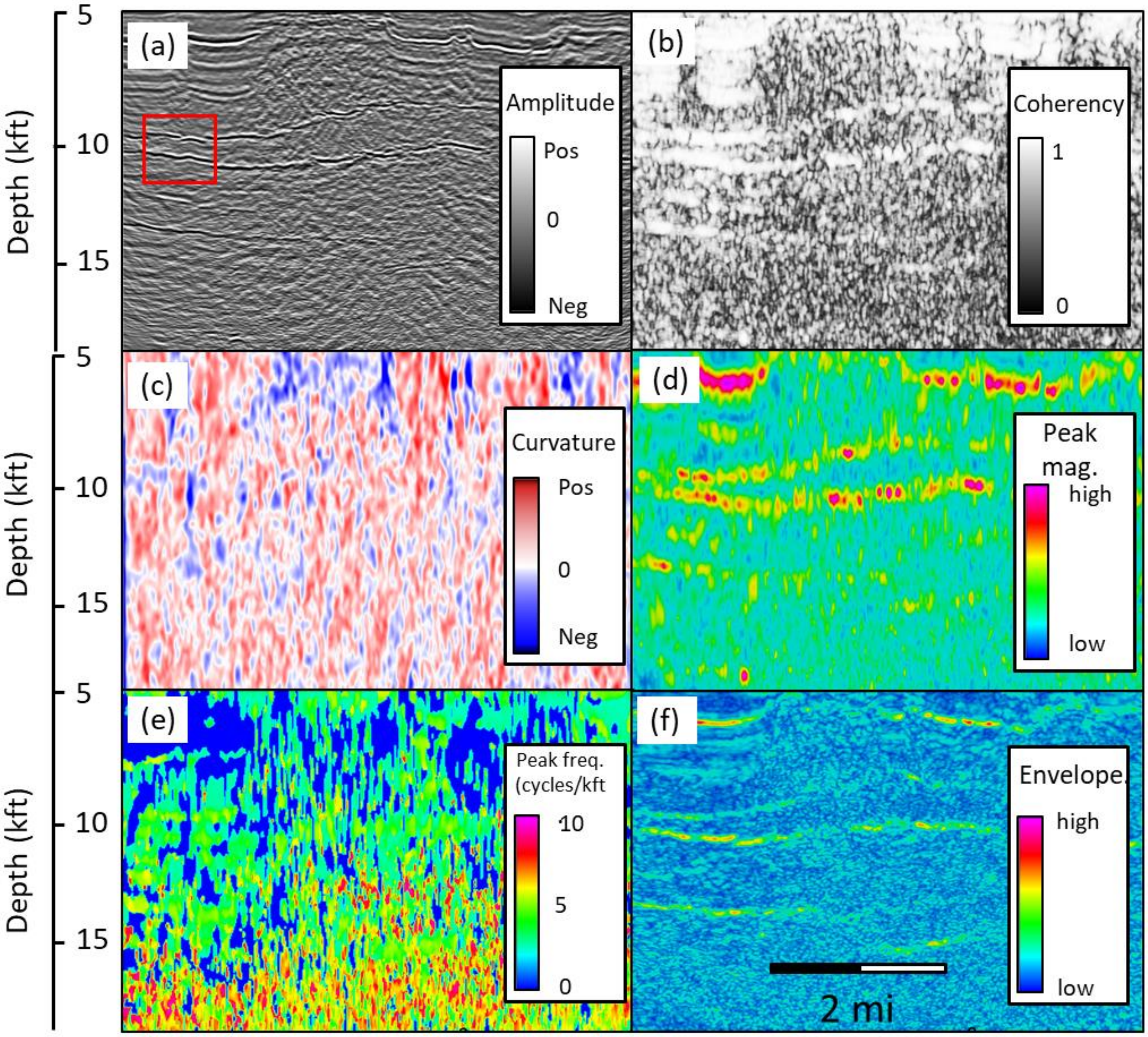

Figure 41. Representative vertical cross section through (a) seismic amplitude, (b) coherence, (c) k_1 most positive curvature, (d) spectral peak magnitude, (e) spectral frequency and (f) amplitude envelope. Red square represents zoomed in area displayed in **Figure 42**. Seismic amplitude anomalies in basement (a) associated with mafic diabase intrusions into felsic granite host rock in basement. These intrusions are characterized by coherent reflectors (b), mixed curvature response (c), high spectral magnitude responses (d) mid-range frequencies (e) and relatively high envelope (f).

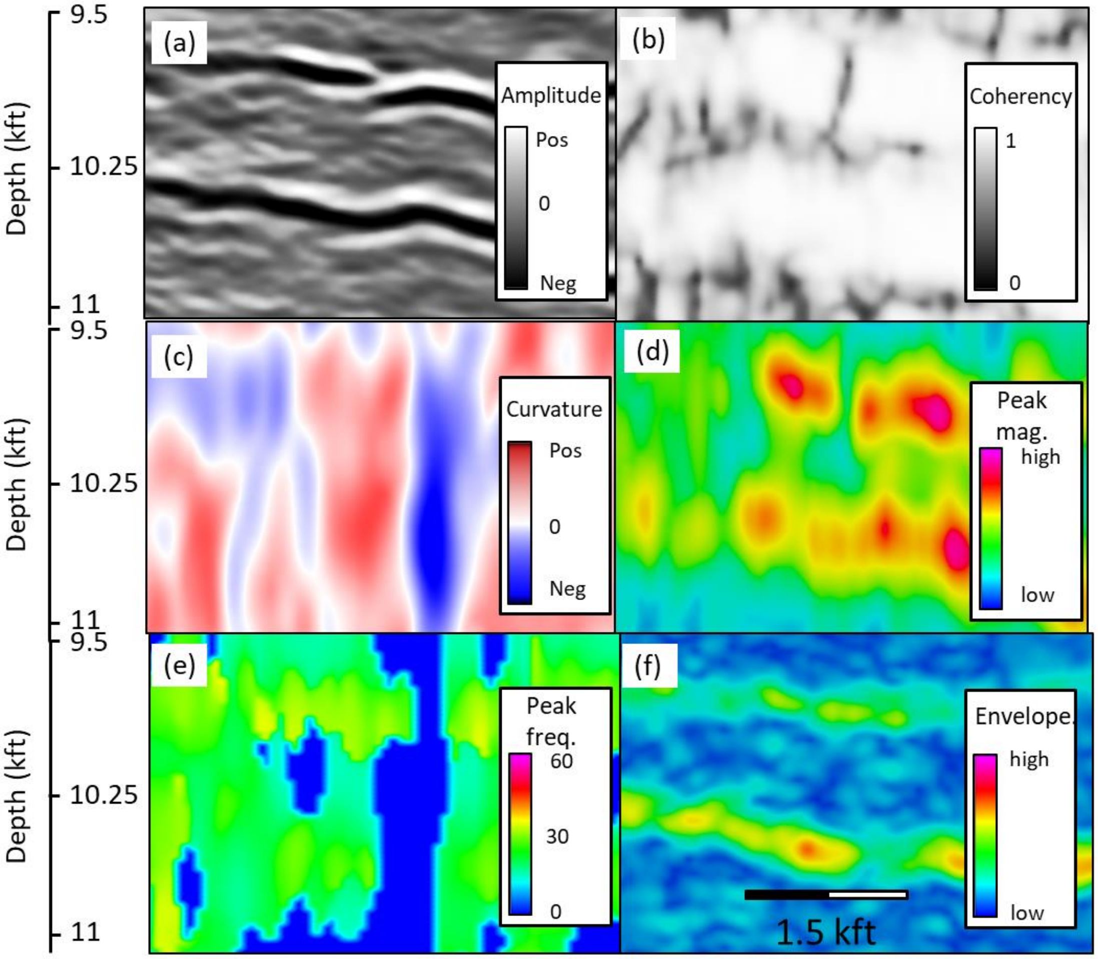

Figure 42. Representative vertical cross section of zoomed in square in **Figure 41** through (a) seismic amplitude, (b) coherence, (c) k_1 most positive curvature, (d) spectral peak magnitude, (e) spectral frequency and (f) amplitude envelope. Two seismic amplitude anomalies examined. Top intrusion exhibits a low coherence lineament cutting vertically through it, unlike low intrusion. Low intrusion displays a higher positive curvature magnitude than top one. Top intrusion displays higher spectral magnitudes than low intrusion, with an inverted trend for the amplitude envelope. Additionally, both intrusions show an interruption of spectral magnitude and amplitude envelope at the location of vertical low coherence lineament. Both intrusions show a peak frequency of approximately 30 Hz.

Chapter 4: Limitations to thin bed resolution

Abstract

Beginning in 1973 with Widess' analysis of reflector wedge models, the conventionally understood limit of vertical seismic resolution has been $\lambda/4$ for noise contaminated data. However, this model and resolution limits do not represent the full range of models that might occurin nature. Most rules of thumb on vertical resolution are based on the resolving power of the dominant frequency of an otherwise broad band wavelet. In this paper, I examine three algorithms designed to increase the limit or at least quantify vertical seismic resolution: spectral balancing, bandwidth extension and the Hölder exponent. I find that spectral balancing provides a useful, but limited improvement of seismic resolution. I find that although bandwidth extension attempts to resolve beds below tuning frequencies by extending the magnitude spectrum, the corresponding phase spectrum interference patterns are not properly unraveled. Events that were previously resolved appear sharper, while those that were not are now corrupted. The goal of the Hölder exponent is to use the shape of the magnitude spectrum to characterize the underlying reflectivity as being blocky, spikey, or smooth. However, the Hölder exponent suffers from the same limitations of other spectral decomposition techniques in the presence of tuning. My work shows that the resolution of thin beds below tuning remains an important problem in the geophysics community that is often poorly understood and for which permanent solutions are still to be found.

Introduction

Defining resolution

The limits of seismic resolution is an important factor to consider in any exploration or development project. One of the most commonly used limits to seismic resolution was established by Widess (1973), who defined the resolving power to be $\lambda/8$ for noise-free data, but with a more practical limit of $\lambda/4$ for noise-contaminated data.

Widess (1973) calculated the effects of bed thickness by examining the interference pattern on relatively broadband wavelets reflecting off a simple wedge model. Using what appears to be a Morlet wavelet with center period λ, he noted that as the bed thickness h approach $\lambda/4$ the wavelets experience maximum positive interference, while at $\lambda/8$ they experience maximum destructive interference. After this point, Widess (1973) states that “the character of the reflections is indistinguishable for beds whose thickness is less than about $\lambda/8$. For this reason, it is appropriate to define a thin bed as one whose thickness is less than about $\lambda/8$”. With the advent of spectral decomposition and the analysis and interpretation of frequency and phase, it became clear that the assertion of $\lambda/8$ as the lower limit for seismic resolution was incomplete (Chung and Lawton, 1995; Chopra et al.,2006).

One of the first studies analyzing changes of peak frequencies in thinning beds was conducted by Chung and Lawton (1995). Using Ricker wavelets, they generalized Widess’ (1973) wedge to represent four fundamentally different two-term reflectivity models summarized in Appendix A, one of which is the Widess model. They show that the calculated peak frequency does not occur when the bed thickness is equal to $\lambda/8$, as predicted by Widess (1973), but that $\lambda/8$ is actually the limiting value for the peak frequency as the bed thickness approaches zero. For all reflectivity models but one, the Widess model, as the bed thickness approaches zero, the peak frequency approaches the values of the peak frequency of the source wavelet. These findings provide the mathematical basis to further understand the behavior of seismic wave interference in thin beds.

Tirado (2004) evaluated the limits of seismic resolution for sands in Louisiana through the use of spectral decomposition. She utilized the peak frequency estimates from Chung and Lawton (1995) to find its relationship with sand thickness and found that peak frequencies continue to vary as the sand layer thickness decreases not only below the tuning frequency, but also below the $\lambda/8$ limit. She noted that every reflectivity pair can be represented as the sum of an even and an odd component. She then shows that each one of the components presents a different evolution of peak frequency values as the sand thickness decreases.

Several authors have extended Tirado's (2004) concept to further improve the seismic resolution limit in different cases (Portniaguine and Castagna, 2004, 2005; Chopra et al., 2006; Puryear and Castagna, 2008; Chopra et al., 2009;). Chopra et al. (2006) showed that when the top and the base reflectivity coefficients of a layer are not exactly equal and opposite, as in the Widess (1973) model, the peak frequency decreases with thickness even below $\lambda/8$. Since there are changes of seismic amplitude and frequency below the conventional limit established by Widess (1973), thicknesses below the tuning limits can also be inferred. Note that such an extension of the limits of seismic resolution is based on the validity of a two-reflector model accurately representing the geology.

Sinha et al. (2005) used continuous wavelet transforms (CWTs) to generate time-frequency spectra that are useful in mapping anomalous attenuation as well as tuning effects. The CWT transform uses a suite of wavelets whose bandwidth changes with the scale (or center frequency) resulting in shorter wavelets at higher frequencies and longer wavelets at lower frequencies. The original data can be reconstructed by convolving the same wavelets with the decomposed data and summing.

Improving resolution

The simplest and earliest technique to improving resolution is spectral balancing. Spectral balancing is routinely applied in seismic processing as the objective function in deconvolution (Yilmaz, 2001). A common workflow is to use spiking deconvolution to flatten the entire spectrum (beyond the useable frequencies) and then follow it with a bandpass filter. An approach that is useful for interpreters is to decompose the seismic data using spectral decomposition, spectrally balance (or "flatten") the spectral components and then reconstruct the data using the original CWT wavelets. While spectral balancing enhances the lower magnitude spectral components in the data, it does not attempt to extend the spectrum beyond that measured.

Smith et al. (2008) generalized this method by reconstructing the data using octaves of the original wavelets in the inverse transform in addition to those used in the forward transform, thereby "extending" the bandwidth. The magnitude of the octaves was set to be a finite value while the phase was then kept consistent with the corresponding measured, lower-frequency components (Wei et al., 2019). Such bandwidth extension capabilities are provided by several technology companies, but the details of the algorithm implementation are proprietary. Smith et al. (2008) advise that users of these products should "trust but verify" using impedance logs. First, the interpreter extracts a wavelet, generates a synthetic, and computes a correlation coefficient. If the wavelet generated from the bandwidth extended volume results in synthetics that exhibit a higher correlation coefficient, the bandwidth extension is improving resolution; in contrast, if the correlation is less, the assumptions used in the algorithm are not valid and the results should be discarded. They show excellent results for both prestack gathers and poststack data.

In an attempt to understand this process, Matos and Marfurt (2011) built on Mallat and Hwang's (1992) concept of Maximum Modulus Lines (MML). Mallat and Hwang (1992) found that the original seismic data can be approximated by using only the wavelets at the peak locations (MML) of the CWT magnitude spectra. Matos and Marfurt (2011) then mimicked Smith et al. (2008) and reconstructed the data using broader bandwidth wavelets than used in the forward transform. They found significantly improved resolution in a Barnett Shale play with dozens of wells used for control.

Mallat and Hwang (1992) also found that the Hölder exponent (a measured of the magnitude spectra's change with frequency) can be used to differentiate smooth from abrupt discontinuities. Li and Liner (2008) took this idea to its next logical conclusion by computing a seismic attribute based on the Lipschitz exponent, called the SPICE algorithm (Smythe et al., 2004). The basis for such a seismic attribute computation is that the Lipschitz exponents can be linked to acoustic impedance contrasts computed from seismic data. The algorithm they implemented is capable of recovering the correct Lipschitz exponent from different signal singularities and shows an interesting approach to mathematically characterize seismic discontinuities and structural features in seismic data. While the authors do not claim that this algorithm improves resolution, they do find that it better quantifies the types of discontinuities in the subsurface.

Puryear and Castagna (2008) used the physical principle of decomposing the seismic signal into even and odd components to develop a spectral inversion algorithm and determine layer thickness below tuning. They define this model as a "generalized reflectivity model" and show that the improvement in resolution results from the constructive interference of the even component as model thickness approaches zero. Then, knowing that the spacing between peaks and notches in the spectral components is a deterministic function of layer thickness between the two reflections, they invert for reflectivity.

In this paper, I evaluate three of the above methods that in some way attempt to either extend or quantify the resolving problem of the recorded seismic data. I begin with Chung and Lawton's (1995) three wedge model classes to test the alternative algorithms. I then review the assumptions of each of the three methods and evaluate their effectiveness on the wedge models. After this analysis, I apply the some of these algorithms to real seismic data from the Diamond-M field in Texas and compare the seismic-to-well ties before and after application.

Methodology

Wedge models

I illustrate the limits of resolution using a simple wedge model (Figure 43a). I created three wedges based on the types defined by Chung and Lawton (1995) and further developed by Tirado (2004), Portniaguine and Castagna (2004 and 2005), Chopra et al. (2006), Puryear and Castagna (2008); and Chopra et al. (2009). The top wedge exhibits Type III (Appendix A), the middle wedge a Type II and the bottom wedge a Type I coefficient pairs that represent the mixed, even and odd components, respectively.

The two-way traveltime thickness h of all three wedges ranges from 0 to 60 ms. A Ricker wavelet with a peak frequency of 30 Hz was used to create the models (Figure 43a and Figure 43b), which generates a one-quarter-wavelength tuning thickness at approximately $h = 8.25$ ms. The top of each wedge is at *60* ms (top), *180* ms (middle) and *300* ms (bottom). Figure 43d shows the amplitude spectrum of the three wedges averaged over the entire line. Its spiky nature is attributed to the wavelet interference pattern that gives rise to tuning thicknesses and frequencies of the six reflectors.

Since seismic volumes are commonly contaminated by different types and levels of noise, I generated another set of wedge models with *20%* random noise added to test the sensitivity of the algorithms reviewed in this paper to it. Figure 44a shows the wedge models from Figure 43 with *20%* random noise added. The wedges are displayed as wiggle traces to highlight the effects of the random noise more clearly on the top and bottom of each wedge. The same wavelet was used in the generation of the wavelets, as can be observed in Figure 44b and Figure 44c. The amplitude spectrum from Figure 44d is very similar to the one displayed in Figure 43d, with the difference of the base amplitude level, which is evident for very low frequencies (below *10* Hz) and high frequencies (above *70* Hz).

Spectral balancing

A collection of seismograms is said to be spectrally balanced if they have been filtered in such a way that they exhibit the nearly constant amplitude spectrum (Tufekčić et al, 1981). One common way to accomplish spectral balancing is by deconvolution followed by band-pass filtering, with the result that the balanced traces have the spectrum of the band-pass filter (Tufekčić et al, 1981).

Unlike bandwidth extension, if a given spectral component is not recorded in the original acquisition, it will not be restored with spectral balancing. The objective of spectral balancing is to flatten the seismic spectrum and, in this way, extend the usable bandwidth of the data and improve seismic resolution (Marfurt, 2018).

For my implementation of spectral balancing, I follow the algorithm presented by Marfurt (2018):

- Compute the power of $P_j(t,f)$ the j^{th} trace as the square of the magnitude component $D_j(t,f)$:

$$P_j(t, f) = D_j^2(t, f) . \qquad (1)$$

- Average this spectral power over all traces $j = 1, 2\ldots, J$ in the survey a $2K+1$ samples vertical analysis window to obtain the average power for each time slice t:

$$P_{avg}(t,\mathrm{f}) = \frac{1}{J(2K+1)} \sum_{k=-K}^{+K} \sum_{j=1}^{J} P(t + k\Delta t, f) . \qquad (2)$$

- Calculate the peak of the average power at time t:

$$P_{peak}(t) = MAX_f \left[P_{avg}(t, f) \right] . \qquad (3)$$

- Define a pre-whitening value of $\varepsilon=0.01$ (or 1%) and calculate the flattened magnitude spectrum $D_j^{flat}(t,f)$ as:

$$D_j^{flat}(t, f) = \left[\frac{P_{peak}(t)}{P_{avg}(t, f) + \varepsilon P_{peak}(t)} \right]^{1/2} D_j(t, f) , \qquad (4)$$

where the ε value represents a noise threshold for the data. With this computation, I can enhance the spectral components associated with the signal of interest while diminishing the contribution of noise to the final output. It follows that this technique has limited application in the presence of highly contaminated data with noise of epsilon values $\varepsilon \geq 50\%$ or in the abundance of bad traces, as the average will only increase the influence of noise in the final result.

Continuous Wavelet Transform (CWT) Bandwidth Extension

I decompose the three wedge models into their spectral components through the implementation of a Continuous Wavelet Transform (see Appendix B) to evaluate the feasibility of increasing the seismic resolution by using this technology.

I define the bandwidth f_B of a signal as conventionally done by the signal analysis community, as the spectral distance between the two half-power points of the spectrum of a signal which for a Morlet wavelet is:

$$f_B = 2\sqrt{\ln(2)}\sigma_f \, , \tag{5}$$

where σ_f is the standard deviation of the original Morlet wavelet.

During the data reconstruction phase of the Continuous Wavelet Transform, the same wavelet need not be used to reconstruct the original data (Liner, 2010). In my application, I can choose to replace the original wavelets with a broader-band version of themselves during the reconstruction, resulting in bandwidth extension to both higher and lower frequencies (Smith et al., 2008; de Matos and Marfurt., 2011; Marfurt, 2018). Bandwidth extension can be performed if the underlying assumption that the Maxima Modulus Lines (MML) or ridges of the original CWT components accurately represent the major impedance changes in the subsurface (see Appendix C) (Marfurt, 2018; Li and Liner, 2008, Matos et al., 2011).

Hölder exponent

Li and Liner (2008) developed a method to detect singularities in acoustic impedance profiles from seismic reflection data through the utilization of amplitude, phase and frequency integration in what they term the "Hölder" attribute. They calculate the Hölder exponent from the seismic spectral components and use it to characterize singularities from the signal.

In this paper, I follow their approach to calculate the Hölder exponent for every sample in the wedge models and determine whether this technology can be utilized to improve seismic resolution on amplitude volumes.

Li and Liner (2008) build upon the of Mallat and Hwang's (1992) Maximum Modulus Lines (Appendix C) to demonstrate that their algorithm can recover the Hölder exponent (see Appendix D) from singular points in the seismic data. The Hölder exponent can be computed due to the fact that MML in time-scale space tend to be linear directly above singular points. Thus, on a time-scale space, by plotting all the Maxima Modulus Points, the Hölder exponent can be recovered from the slope of the expression (Mallat and Hwang, 1992):

$$\log_2 \left| X_{CWT} \right|^2 \leq \log_2 C + (2\alpha + 1) \log_2 \sigma \, , \tag{6}$$

where X_{CWT} is the magnitude of the spectral components computed from the Continuous Wavelet Transform (CWT), α is the Hölder exponent, C is a constant, and σ is the scale of the transform. Li and Liner (2008) show the usefulness of their algorithm by computing a Hölder attribute, which they apply to the Marmousi2 (Martin, 2004) model to detect singularities within the volume. The Hölder exponent provides a means to further characterize the seismic data and is shown to be sensitive to small transitions within the acoustic volume which could go undetected otherwise (Li and Liner, 2008).

For my implementation, the slope of equation 6 defines what I refer to as "Hölder" exponent attribute in this paper. I expect a spike in the acoustic impedance to define a flat magnitude spectrum, therefore producing a "Hölder" value of "0". For a decrease in the magnitude spectrum, I expect a negative "Hölder" exponent while for an increase in magnitude with high frequencies, which I would expect to occur at thin beds, I expect a positive "Hölder" exponent.

Results and discussions

We tested these three algorithms on a data set acquired over the Diamond M field in the Midland Basin, Scurry County, TX. The available seismic volume encompasses carbonate and dolomitic formations of Wolfcampian and Leonardian age mostly, belonging to the San Andres, Glorieta and Clearfork formations (Caf, 2015).

Figure 45a shows a representative vertical cross section of the field through seismic amplitude. Arrows indicate different geological features recognized in it by previous authors. Near the top of the dataset, strong acquisition footprint, indicated by the blue arrow, strongly contaminates the first 200 ms of reflection data. Clinoforms belonging to the Clearfork formation are indicated by the orange arrow. Wolfcampian rocks underlie the Clearfork formation and are recognized by the relatively flat and low amplitude reflectors below the clinoforms from the Clearfork formation, as indicated by the red arrow. A statistical wavelet (Figure 45b) was extracted from the interval corresponding to the Clearfork and Wolfcampian formations, from *500* ms to *900* ms in depth, with its corresponding frequency spectrum displayed in Figure 45c. The amplitude spectrum of the entire seismic volume within the aforementioned interval is displayed on Figure 45d. Dominant frequencies of up to 60 Hz define a one-quarter-wavelength tuning thickness of approximately $h = 4$ ms.

Continuous Wavelet Transform (CWT) bandwidth extension

Figure 46 through Figure 49 show the different parts of the spectral components for the wedge models shown in Figure 43: the spectral magnitude (Figure 46), spectral ridges (Figure 47), spectral voices (Figure 48) and spectral phase (Figure 49). As expected, higher frequency components delineate the top and bottom of the wedges more clearly.

Patterns of tuning are observed in all wedges, with the onset thickness of tuning starting at lower thicknesses for the even component. Marfurt and Kirlin (2001) predicted this behavior by analyzing the amplitude of thin bed reflections for a Type I wedge, showing that both odd and even components of the wedge will reach amplitude maxima with a phase shift at periodic intervals (Figure 46).

Figure 46 shows three spectral magnitude components of all three wedges at a low (20 Hz), a medium (40 Hz) and a high (80 Hz) frequency. Pockets of high amplitude are highlighted by red ellipses in Figure 46b and Figure 46c. As predicted by Marfurt and Kirlin (2001), these tuning frequencies repeat with the same period for all components. I also note that such tuning thicknesses shift towards lower values as frequencies increases. Both the odd component (bottom wedge) and the mixed component (top wedge) exhibit the same tuning pattern, which is to be expected since the mixed component is predominantly odd. These tuning effects prove to be a challenge for the ridge determination, as we can see in the next figure.

Figure 47 shows the spectral ridges as calculated from equations C1 and C2 (Appendix C). On a tuning free model, one would expect the ridges to be located at the exact location of local maxima in the frequency magnitude domain, therefore delineating the wedges at the proper location of their tops and bottoms. However, in the presence of interference patterns, the location of the ridges becomes inaccurate for low-to-mid range frequencies. Red ellipses are located in the same place as in Figure 46 for identification of tuning thicknesses. Blue lines show the location of the wedge top and bottom, to indicate misplacement of reflections in places where black ridges do not follow the blue lines, delineating the extent of the wedges. The orange arrow indicates a wedge thickness miscalculation derived from the algorithm picking the wavelet's side lobes due to destructive interference canceling the amplitude of the main lobe. Near the tuning frequency, the two wavelets constructively interfere to form a single, stronger wavelet. However, the peak of magnitude of this wavelet falls in the middle of the wedge. Overall, higher frequency ranges better delineate the top and bottom of the wedge, however, such high frequencies are not always recorded by seismic methods in the first place.

Figure 48 shows the voice components for the spectra shown in Figure 46. The high amplitude side lobes in all frequency components give rise to extra MML or ridges in Figure 47.

Figure 49 shows the spectral phases co-rendered with spectral magnitudes against an opacity-variant monochrome gray color map. Areas of high magnitude (i.e. tuning thicknesses) show transparent, while areas with low spectral magnitudes, appear opaque. The phase distribution shows that, in the presence of tuning frequencies, no phase unwrapping takes place, which would be necessary for a proper reconstruction of a higher resolution form of the data.

Figure 50 shows the reconstructed wedges using the bandwidth extended wavelet family displayed in Figure 62. As predicted from ridges in Figure 47, interference patterns prevent the proper location of events in the reconstructed image, as indicated by orange arrow. Red arrow indicates the creation of a false event from tuning thicknesses interpreted as one combined effect, as red arrow indicates in Figure 47. Purple arrows indicate created false events from locations where the algorithm recognized side lobes as seismic events. The reconstruction is accurate and “higher resolution” for thicknesses above tuning. Figure 50b and Figure 50c display the extracted wavelet with its corresponding magnitude spectrum. Note the increased magnitude for both low and high frequencies, which is also reflected on the amplitude spectrum for all three models depicted in Figure 50d.

Applying the bandwidth extension workflow on the seismic volume from Diamond M field in Figure 45a yields the results displayed in Figure 51a. Wavelet interference patterns generate the broken reflector image of some of the events displayed in the seismic. Figure 51b and Figure 51c display the extracted wavelet with its corresponding magnitude spectrum, respectively. Figure 51d shows the amplitude spectrum for the entire line.

The results show that the current implementation of bandwidth extension does not improve resolution, as can be verified by the ridge misplacing in Figure 47 and the wedge results on Figure 50a. The results of this implementation are cosmetic, with moderately well separated reflectors appearing sharper. But below tuning it does not improve resolution.

Spectral balancing

Figure 52a shows the simple wedges model reconstructed after spectral balancing using the same wavelet family utilized for its decomposition (Figure 61). Small side lobes can be observed at the different interfaces, which can also be explained by looking at the shape of the extracted wavelet in Figure 52b. When compared with Figure 43c, the magnitude spectrum of the extracted wavelet from the reconstructed data has increased high frequencies, which is also evident in Figure 52d. Some low amplitude side lobes appear in the extracted wavelet, as a consequence of the higher frequency content after spectral balancing.

I obtain similar results when comparing Figure 53 to Figure 44. The random noise in the wavelets in Figure 44a is corrected after spectral balancing, at the cost of low amplitude ringing on the side lobes (Figure 53b). The magnitude spectrum of the frequencies in Figure 53c is significantly increased for high frequencies and slightly for low frequencies. High frequency noise can be exacerbated in spectral balancing, as can be observed in the high frequency range (> *80* Hz) of Figure 53d, when compared with Figure 44d.

I apply spectral balancing to the Diamond M field shown in Figure 45a on Figure 54a. The spectral balancing has a smoothing effect on both the extracted wavelet and magnitude spectrum displayed on Figure 54b and Figure 54c respectively. Such smoothing attenuates the acquisition footprint effect at the top of the vertical cross section, as indicated by the blue arrow. Spectral balancing also subtly highlights some of the higher frequency events, as indicated by the orange arrows.

Hölder exponent

Li and Liner (2008) find that the Hölder exponent exhibits the transitional character of waves recorded in seismic data. They also show the expected Hölder exponent for five different kinds of singularities. Equation 6 shows that in the logarithmic time-scale space, the Hölder exponent can be recovered from the slope of least square fitting the squared magnitudes and scales. Therefore, the Hölder exponent shows the evolution of magnitudes across scales for any given time in every trace. A Hölder exponent value of $\alpha = 0$ corresponds to a constant magnitude spectrum, as we expect from an isolated reflector separating two constant impedance layers. For increasing spectral magnitudes, I expect positive values for the Hölder exponent, with higher numbers associated with potential exploration or development targets, such as small channel infills, or with tuning effects represented by the Widess model. Decreasing spectral magnitudes corresponds to gradients in the impedance.

Figure 55 and Figure 56 show the Hölder exponent attribute computed for the a modeled acoustic impedance profile and the wedge models from Figure 43. Since the derivation of the Hölder exponent stems from a time-scale space, it is natural that it resembles the spectral component in distribution of high and low values. In Figure 55a I generate a simple acoustic impedance profile showing five distinct events and characterize their Hölder exponent response: at 200 ms a sharp positive change in acoustic impedance; at 300 ms a layer with a grading velocity increase and at 400 ms a layer with a grading velocity decrease; at 500 ms and 600 ms two thin layers with a positive and a negative acoustic impedance contrast, respectively. I convolve this model with an Ormsby wavelet ($f_1=5$ *Hz,* $f_2=10$ *Hz,* $f_3= 60$ *Hz* and $f_4=70$ *Hz*) in **Figure 55**b, from which I compute its corresponding Hölder exponent response in **Figure 55**c. As expected, I observe a sharp increase in the Hölder exponent for both thin beds, and a low, negative response for the velocity gradients.

In **Figure 56** I compute the Hölder exponent for the wedges generated in **Figure 43.** I observe high values in most of the inner portion of the wedges, with the highest values of $\alpha \geq 2$ on the locations of tuning thicknesses, as displayed on Figure 46, indicated by the red arrow. The transitional character of the outside of the wedges is delineated by Hölder exponent values of $\alpha = -1$. I observe the lowest negative values for the Hölder exponent of $\alpha \leq -2$ in places outside the wedges where sidelobe interference causes lower magnitude across higher frequencies, indicated by the blue arrow. I selected a discrete color bar to better highlight different types of singularities that the attribute is sensitive to.

Figure 57 displays an extracted Hölder exponent attribute trace at the location of a well in the Diamond M field. The acoustic impedance is calculated from available sonic P-wave and bulk density logs, which are also used to compute a synthetic trace for the range of *400-900* ms corresponding with the with Clearfork and Wolfcampian formations. Yellow arrows indicate locations of "M" shaped functions that correspond to sharp changes in the acoustic impedance. Local high values of the attribute, as indicated by orange arrow, may indicate potential zones of interest, as they reveal an increasing magnitude with frequency components that may be associated to potential targets.

Figure 58a displays a cross section through seismic amplitude of the Diamond M field shown on Figure 45; Figure 58b through the computed Hölder exponent attribute and Figure 58c shows a correndering of Figure 58a and Figure 58b. Blue arrow indicates the attribute response to acquisition footprint noise, as a high, negative value. Orange arrow indicates a high Hölder exponent value for a zone unnoticed in the amplitude section that could correspond to a potential exploration or development target, due to the high energy associated to it. Purple arrow indicates the attribute response to the relatively low energy Wolfcampian formation below the Leonardian clinoforms.

Overall, this attribute, as stated by Li and Liner (2008) shows promising results in improving current seismic interpretation workflows, providing an additional tool for interpreting potential features of interest for exploration or production. I find that it shows the evolution of spectral magnitudes across all frequency components, which might highlight regions in the seismic survey where potential targets could hide. However, for thin bed resolution purposes, it does not improve on what spectral decomposition techniques can highlight.

Seismic well-ties

One of the biggest limitations for applying bandwidth extension is the underlying assumption of the sparse spike model. Smith et al., (2008) recommend correlating bandwidth extension output with vertical well logs. If the resulting well tie correlation is improved, then the underlying assumption is partially validated.

In this project, to verify the results obtained from spectral balancing and bandwidth extension, I applied a seismic well-tie with one well available within the Diamond M field, for the range of *400-900* ms corresponding with the with Clearfork and Wolfcampian formations. Figure 59a displays the result of the seismic well-tie with the original amplitude volume for the Diamond M field, while Figure 59b does so for the spectrally balanced output. Figure 59c displays the result of the seismic well-tie with the bandwidth extended output. With a slightly improved correlation coefficient, the workflow for spectrally balancing seismic volumes is validated for this survey, while also improving the overall quality of the image. However, no significant change is demonstrated for the seismic resolution, which remains the same before and after the poststack filers applied. Erroneous computation of wedges during the reconstruction phase of the bandwidth extension output lead to a decreased correlation coefficient, thus corroborating its inability to resolve layer thicknesses below tuning.

Discussion

Seismic vertical resolution below tuning thicknesses remains a very important, yet not completely understood, problem within the geosciences. Complex interference patterns prevent correctly imaging reflectors below tuning thicknesses. Phase unraveling is, perhaps, the most challenging problem to resolve.

The Continuous Wavelet Transform, coupled with spectral balancing, provides a tool for qualitatively improving the seismic image of reflectors, highlighting both higher and lower frequency components often used for the creation of background models in acoustic inversion workflows, among others. However, from the results of my application into both real and synthetic data, this coupled workflow does not improve on the original vertical resolution of seismic volumes. It only slightly improves seismic-to-well ties.

The Hölder exponent attribute provides a framework for better interpreting seismic volumes, through the understanding of the transitional character of acoustic impedance changes in seismic volumes. The Hölder exponent does not improve the vertical resolution but it can highlight potential exploration or development targets that could go unnoticed otherwise.

Conclusions

Widess’ (1973) model for thin bed resolution provides a good baseline for understanding the limits of conventionally acquired seismic volumes for both land and marine data. However, it does not account for a majority of the cases encountered in most exploration and production campaigns. Therefore, a more generalized model is necessary. Decomposing the seismic reflectivity of a thin bed into an even and an odd component allows me to retrieve more information from the seismic volume, as I now know that the even component contains variations in amplitude and frequency below tuning thickness, thus enabling the user to extract useful information below what is conventionally accepted.

Of the three methods evaluated in the current paper, the Continuous Wavelet Transform (CWT) Bandwidth Extension provides cosmetic improvements that may aid horizon interpretation in exploration and production endeavors, but does not improve the seismic resolution. Phase interference patterns below tuning thicknesses provide CWT magnitude peaks, and hence Maximum Modulus Lines (MML) that fall between the top and bottom of a thin bed. Increasing the bandwidth provides an erroneously placed, superficially higher resolution event

The Hölder exponent seismic attribute provides a means for further characterizing the impedance profile that gives rise to the seismic data. Although the Holder exponent may provide a means to discriminate between upper fining, upper coarsening, and simple blocky impedance patterns, it does not provide means for increasing seismic resolution below the tuning thicknesses.

Acknowledgments

The author would like to thank CGG Veritas for the access to Hampson-Russel licenses used in the development of this project. I would also like to thank friends and colleagues for the support and help provided for interpretation and generation of results, most especially to David Lubo and Abidin Caf.

Appendix A

Reflectivity decomposition

Chung and Lawton (1995) defined four fundamentally different types of two term reflectivity series, in contrast to that which was previously described by Widess (1973) (Figure 60). The first, Type I, has two reflectivity terms of opposite polarity and equal magnitude, in principle equal to the one defined by Widess some twenty years before; the Type II, had reflectors of equal polarity and magnitude. Type III, had opposite polarity and unequal magnitude. Finally, Type IV had of reflectors with equal polarity and unequal magnitude.

Several other authors further developed this concept to decompose such reflectivity series into an odd and an even component (Tirado, 2004; Portniaguine and Castagna, 2004 and 2005; Chopra et al., 2006; Puryear and Castagna, 2008; and Chopra et al., 2009). According to Puryear and Castagna, 2008, a Type I reflectivity coefficient pair would be equal, in principle, to the odd component of a decomposition pair; Type II would be equivalent to the even component; and Type III to the mix or total component, i.e. the original two term reflectivity series.

Appendix B

The Continuous Wavelet Transform (CWT)

Frequency analysis constitutes a pivotal tool in signal analysis for a multitude of reasons. Perhaps the most common way to perform such an analysis is through the use of the Fourier Transform (Smith et al., 2008). Unfortunately, a direct implementation carries the loss of time resolution as a consequence (Liner, 2010).

Beginning in the 1970s and 80s seismic processors introduced "time-variant" analysis such as time variant deconvolution and time variant spectral balancing. In the latter application, one might apply Fourier techniques in overlapping *1* s windows. The Continuous Wavelet Transform (CWT) takes this notion to the logical endpoint, where the size of the temporal analysis window and the frequency resolution are directly coupled. The CWT has proven invaluable in not only decomposing signals into its constituent frequencies while preserving time resolution, but also in further mathematically characterizing singularities in the signal (Mallat and Hwang, 1992).

Following Liner (2010), I define the Continuous Wavelet Transform as:

$$\mathrm{G}(\mathrm{s},\mathrm{u}) = s^{p}\int_{-\infty}^{+\infty} g(t)\psi\left(\frac{t-u}{s}\right)\mathrm{dt}\,, \tag{B1}$$

where $\psi(t)$ is the analyzing wavelet, $g(t)$ is the time series being transformed to the wavelet domain in the form $G(s,u)$; "s" is a frequency scale variable, "p" a real normalization parameter and "u" a translation variable. This conversion is used routinely in geophysics and can also be applied in more than one dimension (Alali et al., 2018).

For the reconstruction of the original time series, the inverse CWT is given by:

$$g(\mathrm{t}) = \int_{-\infty}^{+\infty}\int_{-\infty}^{+\infty} \mathrm{G(s,u)}\psi^{'}(\frac{t-u}{s})\,\mathrm{dsdu}\ , \qquad \text{(B2)}$$

where the inverse analyzing wavelet *ψ’* need not be the same as the forward transform wavelet (Liner, 2010).

For the Continuous Wavelet Transform application, an appropriate function needs to be selected that meets the criteria of a wavelet. According to Mallat and Hwang (1992), the function *ψ(t)* is said to be a wavelet if and only if its Fourier transform *Ψ(ω)* satisfies:

$$\int_{0}^{+\infty} \frac{\left|\Psi(\omega)\right|^2}{\omega} d\omega = \int_{-\infty}^{0} \frac{\left|\Psi(\omega)\right|^2}{\omega} d\omega = C < +\infty\ , \qquad \text{(B3)}$$

which implies that

$$\int_{-\infty}^{+\infty} \psi(u)du = 0\,. \qquad \text{(B4)}$$

In other words, a function *ψ(t)* is called a “wavelet” if it has finite energy concentrated in time and satisfies certain well-established conditions.

For my current implementation I choose a Morlet wavelet for decomposing the seismic data into its spectral components. A classical definition of Morlet wavelets is (Tu and Hwang, 2005):

$$\psi(\mathrm{t}) = Ae^{-\frac{t^2}{2\sigma^2}}e^{i\omega_0 t}\ , \qquad \text{(B5)}$$

where σ is the standard deviation of a Gaussian distribution and ω is the angular frequency.

The Morlet wavelet is not a true wavelet in the strict sense that its integral is not zero. This problem is solved by the fact that for large enough ω_0, the integral of $\psi(t)$ is small enough to ensure that it can be used numerically as if it were a wavelet (Tu and Hwang, 2005).

To implement the Continuous Wavelet Transform, I define a wavelet family which will be convolved with the seismic signal for the creation of all the spectral components. A family of wavelet functions can be obtained from a basis (or "mother") wavelet $\psi_M(t)$ centered about time $t = 0$, by scaling it by a dilation factor "s" and shifting it by time "u" (AASPI CWT documentation?):

$$\psi(t,u,s) = \frac{1}{\sqrt{s}}\psi_{\mathrm{M}}\left(\frac{t-u}{s}\right), \tag{B6}$$

Using the scaling theorem, Mallat (2009) shows that if $\Psi(\omega)$ is the Fourier Transform of the wavelet $\psi(t)$, then:

$$\psi_M\left(\frac{t}{s}\right) = |s|\,\Psi(\omega), \tag{B7}$$

Equation B7 states that compressing the wavelet by increasing the scalar s will dilate its spectrum and the peak frequency will shift to a higher value. In contrast, dilating the wavelet by decreasing s will compress its spectrum, and the peak frequency will shift to a lower value. Equation B7 is the basis for computing a wavelet family: by varying the scaling factor s, one can represent broadband spectra. Additionally, the spectrum of each wavelet in the family maintains a constant ratio between its peak frequency and corresponding bandwidth (Figure 61). Figure 61 and Figure 62 represent wavelet families used for spectral decomposition and reconstruction of wedges models in Figure 43 and Figure 44. As stated before, the wavelet family used for the reconstruction of the signal need not be the same as the one used for the decomposition. In this case, the inverse

CWT is performed with a wavelet family for which each component has twice the bandwidth of its counterpart in the decomposition.

The peak frequency for a Morlet wavelet is defined as:

$$f = \frac{1}{2\pi s} \tag{B8}$$

Once a wavelet family is chosen, the continuous wavelet transform *G(u,s)* of a function g*(t)* at time *u* and scale *s* is defined as:

$$\mathrm{G}(u,s) = \int_{-\infty}^{+\infty} \mathrm{g}(t) \frac{1}{\sqrt{s}} \psi_{\mathrm{M}}^{*}\left(\frac{t-u}{s}\right) dt = d(t) * \psi(t,u,s), \tag{B9}$$

where the first superscript * indicates the complex conjugate and the second * indicates convolution.

Because the spectrum of *ψ(t,u,s)* resembles a band-pass filter, the CWT can also be interpreted as the application of a filter bank to the original data *g(t)*. In order to exactly reconstruct the original data, the values of *s* should be chosen to span the spectrum of the original seismic data.

Liner (2010) shows that the convolution shown in equation A9 can be implemented in the Fourier domain, where it becomes a simple complex multiplication. Goupillaud et al., (1984) showed that the natural sampling of the scale variables is logarithmic with base 2. The number of octaves determines the span of frequencies being analyzed, while the number of voices per octave determines the number of samples (scales) across this span (Liner, 2010). Voices are defined as the real part of these spectral components.

Appendix C

Maximum Moduli Lines (MML)

One of the most important properties of the Continuous Wavelet Transform is that it allows me to further characterize singularities in the original signal (Tu and Hwang, 2005). Once the seismic signal has been decomposed through the Continuous Wavelet Transform, local maxima in the spectral components can be utilized to further characterize the signal. One can think of these spectral components as the correlation coefficient of how much the original seismic trace resembles each one of the scale-variant wavelets of the wavelet family. When spectral components are plotted next to each other across different scales, their maxima form lines, which Mallat and Hwang (1992) call Maxima Modulus Lines (MML). Mallat and Hwang (1992) show that these Maxima Modulus Lines (MML) can be used to reconstruct most of the original signal and that they also converge to singularities of the original signal.

I use Mallat and Hwang's (1992) MML to decompose and reconstruct seismic data, defining the local maxima points as local ridges. The algorithm can be described as follows:

- Compute the magnitude of the spectral components as its absolute value,

$$\mathrm{A}(u,s) = \left|\mathrm{G}(\mathrm{u},s)\right|, \tag{C1}$$

- Define a ridge threshold to set a minimum value that needs to be exceeded for a sample to be considered a local maximum; this threshold can be reduced at subsequent iterations.
- Identify ridges near time *t* if

$$A(t-\Delta t,s) < A(t,s) > A(t+\Delta t,s)\,. \qquad \text{(C2)}$$

- Pass a parabola through samples at *(t-Δt)*, and *(t+Δt)* and compute its maximum to identify the ridge time, t_r.
- Distribute the magnitude of $A(t_r, s)$ to the two neighboring samples.

Appendix D

Hölder exponent

Another fundamental property of the wavelet transform is that it allows to characterize local regularity of the signals (Mallat and Hwang, 1992), which carries important information that can be utilized for seismic interpretation (Li and Liner, 2008). This regularity is often measured in mathematics from the Hölder (also called Lipschitz) exponent. Mallat and Hwang (1992) define the Hölder exponent as follows:

- Let n be a positive integer and $n \le \alpha \le n + 1$. A function $f(x)$ is said to be Lipschitz α, at X_0, if and only if there exist two constants A and $h_0 > 0$, and a polynomial of order n, $P_n(x)$, such that for $h < h_0$:

$$\left| f(x_0+h) - P_n(h) \right| \le A|h|^{\alpha}\,. \qquad \text{(D1)}$$

- The function $f(x)$ is uniformly Lipschitz α over the interval $]a, b[$, if and only if there exists a constant A and for any $x_0 \in]a, b[$ there exists a polynomial of order n, $P_n(h)$, such that equation A12 is satisfied if $x_0 + h \in]a, b[$.

Equation A10 shows that the Lipschitz regularity of a function is a measure of the differentiability of a function. In the words of Mallat and Hwang (1992) "If the Lipschitz regularity α of $f(x)$ satisfies $n < \alpha < n + 1$, then I know that $f(x)$ is n times differentiable at x_0 but its n^{th} derivative is singular at x_0 and α characterizes this singularity".

Several authors show that Maxima Modulus Lines in the spectral components of data can be utilized to characterize the singularities of the original signal (Mallat and Hwang, 1992; Tu and Mallat, 2005; Li and Liner, 2008). In order to show this relationship, Tu and Mallat (2005) first present the following theorem:

Let $x_0 \in (a,b)$ and let the n^{th} ($n > 0$) derivative of Re$[A(u,s)]$ and Im$[A(u,s)]$ be finite-deviations for each scale s. If a scale $s_0 > 0$ and constants C and B exist such that for $x \in (a,b)$ and $s<s_0,$ all the modulus maxima of $A(u,s)$ belong to a cone defined by

$$|x - x_0| \leq Cs, \tag{D2}$$

such that, at each modulus maxima (u, s) in the cone

$$A(u,s) \leq Bs^{\alpha}, \tag{D3}$$

then $f(x)$ is uniformly Lipschitz n at x when $x \neq x_0,$ and $f(x)$ is Lipschitz α at x_0 when $\alpha < n$ is a noninteger.

Thus, the Maxima Modulus Lines allow me to estimate the Lipschitz exponent of a singularity in a signal. Tu and Mallat (2005) show that the Lipschitz exponents can be numerically calculated as:

$$\log[\mathrm{A}(\mathrm{u},\mathrm{s})] \leq \log(\mathrm{B}) + \alpha \log(s)\,. \tag{D4}$$

By plotting the logarithmic distribution of the Modulus Maxima values of a CWT decomposition against the logarithm of the scale, it is possible to calculate the Lipschitz exponent of the singularity to which such lines are converging (Mallat and Hwang, 1992; Tu and Mallat, 2005).

References

Alali, A., G. Machado, and K. J. Marfurt, 2018, Attribute-assisted footprint suppression using a 2D continuous wavelet transform: Interpretation, **6**, no. 2, T457-T470. Doi: 10.1190/INT-2017-0175.1.

Caf, A., 2015, Seismic stratigraphic and quantitative interpretation of Leonardian reefal carbonates, eastern shelf of the Midland basin: insight into sea level effects, geomorphology and associated reservoir quality: M.S. thesis, University of Oklahoma.

Chopra, S., J. P. Castagna, and O. Portniaguine, 2006, Seismic resolution and thin-bed reflectivity inversion: Canadian Society of Exploration Geophysicists Recorder, **31**, 19-25.

Chopra, S., J. Castagna, and Y. Xu, 2009, Thin-bed reflectivity inversion and some applications: First Break, **27**, 17–24.

Chung, H., and D. C. Lawton, 1995, Frequency characteristics of seismic reflections from thin beds: Canadian Society of Exploration Geophysicists Recorder, **31**, 32-37.

de Matos, M. C., and K. J. Marfurt, 2011, Inverse continuous wavelet transform “deconvolution”: 81st Annual International Meeting, SEG, Expanded Abstracts, 1861–1865

Goupillaud, P. L., Grossmann, A. and Morlet, J., 1984, A simplified view of the cycle-octave and voice representations of seismic signals, 54th Ann. Internat. Mtg: Soc. of Expl. Geophys., Session: S1.7

Li, C., and C. Liner, 2008, Wavelet-based detection of singularities in acoustic impedances from surface seismic reflection data: Geophysics, 73, no. 1, V1–V9

Liner, C., 2010, An overview of wavelet transform concepts and applications: University of Houston, 1-17.

Mallat, S., and W. L. Hwang, 1992, Singularity Detection and Processing with Wavelets: IEEE Transactions on Information Theory, **38,** 617-643.

Mallat, S., 2009, A wavelet tour of signal processing, 3rd ed.: Academic Press.

Marfurt, K. J., 2018, Seismic attributes as the framework for data integration throughout the oilfield life cycle: Society of Exploration Geophysicists, Distinguish Instructor Series.

Marfurt, K. J., and R. L. Kirlin, 2001, Narrow-band spectral analysis and thin-bed tuning: Geophysics, **66**, 1274-1283.

Martin, G., 2004, The Marmousi2 model, elastic synthetic data, and an analysis of imaging and AVO in a structurally complex environment: M. S. thesis, University of Houston.

Portniaguine, O., and J. P. Castagna, 2004, Inverse spectral decomposition: 74th Annual International Meeting, SEG, Expanded Abstracts, 1786-1789.

———, 2005, Spectral inversion: 75th Annual International Meeting, SEG, Expanded Abstracts, 1638-1641

Puryear, C.I. and J. P. Castagna, 2008, Layer-thickness determination and stratigraphic interpretation using spectral inversion: theory and application: Geophysics, **73**, R37-R48.

Sinha, S., R. Routh, P. Anno, and J. Castagna, 2005, Spectral decomposition of seismic data with continuous-wavelet transform: Geophysics, **70**, no. 6, P19–P25.

Smith, M., G. Perry, J. Stein, A. Bertrand, and G. Yu, 2008, Extending seismic bandwidth using the continuous wavelet transform: First Break, **26**, 97-102.

Smythe, J., A. Gersztenkorn, B. Radovich, C. –F. Li, and C. L. Liner, 2004, Gulf of Mexico shelf framework interpretation using a bed-form attribute from spectral imaging: The Leading Edge, **23,** 921-926.

Tirado, S., 2004, Sand Thickness estimation using spectral decomposition: M. S. thesis, University of Oklahoma.

Tu, C. L., and W. L. Hwang, 2005, Analysis of singularities from modulus maxima of complex wavelets: IEEE Transactions on Information Theory, **51,** 1049-1062.

Tufekčić, D., J. F. Claerbout, and Z. Rašperić, 1981. Spectral balancing in the time domain: Geophysics, **46**, 1182–1188.

Yilmaz, O., 2001, Seismic data analysis: processing, inversion and interpretation of seismic data: Society of Exploration Geophysicists.

Wei, Q., S. Chen., L. Liu., and X. Li, 2019, Extending high and low frequencies by predicting harmonics and sub-harmonics: SEG Technical Program Expanded Abstracts, 4092-4096.

Widess, M., 1973, How thin is a thin bed?: Geophysics, **38**, 1176-1180.

Figures

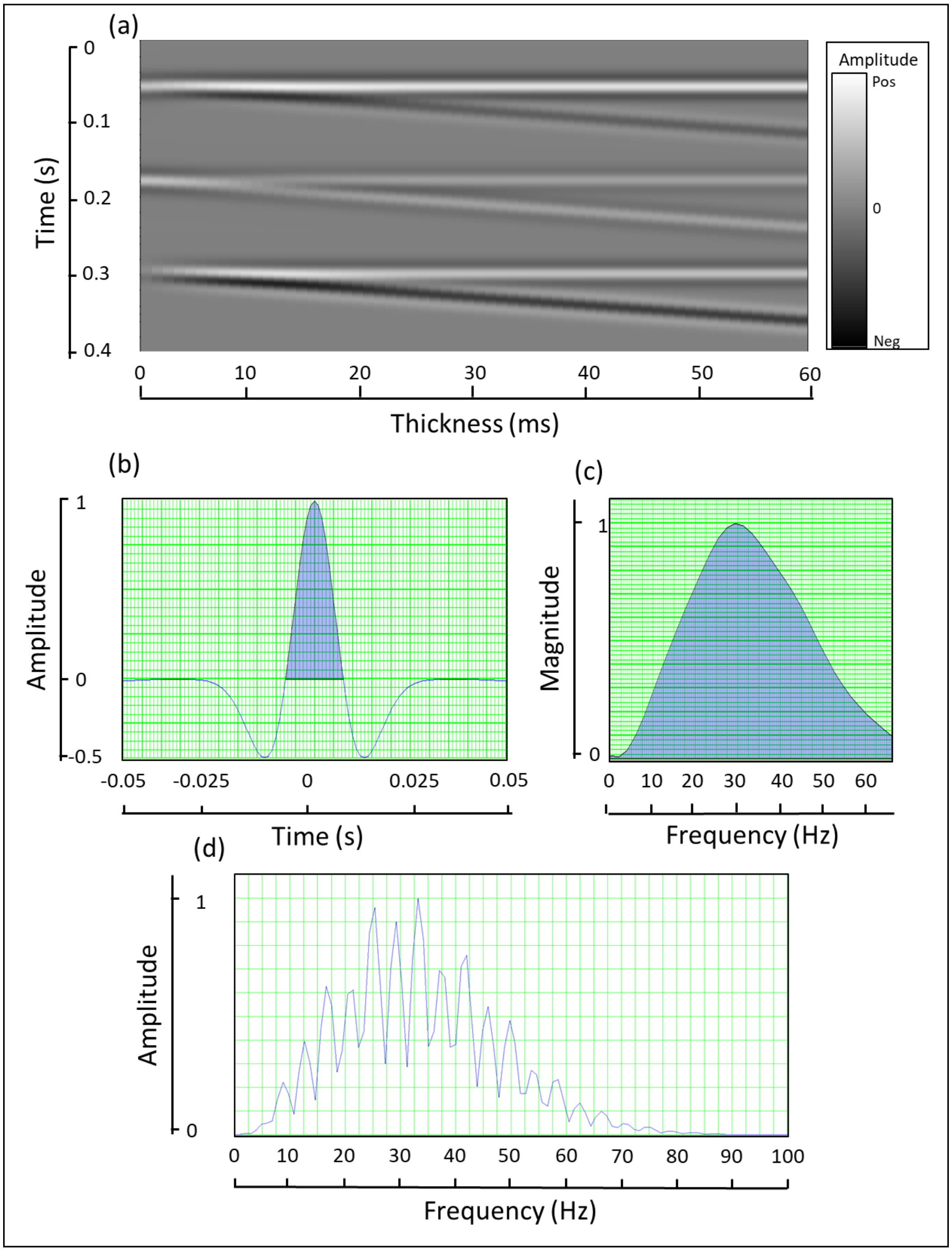

Figure 43. (a) Simple wedge models convolved with a (b) 30 Hz peak frequency Ricker wavelet and (c) its corresponding frequency spectrum. (Top of (a)) the Type III (Mix component); (middle of (a)) the Type II (even component); and (bottom of (a)) the Type I (odd component) wedges, according to Chung and Lawton (1995) and Chopra et al. (2006). (d) displays the amplitude spectrum of the wedges models averaged over the entire line. Peaks correspond to interference patterns generated from model interfaces.

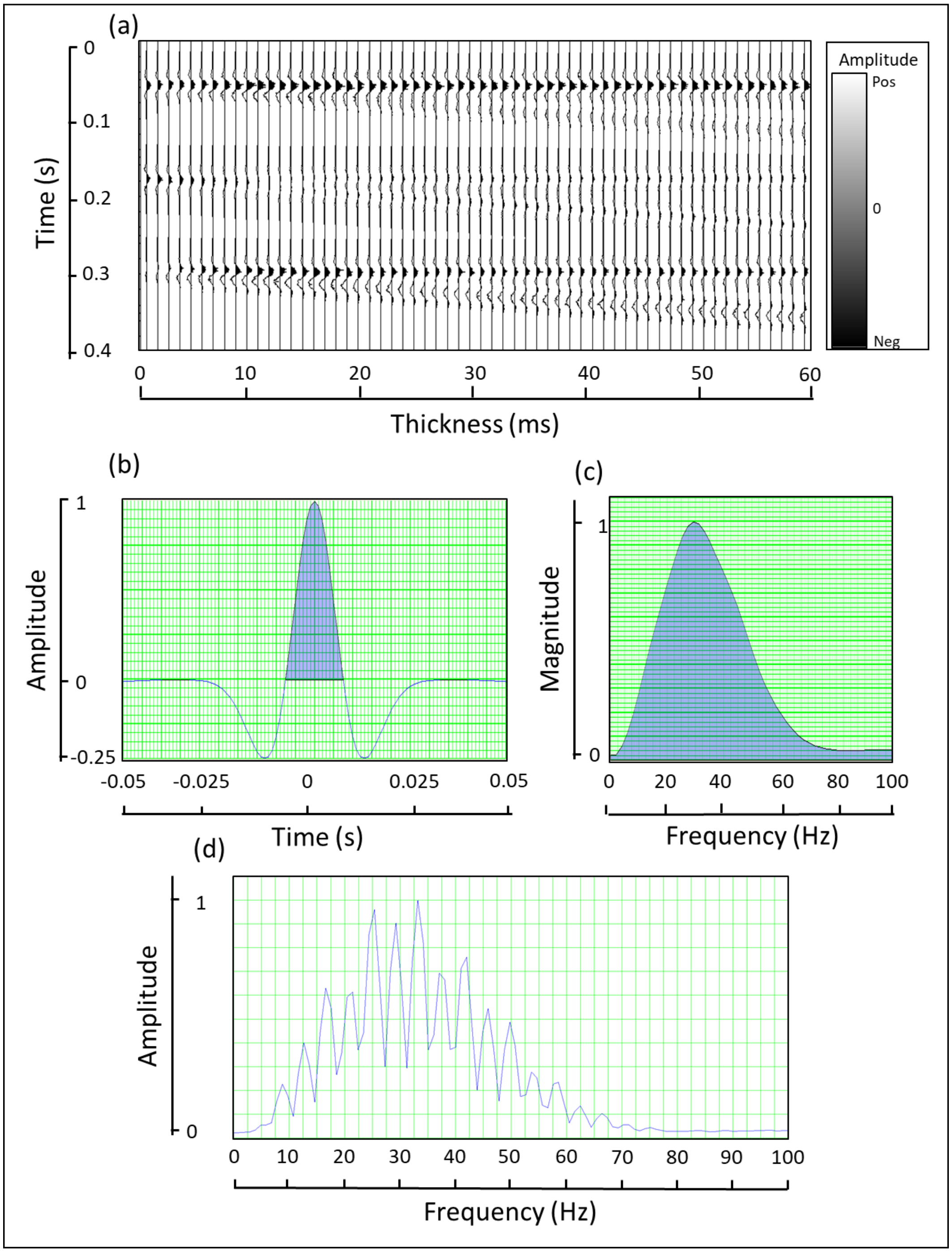

Figure 44. (a) Wiggle display of simple wedge models convolved with a (b) 30 Hz peak frequency Ricker wavelet and (c) its corresponding frequency spectrum. 20% random noise of the RMS amplitude of the entire line was added to the model. (Top of (a)) the Type III (Mix component); (middle of (a)) the Type II (even component); and (bottom of (a)) the Type I (odd component) wedges, according to Chung and Lawton (1995) and Chopra et al. (2006). (d) displays the amplitude spectrum of the wedges models averaged over the entire line. Peaks correspond to interference patterns generated from model interfaces.

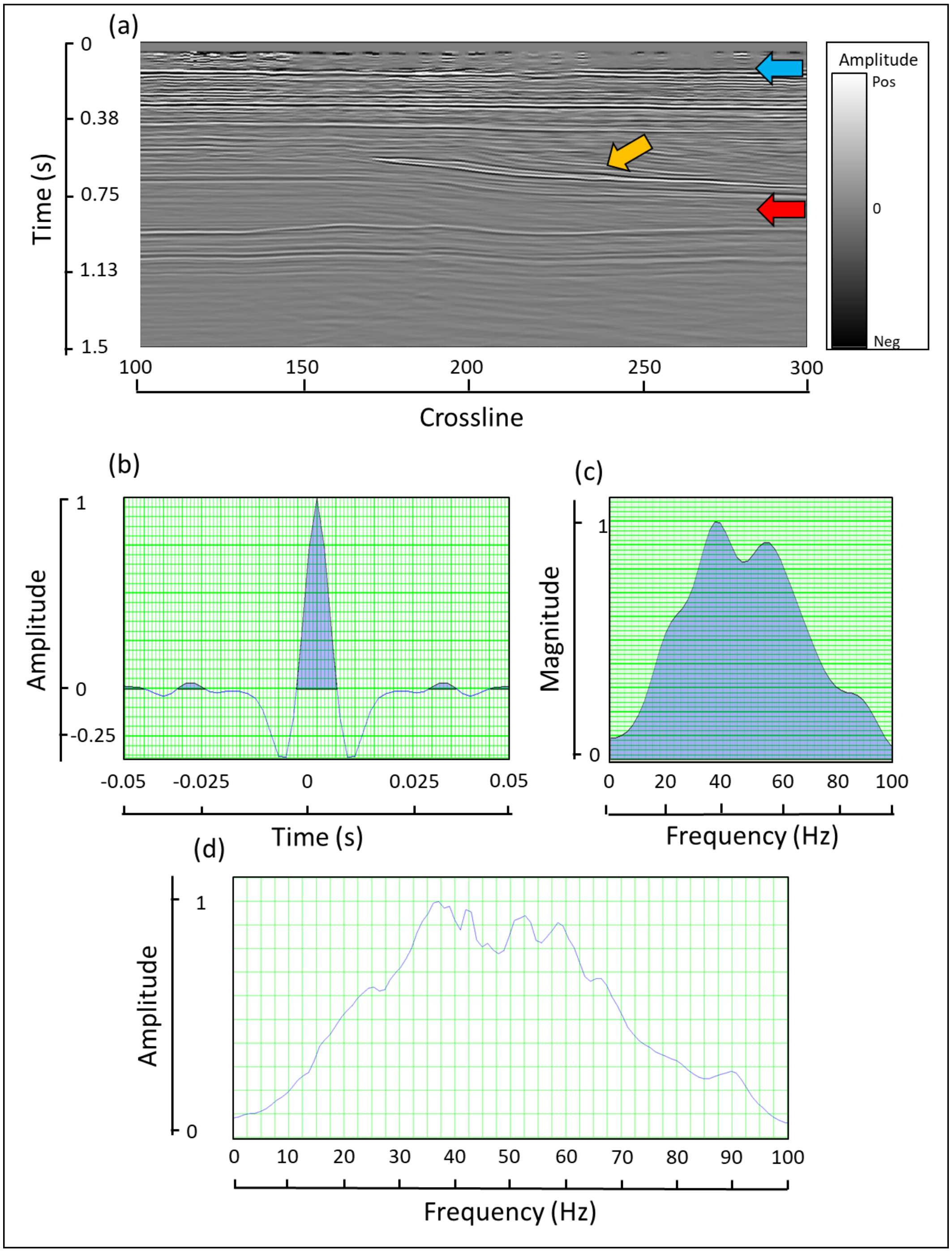

Figure 45. (a) Vertical cross section through seismic amplitude of the Diamond M field with (b) extracted wavelet in the 500-900 ms interval, approximately corresponding to the Clearfork and Wolfcampian formations, and (c) its corresponding frequency spectrum. (d) displays the amplitude spectrum of the entire volume for the aforementioned interval. Blue arrow indicates location of shallow acquisition footprint. Orange arrow indicates location of terminations from clinoforms of Clearfork formation. Red arrow indicates relatively flat and low amplitude reflectors from Wolfcampian formation.

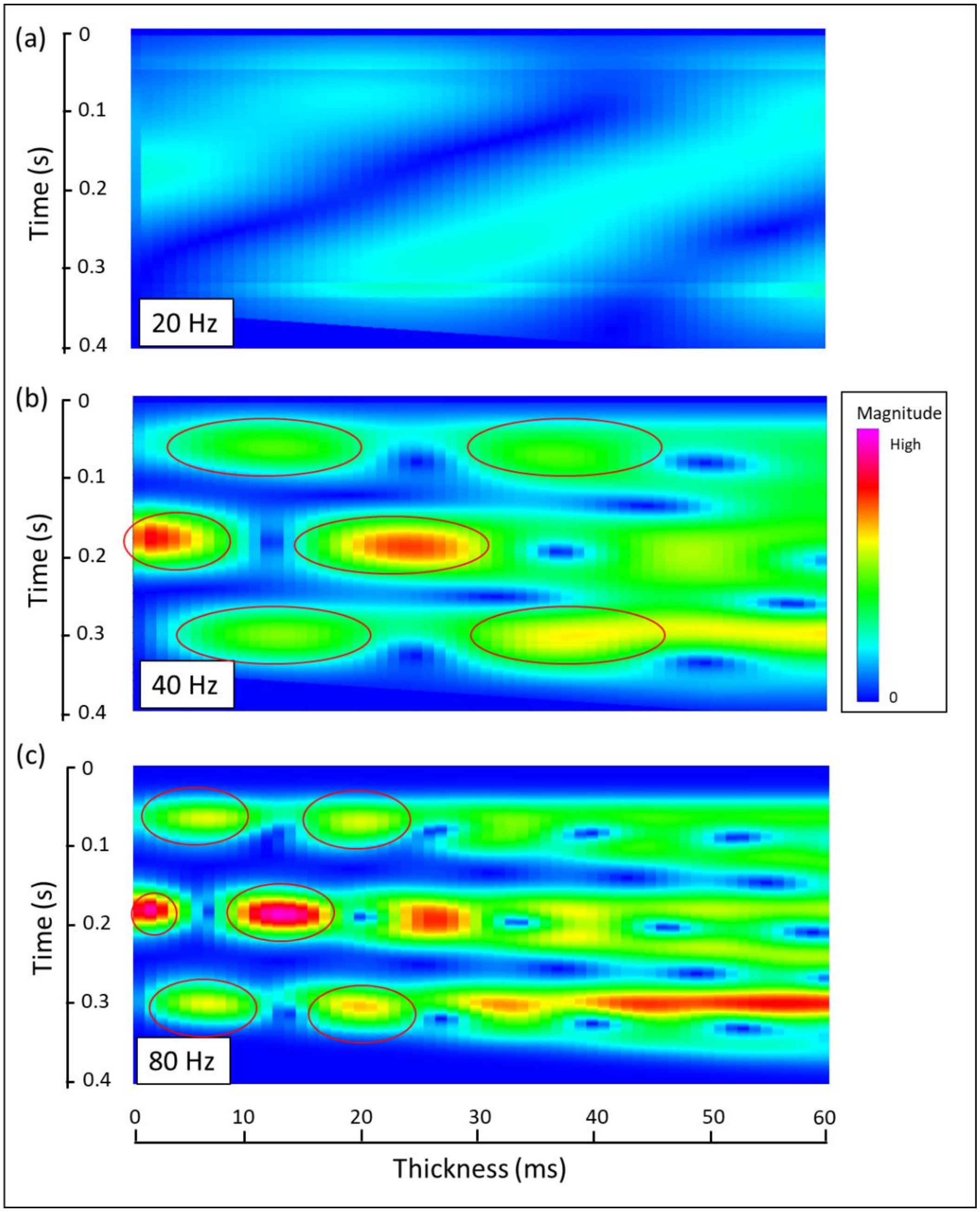

Figure 46. Spectral magnitude components A(t, f) for wedge models in **Figure 43** for (a) the 20 Hz component, (b) the 40 Hz component, and (c) the 80 Hz component. Red ellipses indicate tuning amplitudes where resolution of events becomes challenging. Note that, as predicted by Marfurt and Kirlin (2001), the tuning appears at a lower thickness for the even component than for the odd and mixed component.

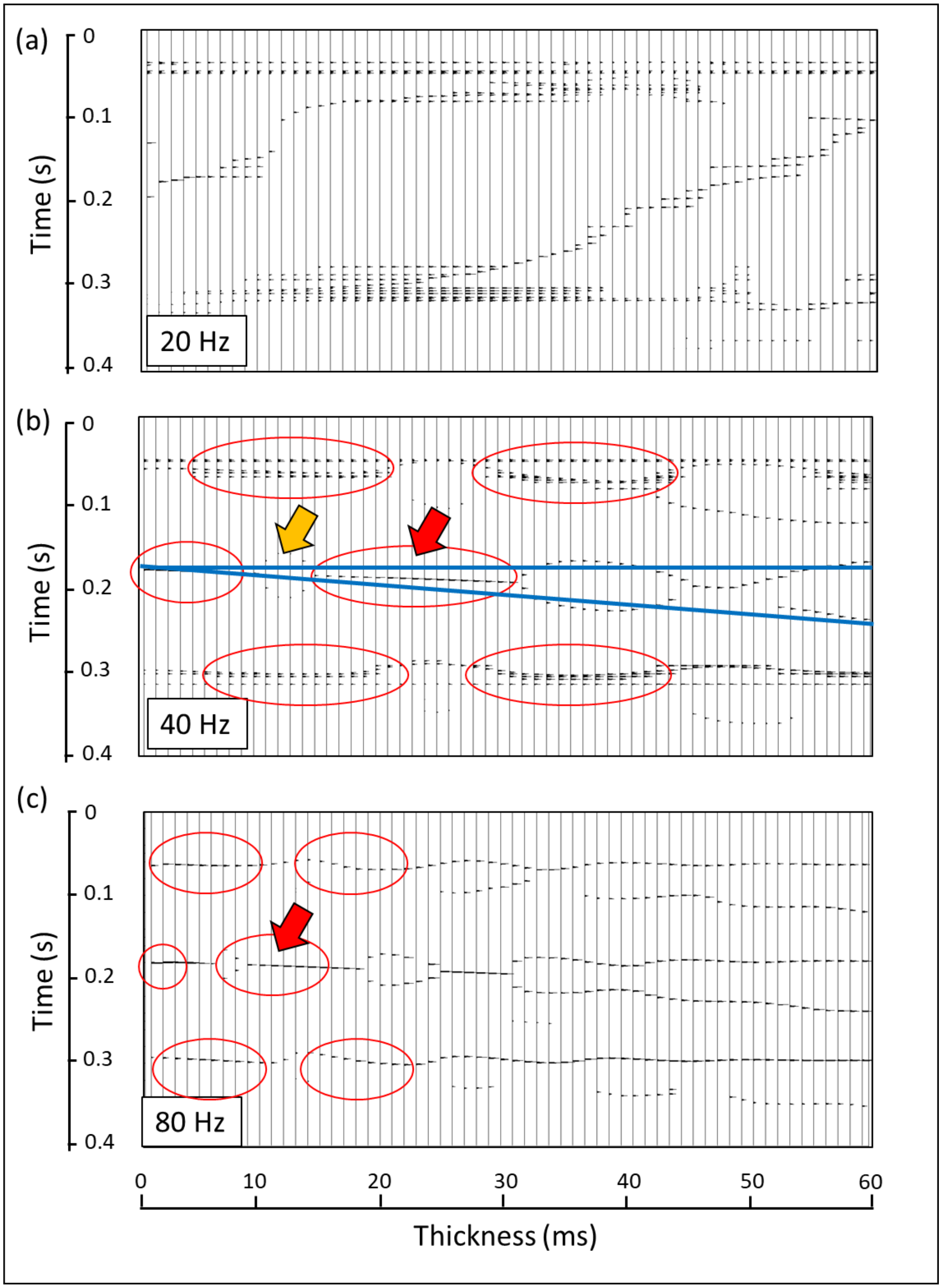

Figure 47. Spectral ridge components for wedge models in **Figure 43** for (a) the 20 Hz component, (b) the 40 Hz component, and (c) the 80 Hz component. Red ellipses indicate tuning zones where resolution of events becomes challenging. Red arrows indicate a mislocation of events due to interference patters. Maximum constructive interference simulates the presence of only one wavelet, which is all that ridges can detect. Orange arrow indicate a location where maximum destructive interference occurs. The main lobe is destroyed but the sidelobe remains, so the algorithm detects it as main peak instead. Blue lines represent actual shape of the wedge.

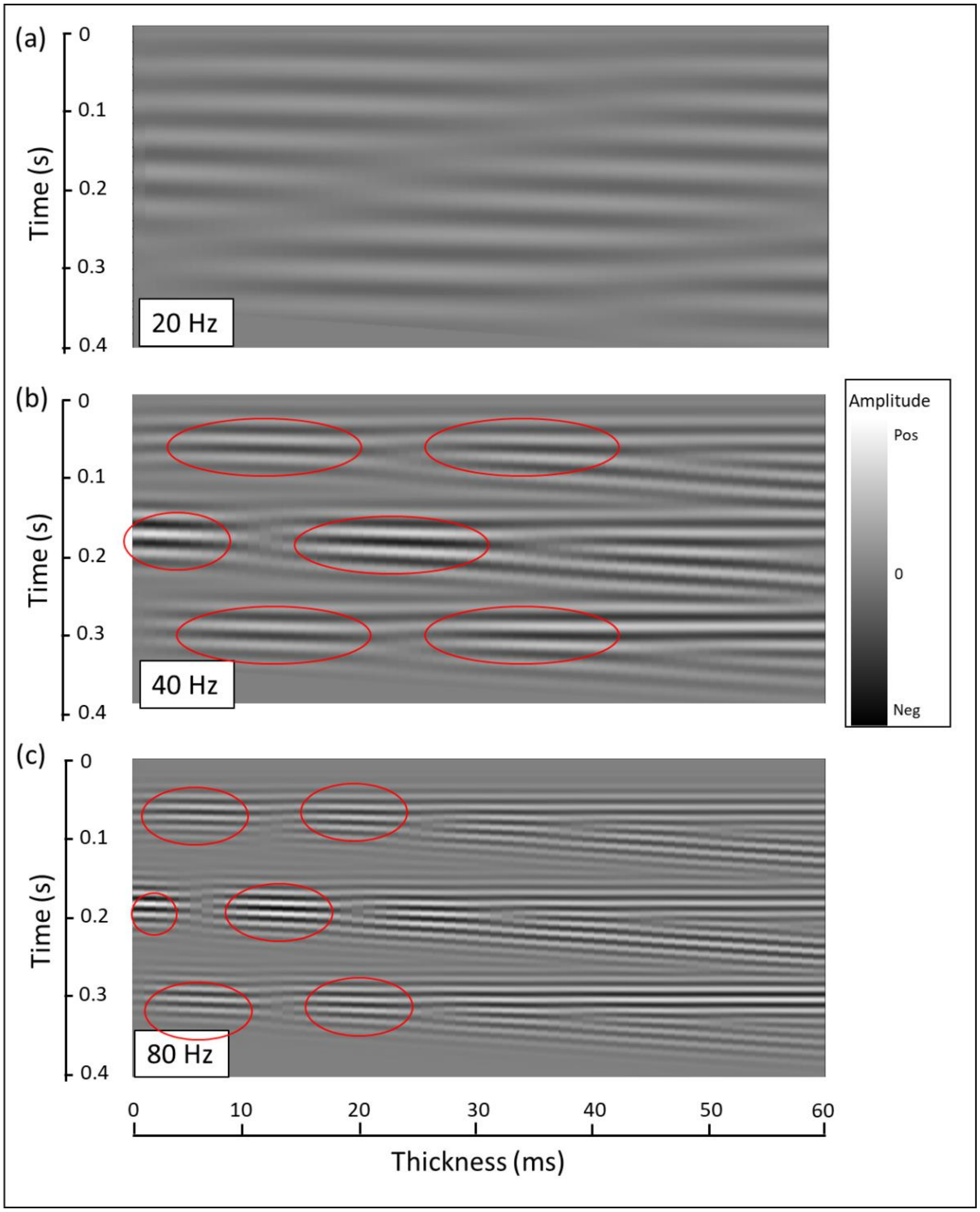

Figure 48. Spectral voice components for wedge models in **Figure 43** for (a) the 20 Hz component, (b) the 40 Hz component, and (c) the 80 Hz component. Red ellipses indicate some of the tuning zones where resolution of events becomes challenging. The high amplitude sidelobes in the 20 Hz component give rise to the extra MML in **Figure 47**a.

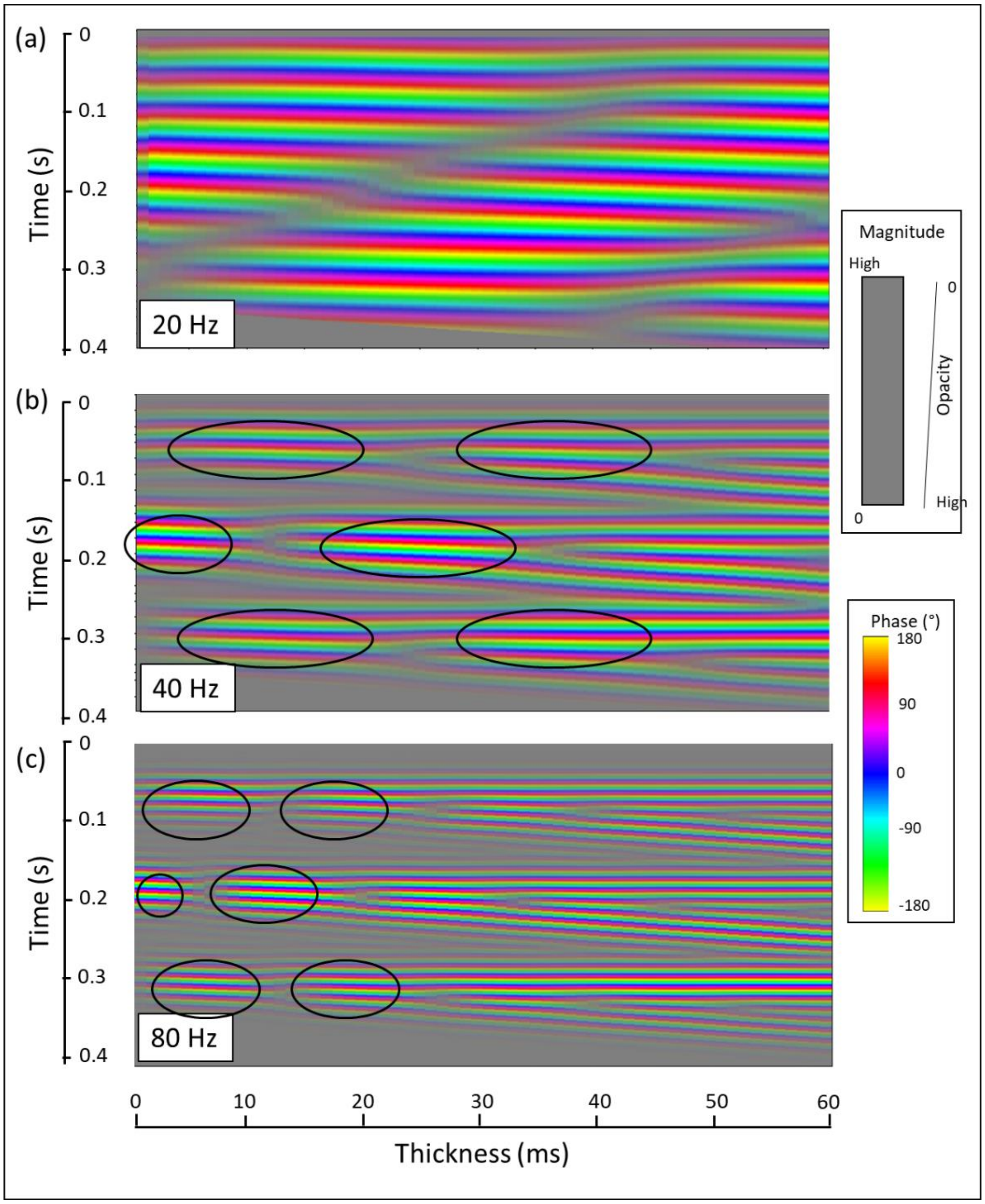

Figure 49. Spectral phase components for wedge models in **Figure 43** for (a) the 20 Hz component, (b) the 40 Hz component, and (c) the 80 Hz component; co-rendered with spectral magnitude component in a monochrome gray color bar. An opacity curve applied for low values of spectral magnitude, rendering high values transparent. Black ellipses indicate some of the tuning zones where resolution of events becomes challenging.

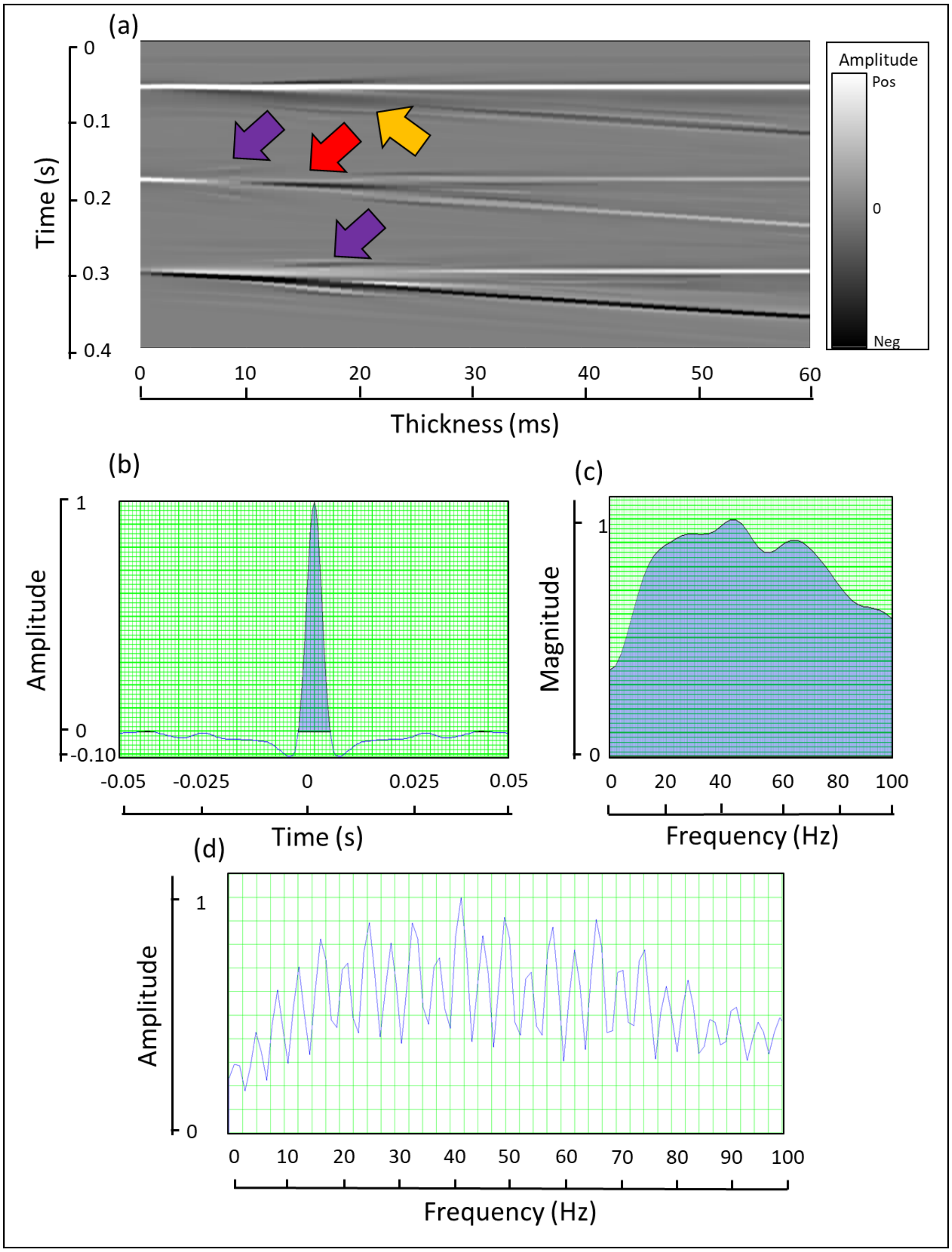

Figure 50.(a) Simple wedge models after bandwidth extension with the (b) extracted wavelet for the entire line and its (c) corresponding magnitude spectrum. (d) shows the amplitude spectrum of all three wedge models. The frequency range selected for the bandwidth extension was 5-100 Hz. As highlighted in **Figure 47**, red arrow indicates location where ridges merged due to tuning interference to create a false event. Purple arrows indicate location of side lobes erroneously interpreted by algorithm as location of ridges. Orange arrow indicates location where algorithm was not capable of resolving bottom layer, resulting in shadow zone within reconstructed line. For high frequency components, the algorithm depicts a sharper and clearer image of the reflectors

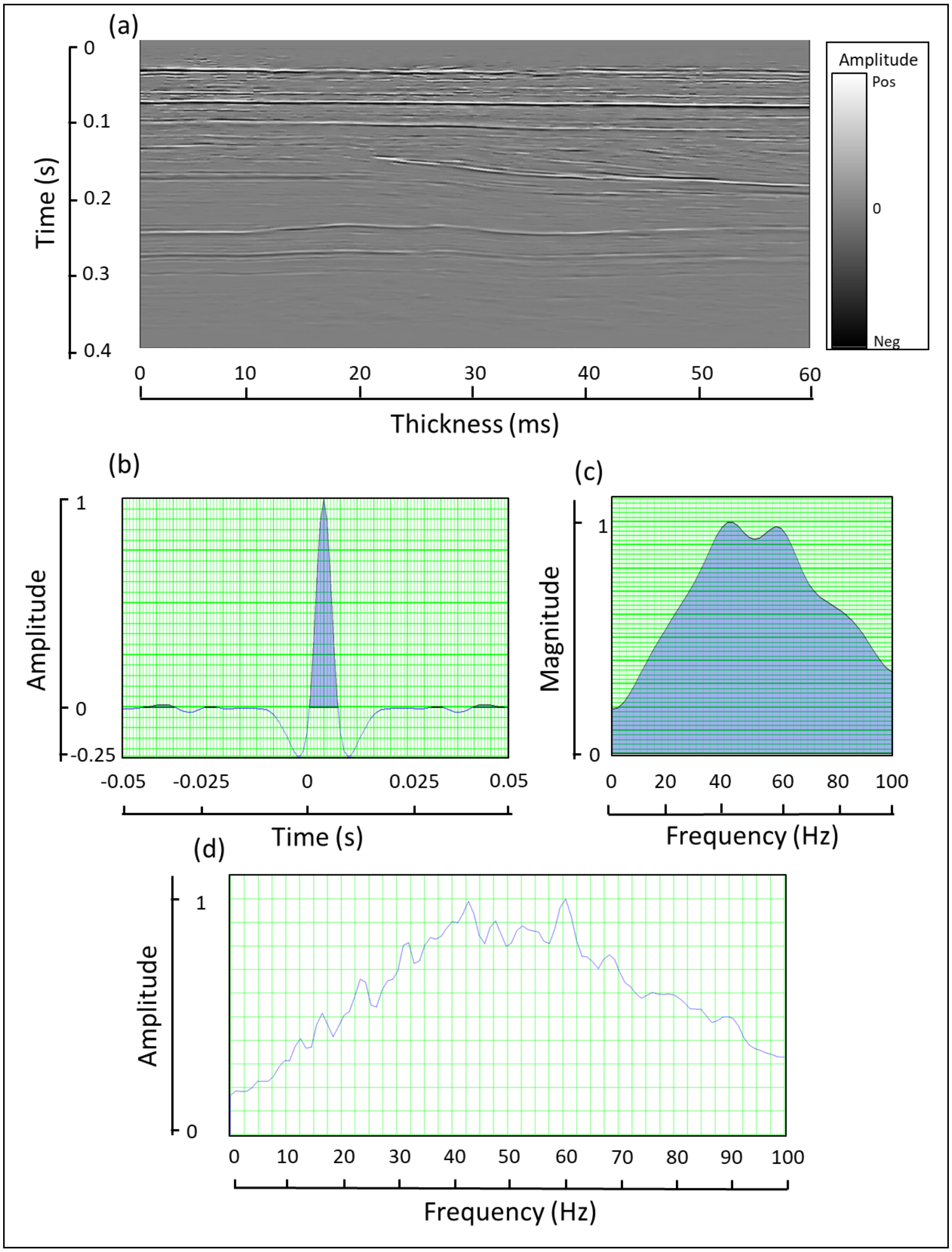

Figure 51. (a) Vertical cross section through bandwidth extended seismic amplitude of the Diamond M field with (b) extracted wavelet in the 500-900 ms interval, approximately corresponding to the Clearfork and Wolfcampian formations, and (c) its corresponding frequency spectrum. (d) displays the amplitude spectrum of the entire volume for the aforementioned interval. The frequency range selected for the bandwidth extension was 5-100 Hz. Note flatter frequency spectrum. However, in the presence of clinoforms in the Clearfork formation, the algorithm fails to highlight them.

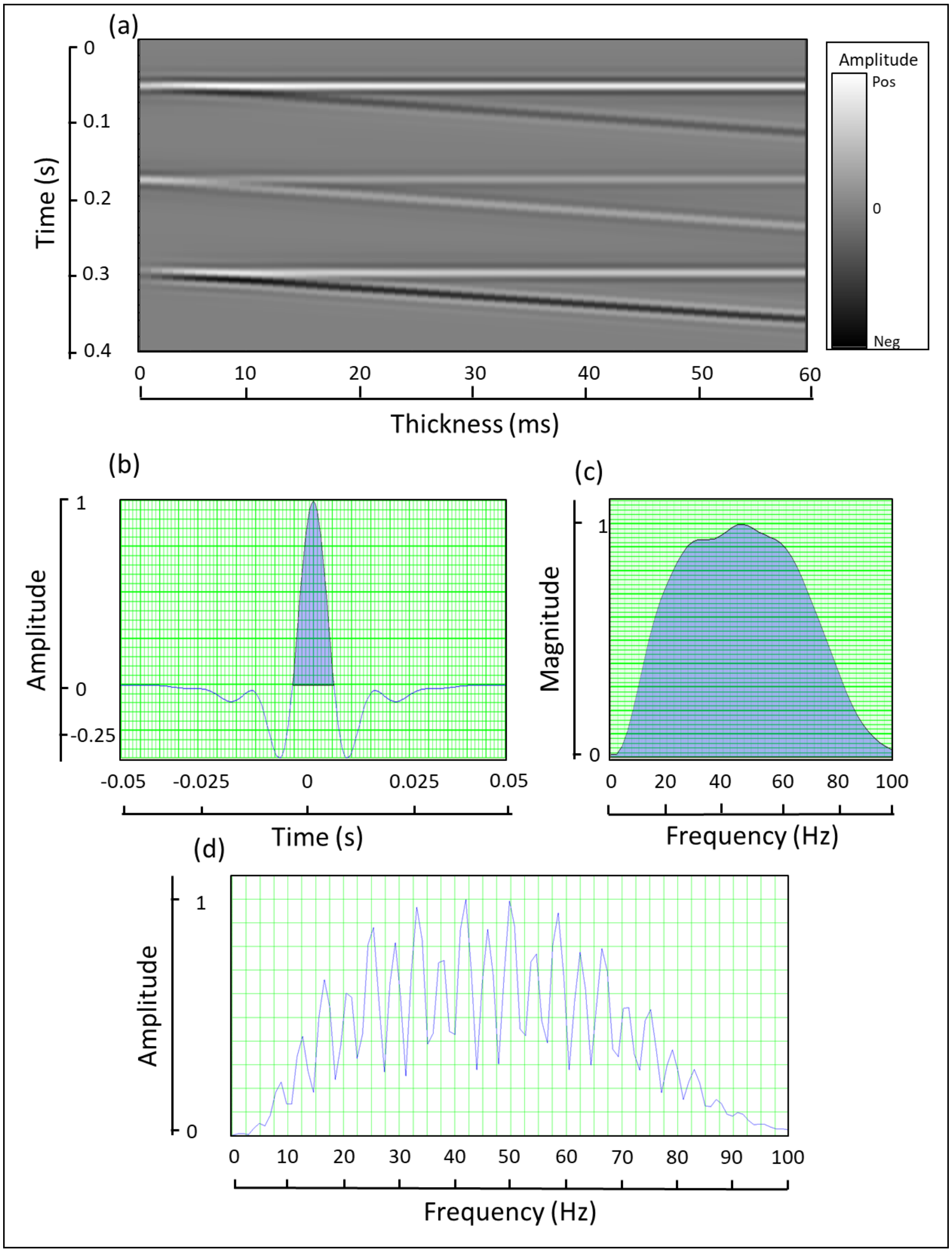

Figure 52. (a) Simple wedge models after spectral balancing with the (b) extracted wavelet for the entire line and its (c) corresponding magnitude spectrum. (d) shows the amplitude spectrum of all three wedge models. Higher and lower frequencies amplitude are balanced when compared with **Figure 43**. I used an epsilon value of ε = 1%.

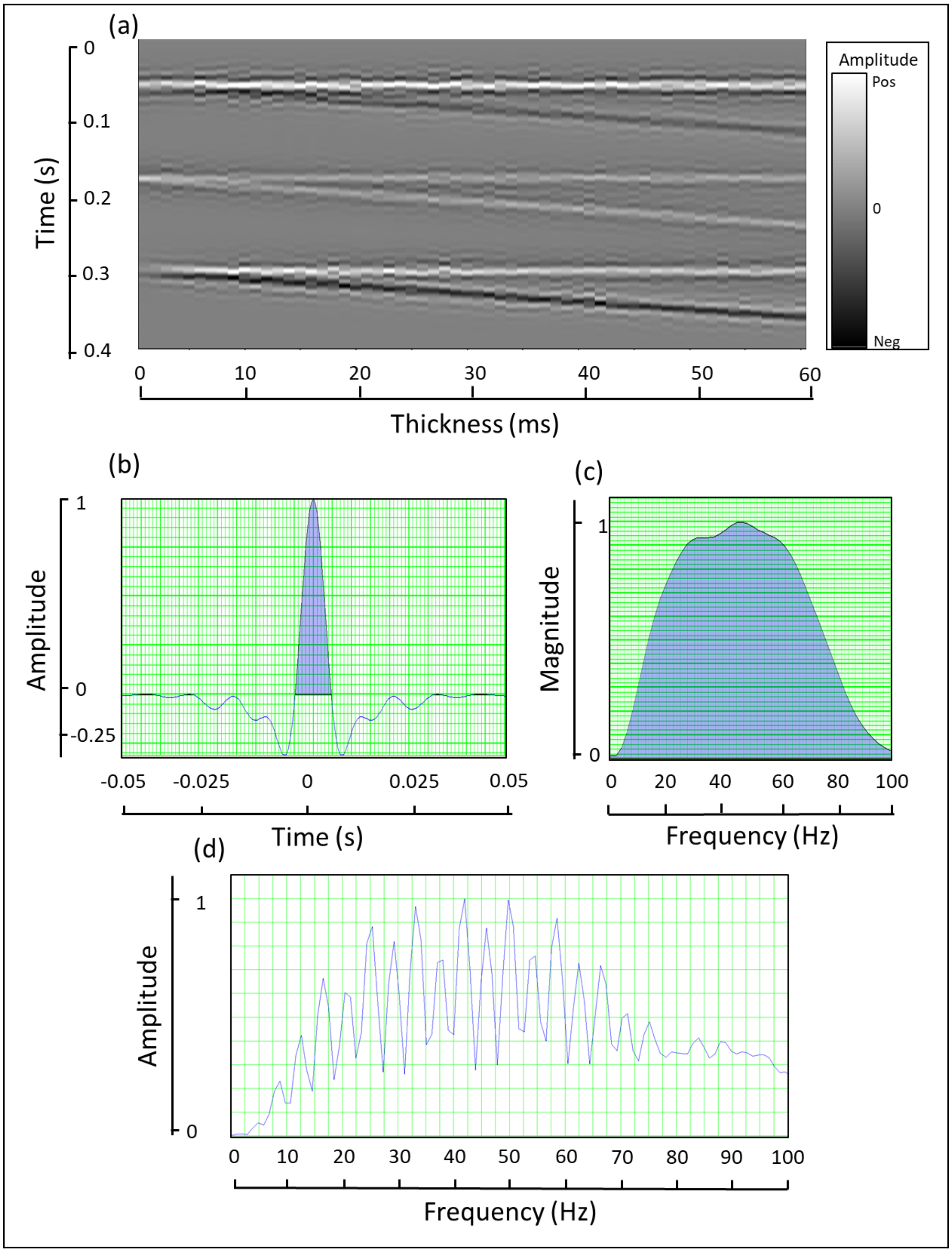

Figure 53. (a) Simple wedge models with added 20% random noise after spectral balancing with the (b) extracted wavelet for the entire line and its (c) corresponding magnitude spectrum. (d) shows the amplitude spectrum of all three wedge models. Higher and lower frequencies amplitude are balanced when compared with **Figure 44**. I used an epsilon value of ε = 1%.

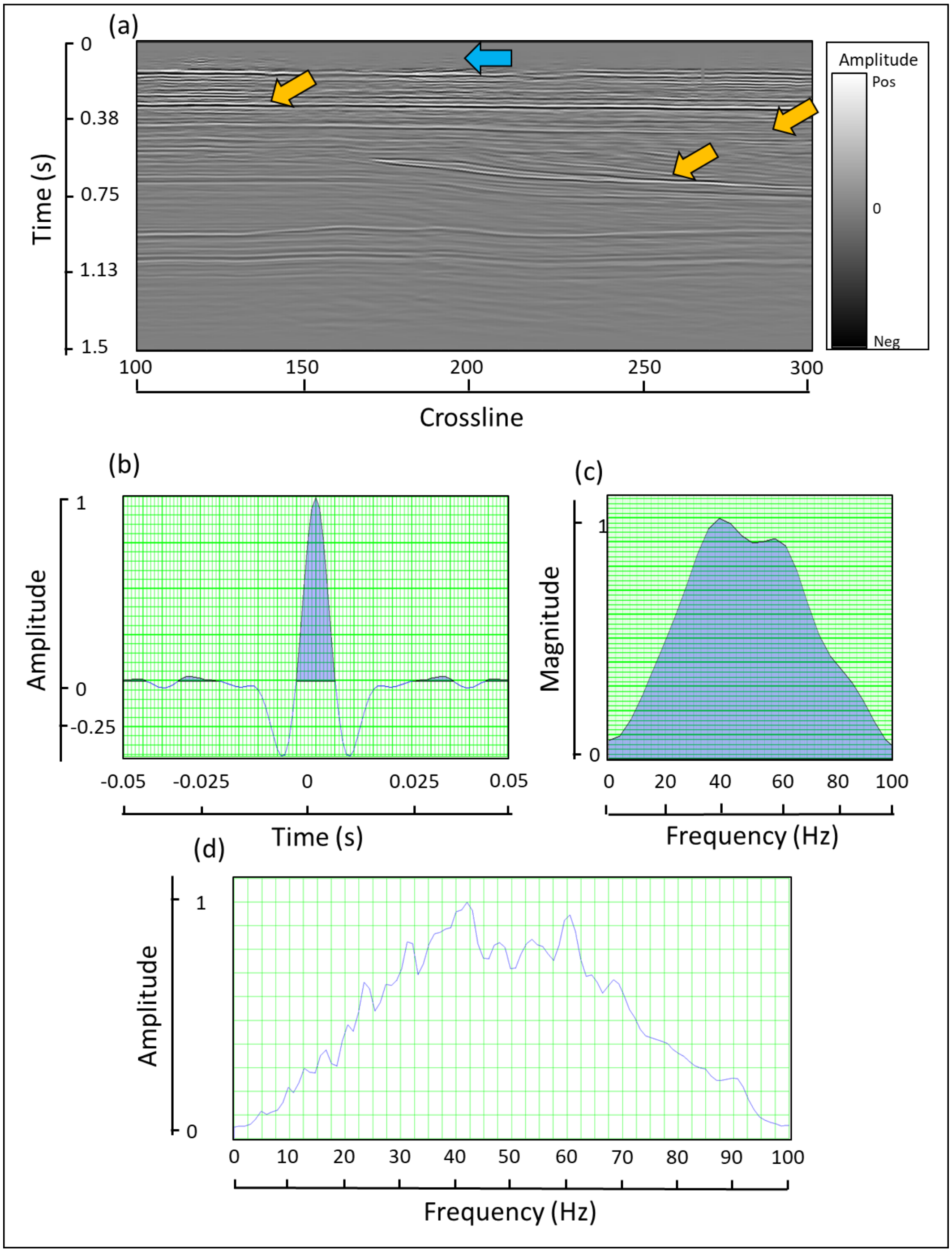

Figure 54. (a) Vertical cross section through spectrally balanced seismic amplitude of the Diamond M field with (b) extracted wavelet in the 500-900 ms interval, approximately corresponding to the Clearfork and Wolfcampian formations, and (c) its corresponding frequency spectrum. (d) displays the amplitude spectrum of the entire volume for the aforementioned interval. Blue arrow indicates attenuated acquisition footprint and orange arrows indicate areas with improved vertical resolution. I used equation 4 with a value of ε = 0.01.

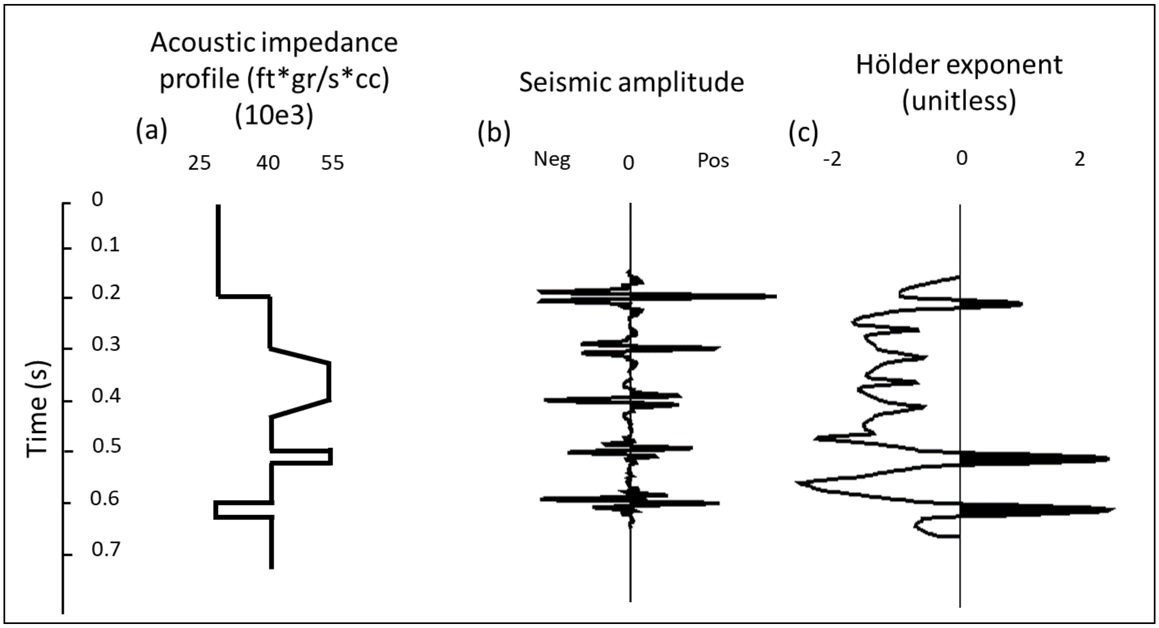

Figure 55. Hölder exponent response to a simple acoustic impedance sequence. (a) shows the modeled acoustic impedance profile generated. A change occurs every 100 ms. Two thin beds of opposite acoustic impedance contrasts are modeled at the bottom, along with a sharp acoustic impedance change in the top and a grading increase and decrease of velocity is modeled between 300 and 500 ms. We convolve this acoustic impedance model with an Ormsby wavelet (*f1=5 Hz, f2=10 Hz, f3= 60 Hz* and *f4=70 Hz*) on (b) to generate a seismic reflectivity trace. We compute the Hölder exponent on this trace and display the result in (c). As expected, the sharp response of the thin beds is matched by high, positive values of the Hölder exponent. The four inflection points in the increasing and decreasing velocity gradients are characterized by four peaks of negative values in the Hölder exponent trace.

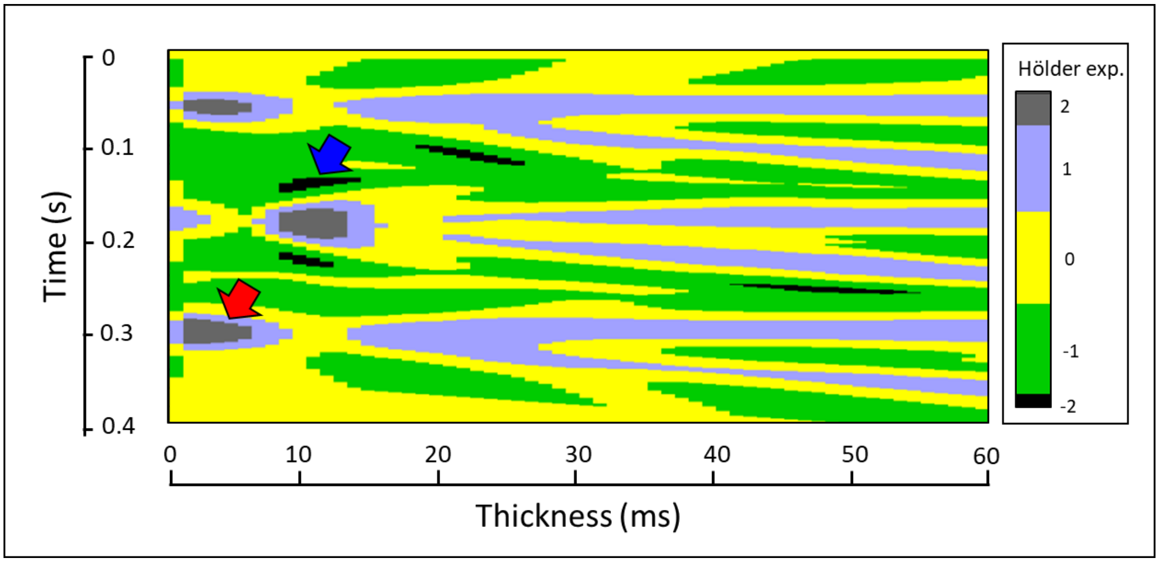

Figure 56. Computed Hölder exponent on wedge models from **Figure 43**. Highest values show location of tuning thicknesses, as in **Figure 46**. Interior of wedges characterized by mid-range values. Blue arrow indicates location of low Hölder exponent anomaly associated with wavelet sidelobes interference patterns. In contrast, red arrow shows location of high Hölder exponent anomaly associated with rapid increase of magnitude of high frequencies due to tuning effects near thin bed conditions.

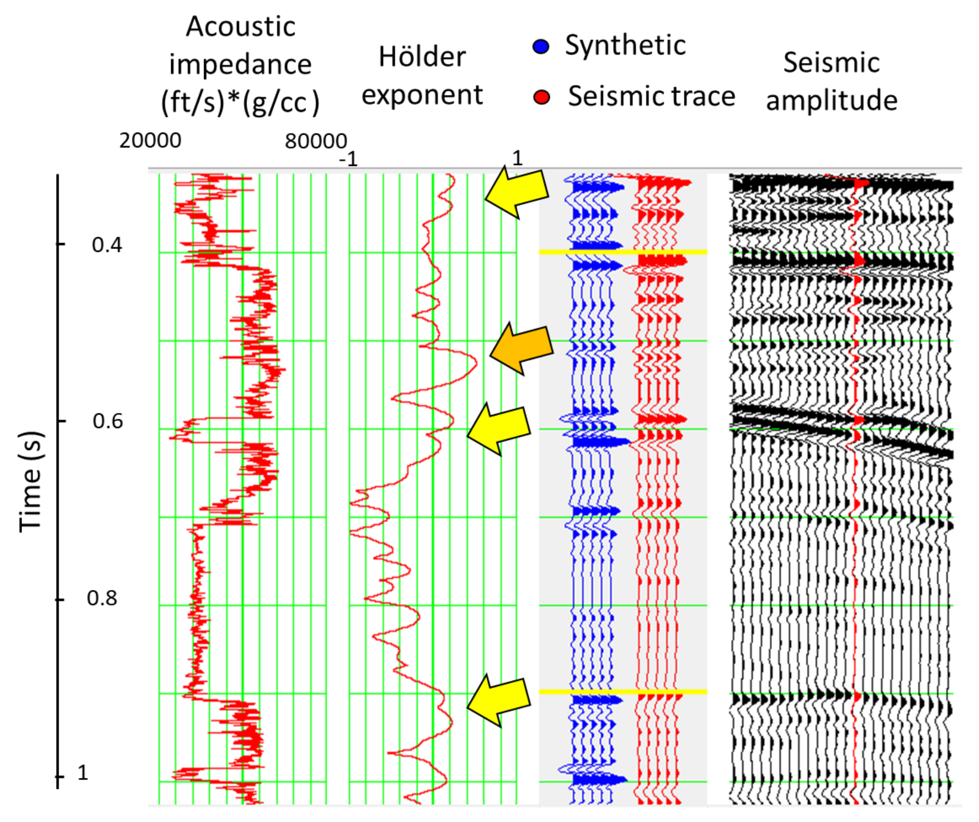

Figure 57. Extracted Hölder exponent trace at well location in Diamond M field. Yellow arrows indicate locations of “M” shaped functions that correspond to changes in the acoustic impedance. Local high values of the attribute, as indicated by orange arrow, may indicate potential zones of interest, as they reveal an increasing magnitude with frequency components that may be associated to potential targets.

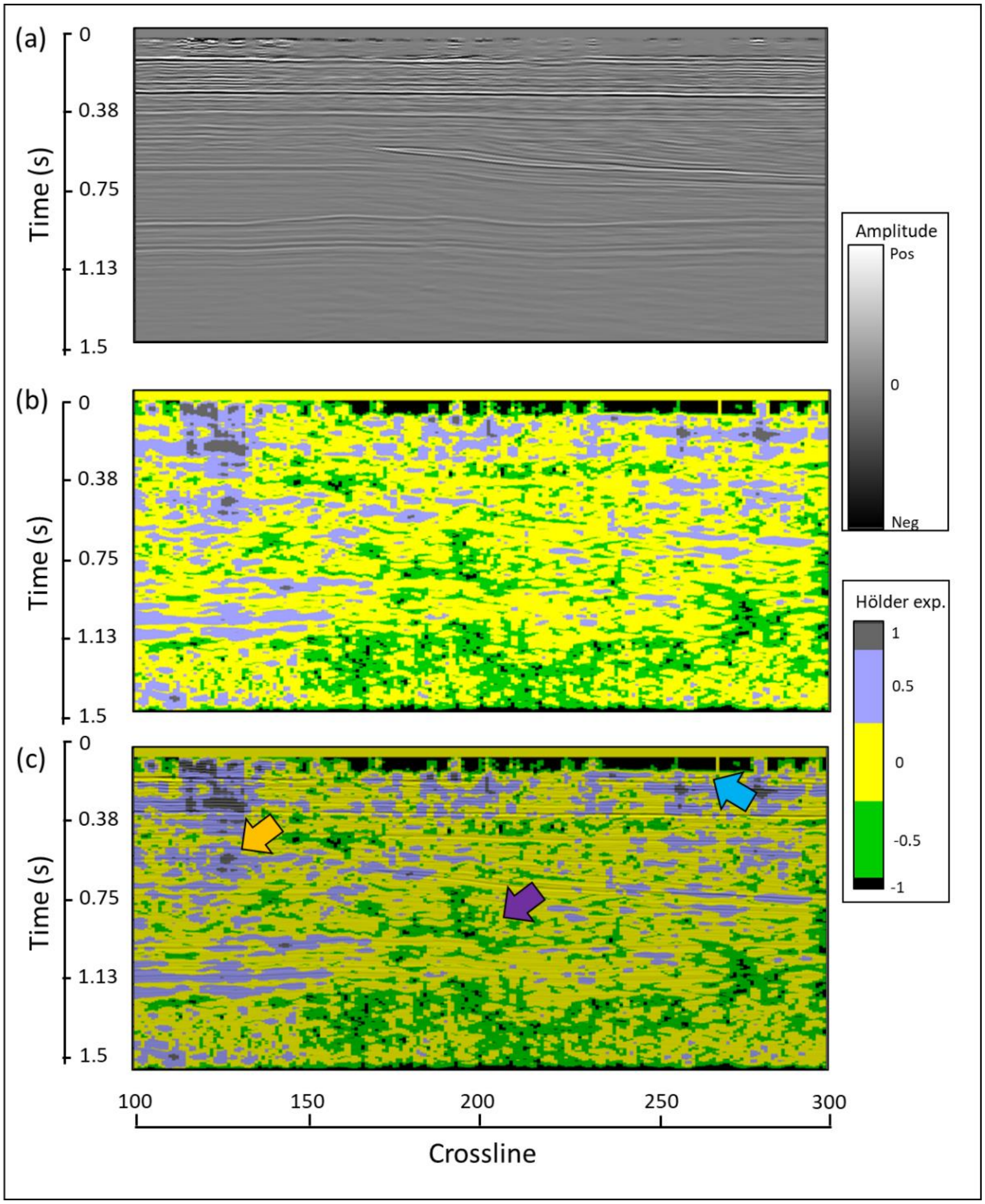

Figure 58. Cross section of seismic volume from the Diamond M field through (a) seismic amplitude, (b) Hölder exponent attribute and (c) correndering of (a) and (b). I selected a discrete color bar better distinguish between different types of singularities that the attribute may be sensitive to. Blue arrow indicates Hölder exponent negative value for acquisition footprint. Orange arrow indicates at high Hölder exponent patch previously unnoticed from amplitude attribute. Purple arrow indicates zone of low, negative Hölder exponent values, interpreted as a result of the low energy Wolfcampian formation at this depth.

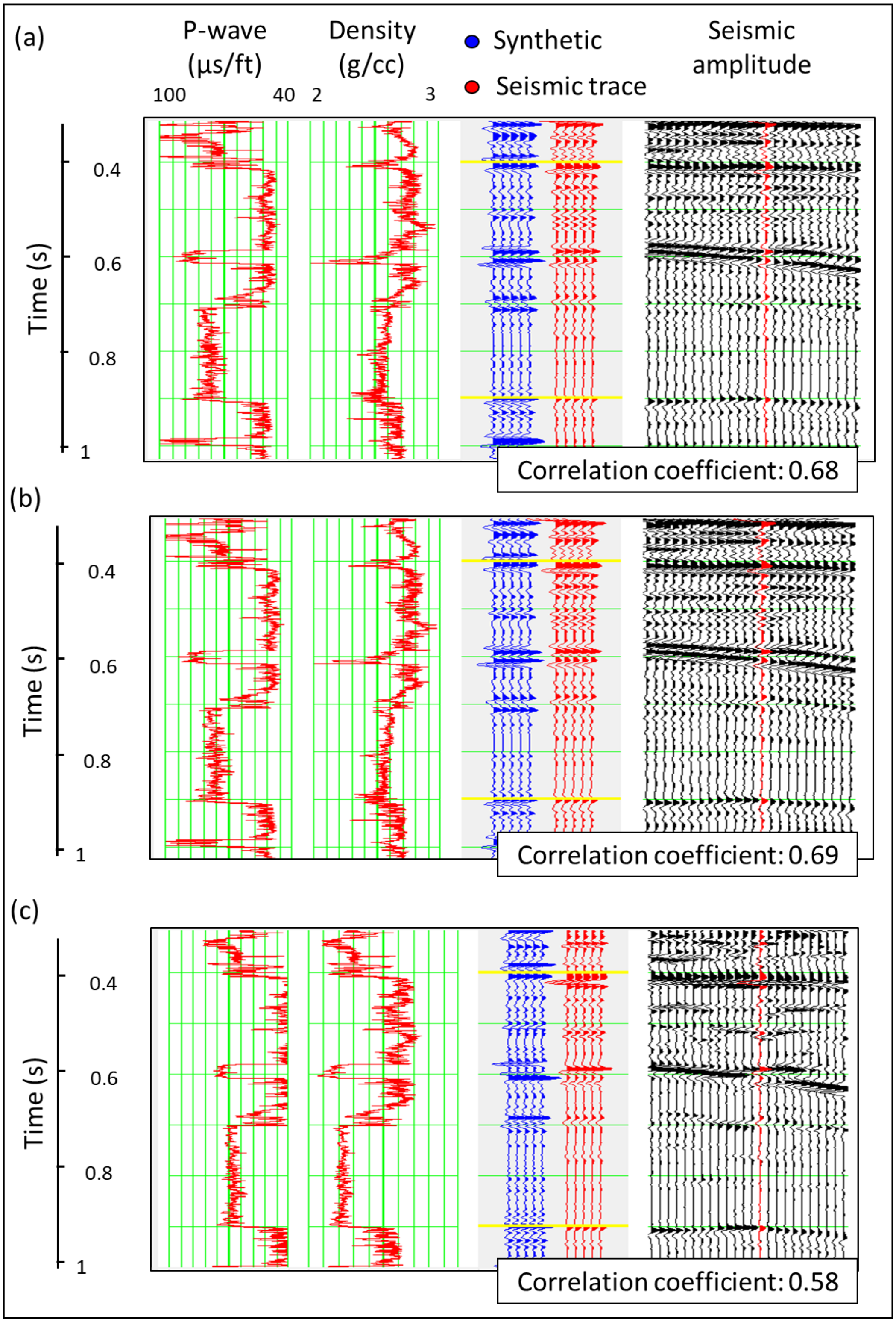

Figure 59. Seismic-to-well tie of Diamond M field seismic volume (a) before, (b) after spectral balancing with epsilon value ε = 1%, and (c) after CWT bandwidth extension with a 5-100 Hz frequency range. Correlation coefficient slightly improved from the subtly higher frequency magnitude balancing performed through this algorithm, but decreased after bandwidth extension. Interference patterns create false events and mislocate others,

resulting in a decreased correlation coefficient. A 5-100 Hz frequency range was used to compute the spectral balancing and CWT bandwidth

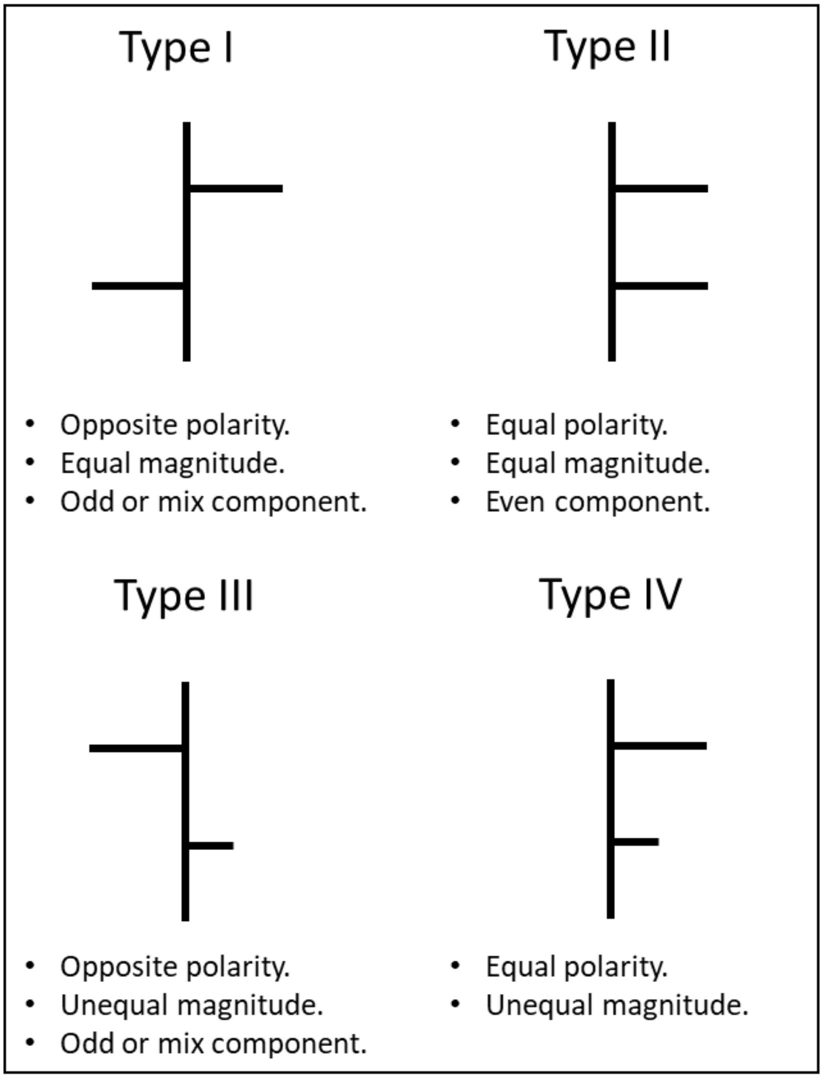
Type I
Type II
• Opposite polarity.
• Equal magnitude.
• Odd or mix component.
• Equal polarity.
• Equal magnitude.
• Even component.
Type III
Type IV
• Opposite polarity.
• Unequal magnitude.
• Odd or mix component.
• Equal polarity.
• Unequal magnitude.

Figure 60. Reflectivity types as defined by Chung and Lawton (1995). This concept was further developed for reflectivity decomposition in odd and even components, as defined by Tirado (2004); Portniaguine and Castagna (2004 and 2005); Chopra et al. (2006); Puryear and Castagna (2008); and Chopra et al. (2009).

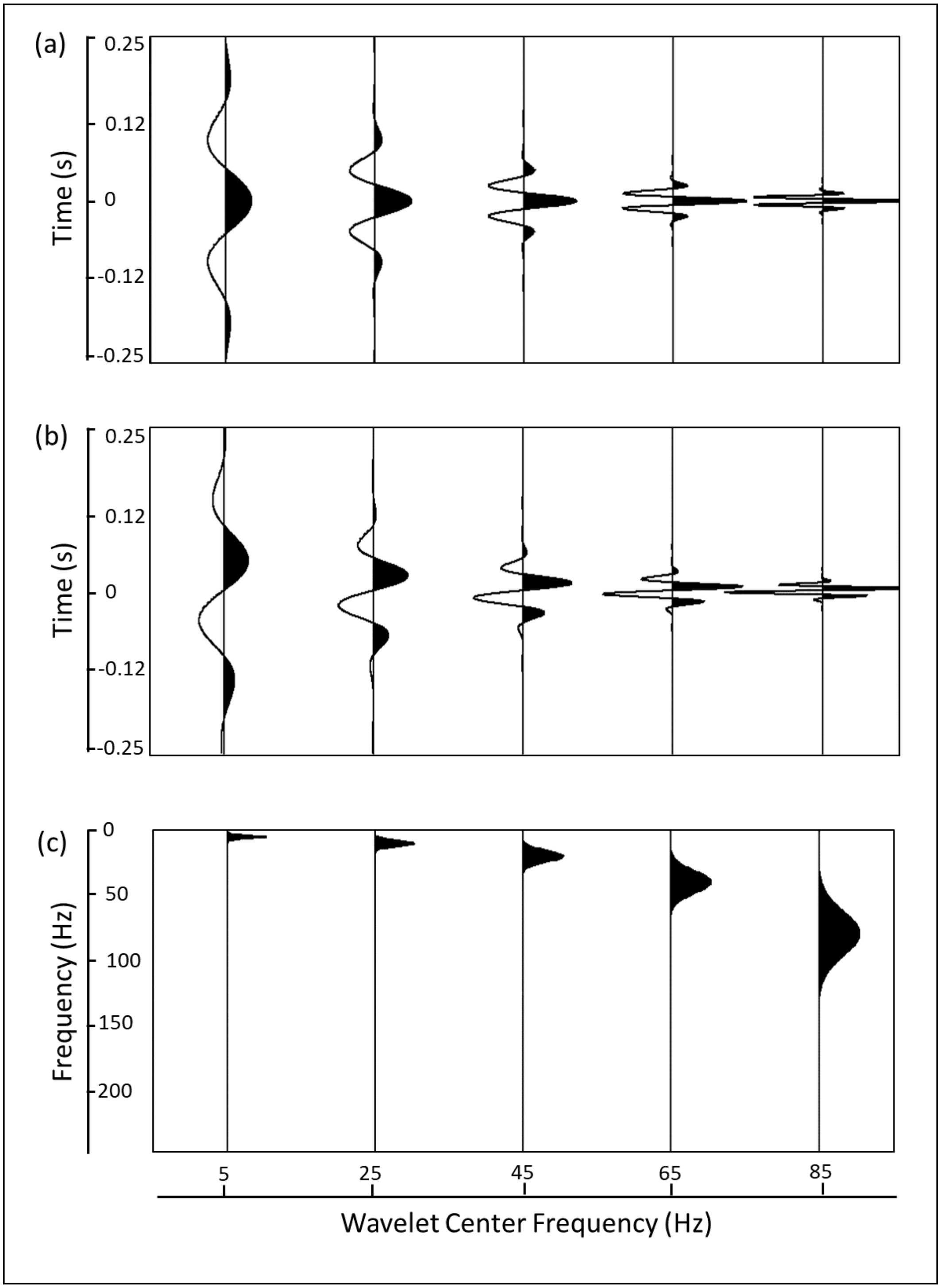

Figure 61. Representative (a) Real and (b) imaginary component of a complex wavelet family and (c) their corresponding amplitude spectrum used in spectral decomposition of wedge models displayed on **Figure 46Figure 47**,**Figure 48** and**Figure 49**. This is also the same wavelet family used to reconstruct spectral balanced outputs in **Figure 52**, **Figure 53** and **Figure 54**. Note how the wavelets become sharper in time and broader band as the center frequency increases. A total of 95 components were computed in the actual decomposition in the range of 5-100 Hz.

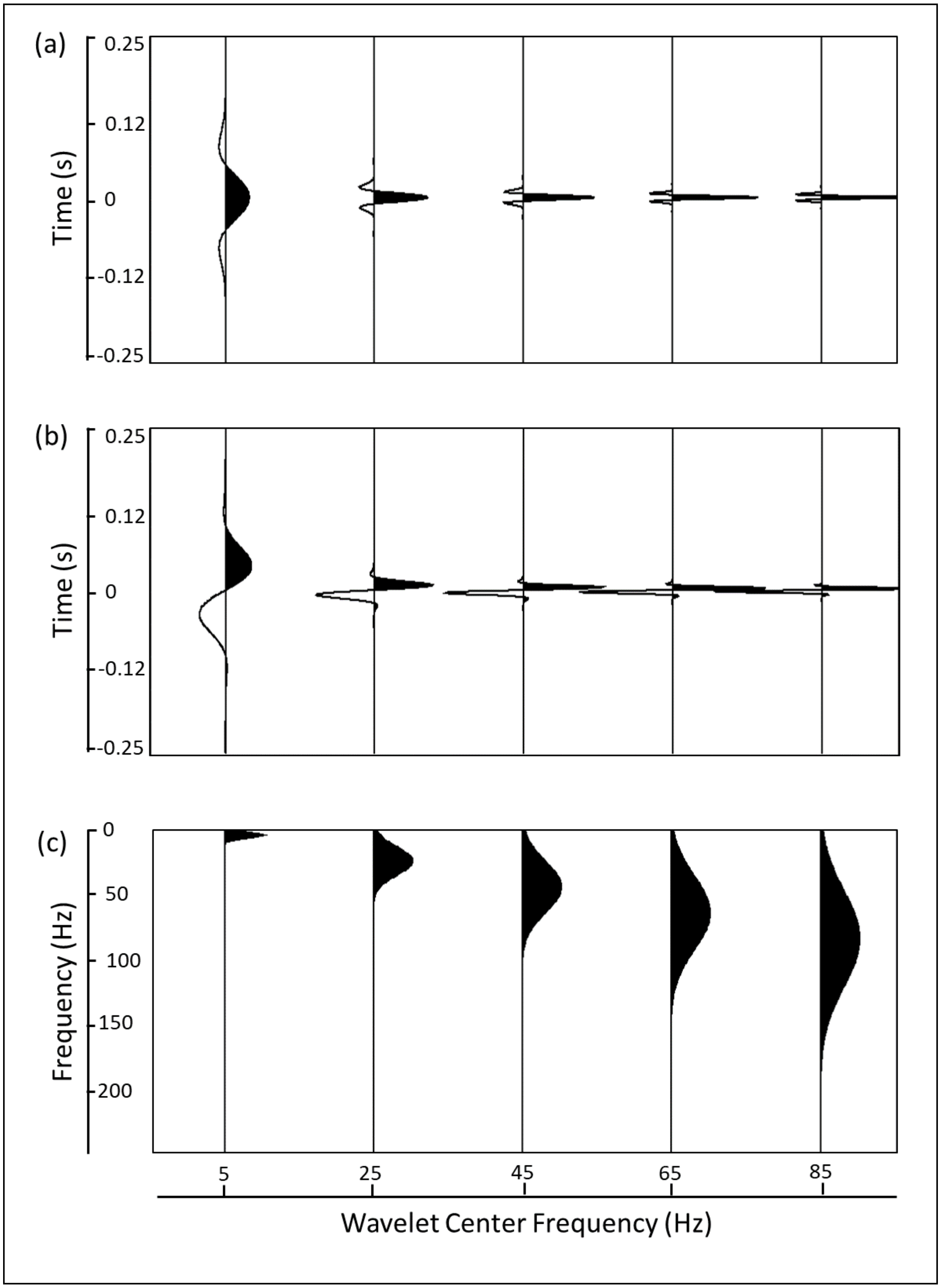

Figure 62. Representative (a) Real and (b) imaginary component of a complex wavelet family and (c) their corresponding amplitude spectrum used in spectral reconstruction of the wedge models in **Figure 51**. The bandwidth of each spectral component is twice as long as each component from **Figure 61**. A total of 95 components were computed in the actual reconstruction in the range of 5-100 Hz.

Chapter 5: Conclusions

In this dissertation I have used well-established reservoir characterization workflows to construct an integrated characterization study of the Arbuckle Group-basement waste water disposal system. The average porosity for the for the Arbuckle Group is approximately 7%, with an average permeability of about 10 mD, and lateral permeability anisotropy of 1.25. The vertical to lateral permeability anisotropy of the Arbuckle Group is approximately 0.01.

The dominant parameters affecting history-matching are the porosity and the horizontal and vertical permeability of the Arbuckle Group. Faults play an important role in fluid movement within Arbuckle and Basement group formations. I observed pockets of non-uniform and large pressure buildup in this and overlying formations.

For improving current interpretation workflows for analyzing igneous intrusions within different host rocks, I have forward modeled and observed seismic attribute response of intrusions in synthetic seismograms. I have found that synthetic models' seismic attributes response can help to identify sill emplacement mechanisms in real seismic data from Payne county, Oklahoma. By carefully constructing an appropriate velocity model and depth-migrating my seismic volume, I have shown that such workflow can help reveal structures that would otherwise go unnoticed.

Seismic resolution below tuning remains an important geophysical problem for which a final solution is yet to be found. Widess' model for thin bed resolution provides a good baseline for understanding the limits of conventionally acquired seismic volumes in both land and marine data. However, since it does not account for a majority of the cases encountered in most exploration and production campaigns, a more generalized model is necessary.

Of the three methods evaluated, none is capable of resolving events below seismic resolution in a reliable way. Spectral balancing provides an incremental improvement while bandwidth extension provides cosmetic changes in well resolved areas and erroneous results in poorly resolved areas. The Hölder exponent can highlight thin beds for potential exploration or development targets, but does not extent the resolution in any way. The topic of seismic resolution remains relevant, yet not completely understood and unraveled for geophysical purposes.